




Review

On the Catalytic Mechanism of 3d and 4d Transition-Metal-Based Materials on the Hydrogen Sorption Properties of Mg/MgH₂

Jinzhe Lyu ^{1,2,*} , Viktor Kudiiarov ^{1,*} , Leonid Svyatkin ¹ , Andrey Lider ¹ and Kejie Dai ²

¹ Division for Experimental Physics, School of Nuclear Science & Engineering, National Research Tomsk Polytechnic University, Lenin Ave. 43, 634034 Tomsk, Russia

² School of Electrical and Mechanical Engineering, Pingdingshan University, Pingdingshan 467000, China

* Correspondence: lyujinzh@pdsu.edu.cn (J.L.); kudiyarov@tpu.ru (V.K.)

Abstract: The slow hydrogenation/dehydrogenation kinetics and high thermodynamic stability of the Mg–H bond are the two major limitations for the large-scale utilization of MgH₂. In this review, we introduce the catalytic mechanism of 3d and 4d transition metal (TM) on the hydrogen sorption properties of Mg/MgH₂. The relative contribution of interatomic interactions to the thermodynamic stability of the TM-substituted MgH₂ system is discussed. A synergy effect between the electronegativity and the radius of the TM element is proposed to explain the charge transfer process between TM and H in the TM-substituted MgH₂ system. The catalytic mechanism of TM nearby the surface of Mg is more complicated than that in the volume of Mg, as the surface-doped TM can experience more options for doping sites, leading to the hindrance effect and causing various contributions of the *d* band center to the dissociation of hydrogen molecules and the diffusion of hydrogen atoms nearby the surface of Mg. In terms of the catalytic mechanism of TM for hydrogen sorption kinetics of Mg/MgH₂, we particularly focused on the “hydrogen pump” effect existing in the Mg–TM–H system. Other mechanisms, such as a possible catalytic mechanism of TM for the hydrogen sorption properties of nano-sized freestanding Mg/MgH₂, were also presented.

Keywords: χ rule; radius effect; charge transfer; *d* band center; “hydrogen pump”



Citation: Lyu, J.; Kudiiarov, V.; Svyatkin, L.; Lider, A.; Dai, K. On the Catalytic Mechanism of 3d and 4d Transition-Metal-Based Materials on the Hydrogen Sorption Properties of Mg/MgH₂. *Catalysts* **2023**, *13*, 519. <https://doi.org/10.3390/catal13030519>

Academic Editor: Carl Redshaw

Received: 14 January 2023

Revised: 17 February 2023

Accepted: 17 February 2023

Published: 3 March 2023



Copyright: © 2023 by the authors. Licensee MDPI, Basel, Switzerland. This article is an open access article distributed under the terms and conditions of the Creative Commons Attribution (CC BY) license (<https://creativecommons.org/licenses/by/4.0/>).

1. Introduction

Along with the rapid growth of the world’s population and economic globalization, global energy demand is increasing day by day, leading to a shortage of traditional fossil energy resources. At the same time, greenhouse gases emitted by the use of traditional fossil fuels lead to environmental degradation issues such as the greenhouse effect and acid rain. In this context, mankind urgently needs to develop renewable, clean, and efficient green new energy sources to replace traditional ones to alleviate and solve the dual crisis of the exhaustion of fossil fuels and the deterioration of the human living environment [1–3]. As a kind of clean energy, hydrogen has received notable attention; however, for the broader and more conventional usage of hydrogen energy, a few limitations in its production, storage, and distribution need to be overcome [4,5]. In particular, lowering costs and developing good de/hydrogenation kinetics, high hydrogen storage density, and a hydrogen storage approach with a moderate operating temperature are the bottlenecks for the practical application of hydrogen energy [6,7]. The storage of hydrogen currently relies mainly on gaseous storage and liquefaction storage. For gaseous storage, bulky and high-pressure-resistant steel cylinders are required (the pressure in the cylinder usually reaches about 15 MPa), and the actual weight of hydrogen stored in the cylinder is only 1–2% of the cylinder’s weight, which greatly reduces the gravimetric hydrogen storage capacity [4]. Although newly developed lightweight carbon-fiber composite materials can withstand pressures of 35–70 MPa, reaching a gravimetric hydrogen storage density of 3.0–6.0 wt%,

high-compression energy consumption, the high cost of hydrogen storage tanks, and safety issues such as hydrogen leakage and blasting still limit the large-scale application of gaseous hydrogen storage [8]. The density of liquid hydrogen is 70.8 kg m^{-3} , showing excellent volumetric hydrogen storage capacity. However, it is difficult for liquid hydrogen to meet practical hydrogen storage applications, because 30% of the chemical energy of hydrogen must be consumed in the hydrogen liquefaction process, and the thermal insulation device is expensive and complicated [8,9]. Solid-state hydrogen storage is a method that uses specific materials to physically/chemically interact with hydrogen and fix the hydrogen in the material [10]. Solid-state hydrogen storage has attracted much attention due to it having the highest volumetric density (higher than that of liquid hydrogen) and relative safety when properly used, despite its limitation on thermodynamic and kinetic properties that are associated with de/hydrogenation reaction [3,11,12]. Furthermore, compared with the use of H_2 in high-pressure cylinders or liquid form, solid-state hydride systems with the same weight and size characteristics and the same mileage without refueling (usually, 300–400 km) can store more H_2 [13].

The hydrogen storage properties of some representative hydrogen storage alloys are summarized in Figure 1. Complex hydrides such as LiBH_4 and NaAlH_4 , consisting of metal cations and hydrogen-containing complex anions with hydrogen atoms presented in a complex form and covalently bonded to central atoms such as boron or aluminum, have high gravimetric and volumetric hydrogen capacity and are most promising to fulfill capacity requirements among all hydrogen storage materials. However, most complex hydride compounds do not possess favorable hydrogen desorption thermodynamics and/or kinetics and high temperatures are required to desorb hydrogen, often with impurities. Furthermore, in addition to poor reversibility, the desorption of hydrogen from complex hydride occurs through multi-step reactions, which lead to a formation of multi-phase intermediates that is unfavorable for onboard applications [5,12,14]. Sorbent materials such as metal–organic frameworks (MOFs) and carbon nanotubes (CNTs) possess nano/micro pores and high surface area, which allows the physical adsorption of hydrogen molecules on the surface via van der Waals force without dissociation [15,16]. However, the weak van der Waals force, with adsorption enthalpy of $4\text{--}10 \text{ kJ mol}^{-1} \text{ H}_2$ and binding energy in the range of 0.04 to 0.1 eV, restrains the hydrogen adsorption in these materials at room temperature, and thus, a low temperature is needed to reach a high hydrogen storage capacity [16–18]. Chemical hydrides such as NH_3BH_3 , containing covalently bound hydrogen atoms in solid or liquid form, have a high density of hydrogen [12]. Particularly, chemical hydrogen storage may be a good option if systems involve liquids that may be easily dispensed using infrastructure that is similar to today's gasoline refueling stations. However, the spent chemical hydrides cannot be reconstituted simply at a modest temperature and hydrogen pressure; thus, they would have to be regenerated off-board the vehicle [19]. Investigations into liquid organic hydrogen carriers such as cyclohexane, methylcyclohexane, and decaline have also been conducted, but the high hydrogen release temperature and the required noble-metal catalysts are significant drawbacks [20,21].

MgH_2 is one of the most promising materials for hydrogen storage applications due to its high gravimetric and volumetric capacities (7.65 wt% and $110 \text{ kg H}_2 \text{ m}^{-3}$, respectively) [22]. Furthermore, Mg exists in abundance and is the eighth-most common element in the Earth's crust, accounting for ~2.35% of its composition [23]. Rutile MgH_2 (Figure 2a), the lattice parameters of which are $a = b = 4.501 \text{ \AA}$ and $c = 3.010 \text{ \AA}$, has a tetragonal symmetry ($P4_2/mnm$, Group No.136) with occupation of Mg and H atoms on the Wyckoff positions (0, 0, 0) and (0.304, 0.304, 0), respectively [22]. As shown in Figure 2a, in the crystal structure of MgH_2 , each H atom has three first-coordination Mg atoms and each Mg atom has six first-coordination H atoms, i.e., each Mg atom is located in an octahedron made up of six H atoms. In MgH_2 , Mg is not as fully ionized as Mg^{2+} ; thus, the remaining charge of Mg contributes to the covalent bonding of the MgH_2 system [6,24–28]. In the density of states (DOS) of MgH_2 , the conduction band is mainly contributed by the $\text{Mg}(3s)$ and $\text{Mg}(2p)$ orbitals (Figure 2c), indicating a strong Mg–H ionic bonding interaction.

Additionally, some Mg–H covalent bonding interactions arise from a few Mg(3s) and Mg(2p) orbitals hybridizing with H(1s) orbitals in the valence band: (1) the bonding peak between E_F and -3.0 eV is mainly contributed by the valence electrons of H(1s), Mg(2p) and a few Mg(3s) orbitals [29]; (2) the bonding peak between -4.0 and -3.0 eV results from the interaction between H(1s) and Mg(3s) as well as a few Mg(2p) electrons [29]; (3) the bonding peak between -7.0 and -4.0 eV is the bonding of valence electrons of H(1s) and Mg(3s) [29].

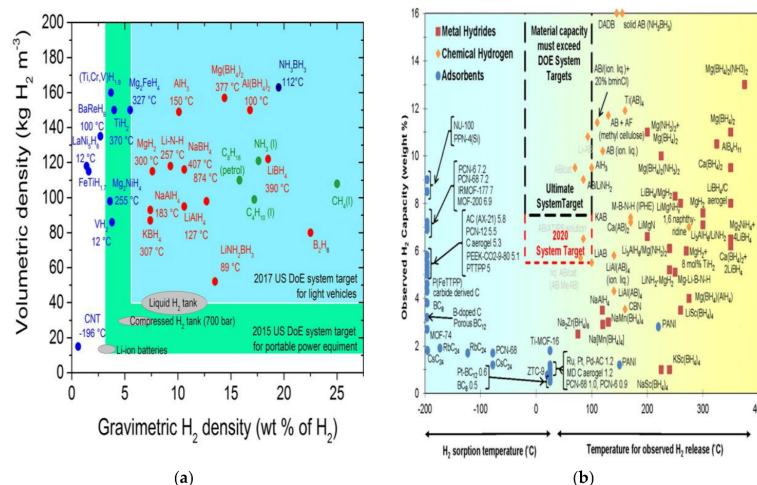


Figure 1. (a) Potential high-capacity hydrides. Reproduced with permission [16]. Copyright 2015, John Wiley and Sons. (b) Gravimetric hydrogen capacity and sorption temperature of various hydrogen storage materials. Reproduced with permission [5]. Copyright 2017, Elsevier.

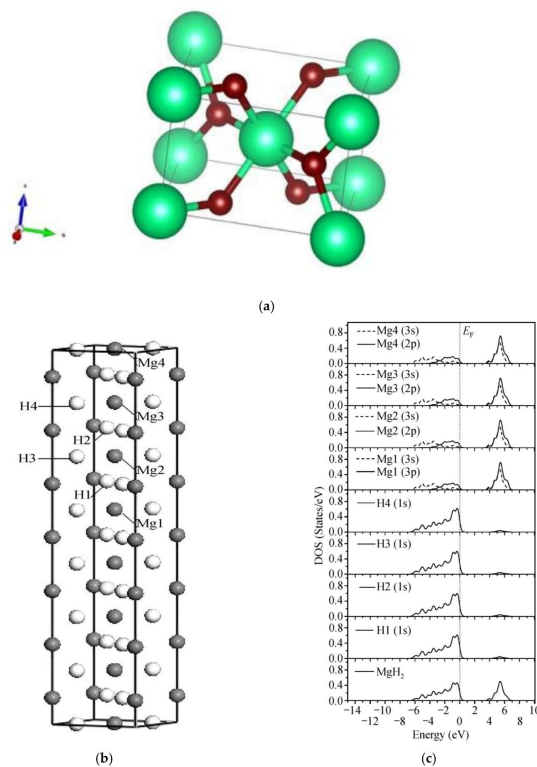


Figure 2. (a) Rutile crystal structure (β -phase) of MgH_2 . (b) MgH_2 supercell. (c) Total and partial DOS of (b) MgH_2 supercell model. (b,c) Reproduced with permission [29]. Copyright 2006, Springer Nature.

Despite the high hydrogen storage capacity, there are several major impediments in the practical utilization of MgH_2 for hydrogen storage, as described below.

1. In terms of de/hydrogenation thermodynamics, a mixture of ionic and covalent bonding in the MgH_2 matrix is responsible for the high stability of MgH_2 [30], thereby leading to a very low room-temperature plateau pressure [31] and a high dehydrogenation enthalpy of up to $75 \text{ kJ mol}^{-1} \text{ H}_2$, which is much larger than the practical requirements for metal hydrides of $20\text{--}40 \text{ kJ mol}^{-1} \text{ H}_2$ [32–35]. Thus, a high temperature is needed for the hydrogen desorption of MgH_2 . As can be seen from Figure 3, thermodynamically, the dehydrogenation of MgH_2 occurs only at temperatures higher than 500 K. Experimentally, under standard hydrogen pressure (1 bar), temperatures higher than 573 K will be required to realize the dehydrogenation reaction of MgH_2 [36]. For feeding fuel cells, magnesium hydride should be heated above 560 K to release hydrogen above 0.1 MPa [37]. This is significantly higher than the temperature range required by practical applications, as shown in Figure 1b. Furthermore, the absence of *d* electrons in Mg, which can facilitate the dissociation of hydrogen molecules into H atoms, results in the high dissociation energy of $432 \text{ kJ mol}^{-1} \text{ H}_2$ [38,39].

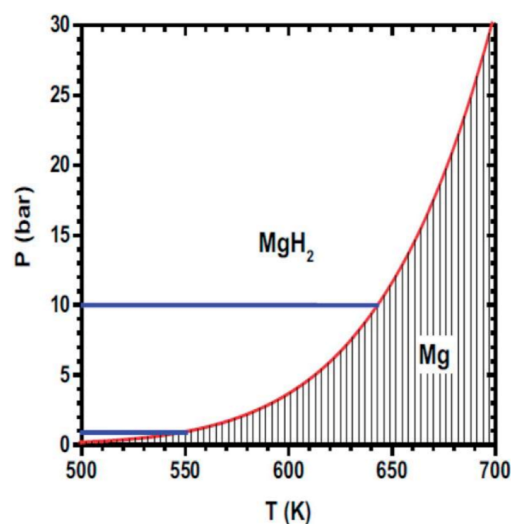


Figure 3. The variation of plateau pressure as a function of temperature for magnesium hydride. Reproduced with permission [33]. Copyright 2016, Springer Nature.

2. For the kinetics issue, from calculation results of the hydrogenation process, the activation energy barriers for the H_2 dissociation on clean $\text{Mg}(0001)$ is 1.42 eV ($137 \text{ kJ mol}^{-1} \text{ H}_2$) [40], and the adsorption energies for H_2 molecules over the clean $\text{Mg}(0001)$ is -0.114 eV ($-11 \text{ kJ mol}^{-1} \text{ H}_2$) [41]. The surface penetration is often the rate-limiting step for H atom diffusion, as the energy barrier can reach 0.69 eV ($67 \text{ kJ mol}^{-1} \text{ H}$) for clean $\text{Mg}(0001)$ [40]. The activation energy for the diffusion of a hydrogen atom in the rutile MgH_2 is also very high—up to 2.21 eV ($213 \text{ kJ mol}^{-1} \text{ H}$) [42]. The high energy barrier is also observed for dehydrogenation of MgH_2 . For example, the experimental energy barriers of pure MgH_2 materials are observed to be around $161\text{--}188 \text{ kJ mol}^{-1}$ [36,43–46]; hence, hydrogen sorption kinetics in the Mg/MgH_2 system are sluggish below 573 K [37,47,48], and as a result, a much lower desorption plateau than the absorption plateau in the pressure–composition–temperature (PCT) curves of MgH_2 is observed, exhibiting a high hysteresis [34].
3. Thermodynamically, the reaction of metallic Mg with hydrogen should proceed at notably low pressure ($<1 \text{ bar}$) and low temperatures (below 323 K) [33,49,50], as can be seen in Figure 3. In practice, however, the reaction between metallic Mg and hydrogen is not observed at low temperatures even at 100 bar hydrogen pressure [49]. Due to slow kinetics, the conversion from magnesium to magnesium hydride is very difficult below 623 K, even when the magnesium is prepared into very fine powder [3]. Thus,

conventionally, the hydrogenation of Mg without any additives requires temperatures and pressures as high as 623 K and 70 bar H₂ [51]. This phenomenon arises from the fact that an oxide passivation layer can be easily formed on Mg, even when Mg is stored in a globe box [37,52], which induces a extremely high activation energy barrier (2.34–2.94 eV or 226–284 kJ mol^{−1}) to the dissociative adsorption of hydrogen [53] and may hinder the penetration of H atom, thereby decreasing the hydrogen storage capacity in Mg [12,54–57] due to the weak nature of the interactions between H₂ and magnesium oxide clusters (the hydrogen physisorption induced by the electrostatic field, which is produced by the polarity of the Mg–O bond due to the charge transfer from the magnesium atoms to the oxygen ones) [18]. Hence, Mg requires initial activation to absorb hydrogen in order to induce the passivation film cracks so that bare Mg surfaces are accessible to hydrogen [58]. However, even after activation, the sorption kinetics can still be rather sluggish [3]; for example, the complete hydrogenation of pure magnesium at 673 K takes several hours [4].

4. The low thermal conductivity of MgH₂ (0.4 W mK^{−1} [59,60]) is a serious problem, since heat transfer can significantly influence the de/hydrogenation processes.
5. It has already been proved that a gas of free electrons is very important for the adsorption and desorption of hydrogen, hence their high rates in metals [61–63]. Thus, the fact that MgH₂ is a semiconductor with the relatively large energy gap of 4.16 eV [64–67] explains the high stability of MgH₂ as well as its sluggish hydrogen sorption kinetics [68], as a low concentration of free-charge carriers in semiconductors leads to a higher barrier compared to metals [63].
6. As is known, in metals, increased hydrogen concentration leads to more sites being occupied by hydrogen atoms, which makes some migration paths unavailable and therefore results in a decreased hydrogen diffusion coefficient [42]. For Mg, the diffusion coefficient or diffusivity (*D*) of hydrogen in MgH₂ can be as low as 10^{−18} m² s^{−1} at 573 K [31,69,70], which is at least three orders of magnitude less than that in Mg [38,71,72]. Thus, as the hydrogenation reaction progresses, a hydride layer, which grows on the metal surface, limits the ability of hydrogen atoms to diffuse into the volume [73]. On the one hand, the low diffusion coefficients of H₂ in the MgH₂/Mg system is another explanation for the sluggish kinetics [38]; on the other hand, it can serve as one of the factors leading to the incomplete hydrogenation of bulk Mg, as the growth of hydride colonies/grains leads to a decrease in the total effective cross-section area for hydrogen diffusion into the magnesium phase. After the impingement of the hydride colonies/grains, the growth of hydride is limited by hydrogen diffusion through the hydride, and maximum capacity is reached [74]. The issue of incomplete hydrogenation of bulk Mg is also believed to be related to the strain energy inhibiting the growth of MgH₂ as MgH₂–Mg interfaces grow into the last small MgH₂-surrounded Mg islands [71]. Thus, for mechanical milled Mg, before the actual hydrogenation data acquisition, each sample must go through several hydrogenation/dehydrogenation cycles to eliminate residual stress caused during mechanical milling [75].
7. The lower the dehydrogenation enthalpy (ΔH), the higher the overall efficiency of filling hydrogen energy (Figure 4). Taking into account the filling of hydrogen energy and the overall efficiency of the application equipment, in practical applications, the dehydrogenation enthalpy of the most suitable hydrogen storage material should be 20–30 kJ mol^{−1} H₂ [64,76], which is coincident with the practical requirements for metal hydrides in terms of the thermodynamics as mentioned above.

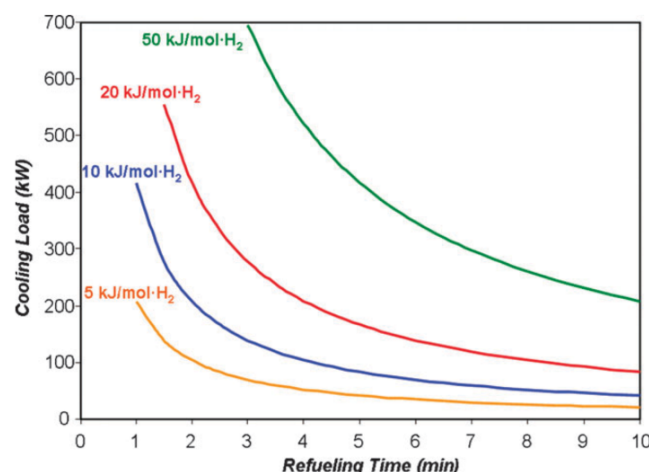


Figure 4. Theoretically required cooling load (kW) as a function of refueling time (min) for absorbing 5 kg of H₂ into storage materials of various ΔH . Reproduced with permission [76]. Copyright 2010, Royal Society of Chemistry.

To overcome this challenge, numerous modification methods such as catalyst doping [50,77–86], alloying [87–97], and nano-structuring [47,98–100] have been applied to alleviate the unfavorable thermodynamic and kinetic barriers of MgH₂. Among all of the reported modified MgH₂ systems, the system doped with transition metal (TM)-based additives shows better hydrogen storage properties [101]. It has been widely established that TMs and their compounds/oxides are quite effective in reducing the hydrogen storage temperatures for MgH₂ [32,102–111] and have been proved to be another effective strategy for improving the hydrogen sorption kinetic performances of MgH₂ [109,111–120], although such improved kinetics may sacrifice some portion of storage capacity due to considerable dead mass in a total composite [12]. The oxidation resistance of MgH₂ can also be improved by reasonable TM-based additives (e.g., CeO₂) and effective processing to circumvent the need for MgH₂ to be used only in a rigorous oxygen-free environment, which consumes substantial resources to maintain and is impractical in large-scale and long-life applications [121]. Doping of TMs with *f* electrons can improve the hydrogen sorption properties of MgH₂ in a three-fold way: (1) the large size of lanthanide dopants enhance the unit cell volume and hence increase the Mg–H bond length, reducing the Mg–H correlation and decreasing the desorption temperature [122]; (2) the presence of localized *f* orbitals of lanthanide across Fermi energy makes the lanthanide-doped MgH₂ cell show more metallic behavior [122]; (3) the substitutional atoms of TMs with *f* electrons in MgH₂ allows for the destabilization of the Mg–H bond as a result of the interaction between the valence electron of H and the unsaturated *f* electron shells of TMs [123]. However, as shown in Table 1, the volumetric and gravimetric capacity would decrease with the doping of TMs with *f* electrons in MgH₂ due to an increase in both volume and mass [122,124]. Thus, in this review, we interpreted mechanisms related only to TMs with *d* electrons, which have smaller atomic radii and relative atomic masses compared to TMs with *f* electrons.

Table 1. Lattice parameters, unit cell volume, specific capacity, and formation energy of pure MgH₂ and doped MgH₂, calculated from the density functional theory (DFT) study. Reprinted/adapted with permission from Refs. [122,124]. Copyright 2016, Elsevier.

Material	<i>a</i> [Å]	<i>c</i> [Å]	<i>V</i> ₀ [Å ³]	<i>r</i> (TM) [pm] ^(a)	<i>m</i> (TM) ^(b)	Volumetric Capacity [g H ₂ L ^{−1}]	Gravimetric Capacity [wt%]	Formation Energy [kJ mol ^{−1} H ₂]
MgH ₂	4.5180	3.021	61.67	150, for Mg	24, for Mg	109	7.66	−67.72
Mg ₁₅ LaH ₃₂	4.6180	3.1374	66.91	195	139	101	6.02	−64.06
Mg ₁₅ CeH ₃₂	4.5894	3.1239	65.80	185	140	102	6.00	−60.55
Mg ₁₅ PrH ₃₂	4.5885	3.1173	65.63	185	141	103	6.00	−60.97
Mg ₁₅ NdH ₃₂	4.5865	3.1139	65.50	185	144	103	5.96	−61.97
Mg ₁₅ GdH ₃₂	4.5430	3.0987	63.95	180	157	105	5.82	−72.63
Mg ₁₅ DyH ₃₂	4.6509	2.9493	63.79	175	163	106	5.77	−70.68

^(a) These data represent the empirical radius of Mg and TM dopant elements from reference [125]. ^(b) These data represent the standard atomic weight of Mg and TM dopant elements from reference [126].

2. Formation of Mg–TM Alloy and Mg–TM–H System

Figure 5 shows a general enthalpy diagram illustrating the destabilization of a strongly bound hydride through the addition of a reactive additive. The hydride, AH₂, is effectively destabilized due to the formation of AB_x, which leads to a reduction of the dehydrogenation enthalpy. In the case of destabilization due to the formation of binary intermetallic compounds, two kinds of reactions can be distinguished [127]: (1) processes in which MgH₂ reacts with a metal/semimetal during dehydrogenation, forming a binary compound, and (2) routes in which MgH₂ reacts with an Mg-containing intermetallic compound producing another intermetallic after dehydrogenation. Obviously, the second type of reaction could only take place in Mg–metal systems where magnesium forms at least two binary compounds or alloys with a metal [127]. The reaction shown in Figure 5 occurs when element A is Mg and element B is a TM such as Cu and Cd. No ternary hydrides have been reported in the literature for the Mg–Cu system; however, Mg and Cu can form the Mg₂Cu alloy, which decomposes to MgH₂ and MgCu₂ under 30 MPa hydrogen pressure according to an irreversible disproportionation reaction represented by (1) with a hydride formation enthalpy and entropy of reaction of −73.5 kJ mol^{−1} H₂ and −146 J K^{−1} mol^{−1} H₂, respectively [34,128,129]:



Cadmium is the only element exhibiting unlimited solubility in Mg in the solid state [34,130]. Below 526 K, an ordered MgCd α'' phase is formed from the disordered Mg–Cd solid solution [130,131]. Mg-rich alloys can form another α''' ordered-phase Mg₃Cd [130]. Thus the Mg–Cd system is the only Mg-based system exhibiting order–disorder transformation in the temperature range relevant for the hydrogenation reaction [130], which may lead to an abrupt change of hydrogen diffusivity in the vicinity of transformation temperature according to the previous study on the ordering of Ni₃Mn and diffusivity of hydrogen in the alloy [132], although no effect of the order–disorder transformation in the Mg₃Cd and MgCd phases on the kinetics of hydrogenation was observed in the work of Skripnyuk and Rabkin [130]. Based on the presence of XRD peaks in the MgCd phase and the pure Cd in the hydrogenated alloy, as well as the presence of a Cd-rich phase on the surface of MgH₂ grains in the SEM micrographs, Skripnyuk and Rabkin [130] confirmed that the solubility of Cd in the MgH₂ hydride is negligible, and as a result, during hydrogenation, Cd is rejected from the hydrogenated phase and accumulates in the remaining unreacted Mg–Cd alloy, changing its composition toward higher Cd contents by forming the pockets of MgCd and other Cd-rich phases on/between the MgH₂ grains through the following reaction:



where $\text{Cd}_{\text{Mg}_3\text{Cd}}$ stands for the Cd atom dissolved in the unreacted Mg_3Cd alloy. Some other reported possible reactions in the Mg–TM system are listed in Table 2. A similar reaction occurs when element A is Mg and element B is a rare-earth (RE) metal, because Mg and RE metals can form Mg-rich intermetallics (e.g., REMg_2 , $\text{RE}_2\text{Mg}_{17}$, $\text{RE}_5\text{Mg}_{41}$, etc.), which, independent of their composition and structure, interact with hydrogen gas to yield a homogeneous mixture of MgH_2 and rare-earth hydrides according to the following reaction [31]:

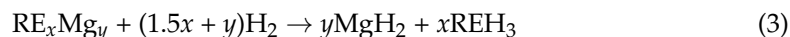


Table 2. Thermodynamic parameters of MgH_2 destabilized by different metals. Reprinted/adapted with permission from Ref. [127]. Copyright 2014, Elsevier.

System	Reaction	Overall Dehydrodrying Enthalpy ΔH [kJ mol ^{−1} H ₂]
Mg–Ag	$\text{MgH}_2 + \text{Ag} \leftrightarrow \text{AgMg} + \text{H}_2$	39.1
	$2\text{MgH}_2 + \text{AgMg} \leftrightarrow \text{AgMg}_3 + 2\text{H}_2$	69.8
	$3\text{MgH}_2 + \text{AgMg} \leftrightarrow \text{AgMg}_4 + 3\text{H}_2$	69.1
Mg–Cu	$\text{MgH}_2 + 2\text{Cu} \leftrightarrow \text{MgCu}_2 + \text{H}_2$	41.0
	$3\text{MgH}_2 + \text{Cd} \leftrightarrow \text{Mg}_3\text{Cd} + 3\text{H}_2$	68.6
	$\text{MgH}_2 + \text{Cd} \leftrightarrow \text{MgCd} + \text{H}_2$	62.3
Mg–Cd	$\text{MgH}_2 + 3\text{Cd} \leftrightarrow \text{MgCd}_3 + \text{H}_2$	57.0
	$2\text{MgH}_2 + \text{MgCd} \leftrightarrow \text{Mg}_3\text{Cd} + 2\text{H}_2$	65.2 or 71
	$3\text{MgH}_2 + 2\text{MgPd} \leftrightarrow \text{Mg}_5\text{Pd}_2 + 3\text{H}_2$	90.17

The products of reaction (3) allow reversible desorption up to 5.5–6 wt% H (depending on the amount of the rare-earth metal), according to the following scheme [31]:

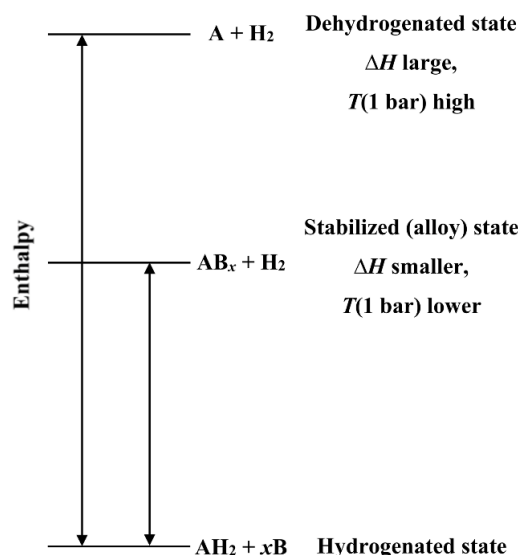
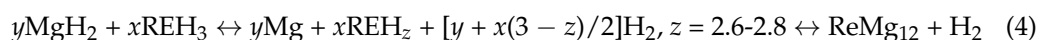


Figure 5. Generalized enthalpy diagram illustrating destabilization through alloy formation upon dehydrogenation. Reproduced with permission [133]. Copyright 2007, Elsevier.

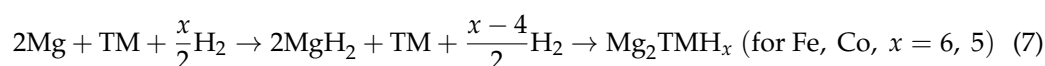
Among Mg–TM–H ternary hydrides, the numerous groups of hydrogen-rich hydrides of Mg with early transition metals (ETM; elements on the left side of the periodic table, from group 4 to group 7) are special. Due to the immiscibility of Mg with these ETMs (see Table 3), the experimental synthesis of these Mg–ETM–H systems, such as systems Mg–Ti–H [134,135], Mg–V–H [135,136], Mg–Cr–H [137], Mg–Mn–H [138,139], Mg–Zr–H [135,140–143], Mg–Nb–H [135,140,141,144,145], Mg–Mo–H [140],

Mg–Hf–H [135,141,143], and Mg–Ta–H [135,141], require the gigapascal hydrogen pressure thermal technique (Figure 6). These compounds tend to collapse after hydrogen desorption because their structural stability is maintained by hydrogen atoms, which act as a glue connecting Mg and TM metals [134,142,145–147] since Mg cannot form a binary alloy with any ETM, as can be seen from Table 3. Thus, the remaining hydrogen atoms in these Mg–TM–H systems are needed to realize partial reversibility, which makes the cycle stability of releasing and restoring hydrogen poor [135,142,146]. A viable solution for the high hydrogen pressure issue for Mg–ETM–Hydrides may be found in the recent DFT calculations for Mg_nTMX_2 ($X = C, N, O, F, P, S$, or Cl ; $TM = Ti, Nb$ or V ; $n = 7$ or 6) with Ca_7Ge type symmetry, which showed that the relatively light nonmetal elements as a “gel”, keeping the structure of Mg_nTMX_2 stable during (de)hydrogenation, not only realize the reversibility of Mg–TM–Hydrides but also maintain the hydrogen storage capacity, e.g., Mg_6VO_2 shows reasonable dehydrogenation temperature (170–246 K) and high hydrogen storage capacity (5.81 mass%) [146]. In addition, the formation energies of $Mg_6TMO_2H_{14}$ and $Mg_6TMS_2H_{14}$ are in the range of -20 to -40 kJ mol $^{-1}$ H_2 [146]. In Table 2, the formation enthalpy ΔH of Mg_7ScH_{16} [148], Mg_7TiH_{16} [147–149], Mg_6TiH_{16} [147], Mg_7VH_{16} [147,148], Mg_6VH_{16} [147], Mg_7ZnH_{16} [149], Mg_7YH_{16} [148], Mg_7ZrH_{16} [148], Mg_7NbH_{16} [147,148], Mg_6NbH_{16} [147], Mg_7PdH_{16} [149], and Mg_7CdH_{16} [149] are calculated by following formulas [147–149]:

$$\Delta H = E_{\text{tot}}(Mg_7TMH_{16}) - 7E_{\text{tot}}(Mg) - E_{\text{tot}}(TM) - 8E_{\text{tot}}(H_2) \quad (5)$$

$$\Delta H = E_{\text{tot}}(Mg_6TMH_{16}) - 6E_{\text{tot}}(Mg) - E_{\text{tot}}(TM) - 8E_{\text{tot}}(H_2) \quad (6)$$

where $E_{\text{tot}}(Mg_7TMH_{16})$, $E_{\text{tot}}(Mg_6TMH_{16})$, $E_{\text{tot}}(Mg)$, $E_{\text{tot}}(TM)$, $E_{\text{tot}}(H_2)$ are the total energies of Mg_7TMH_{16} , Mg_6TMH_{16} , Mg–TM, and H_2 systems in their stable crystal structures as calculated from the first principles, respectively. Mg_2FeH_6 can be formed by mechanical milling of Mg and Fe under hydrogen atmosphere [34,128]. Synthesis of Mg_2FeH_6 is quite difficult, since Mg and Fe cannot form any intermetallics [128]. Similar to the Mg–Fe system, the Mg_2CoH_5 and Mg_3CoH_5 hydride can also be formed from Mg and Co in the presence of hydrogen; however, synthesizing these hydrides is not easy due to the absence of stable precursors such as Mg_2Co or Mg_3Co to produce a single hydride phase, since the only stable intermetallic formed by Mg and Co is $MgCo_2$ [128,150,151]. It is important to highlight that the formation of Mg_2FeH_6 and Mg_2CoH_5 consists of two steps that always involve MgH_2 as a precursor [34]:



These Mg–TM–H ternary hydrides with H as glue are quite sensitive to experimental conditions, such as the sample preparation method, the particle size, temperature, and hydrogen pressure. For example, for core–shell-structured Mg@Co prepared by the reaction of Mg powder in THF (tetrahydrofuran) solution with $TMCl_x$, when Mg powder is prepared by ball-milling, the Mg–Co–H ternary hydride is not observed in XRD patterns (Figure 7a), while when Mg powder is prepared by an Arc Plasma Evaporation apparatus, Mg_2CoH_5 is observed after hydrogenation, and the thermodynamically unstable “ Mg_2Co ” phase is observed after dehydrogenation (Figure 7b). In addition, the Mg_3CoH_5 phase was reported to be synthesized at a temperature between 690 and 710 K under 2 MPa hydrogen pressure [152], while in the work of Lu et al. [117], the formation of the Mg_3CoH_5 phase was observed at 573 K under 2.8 MPa after 10 cycles of hydrogenation (at 573 K under 2.8 MPa hydrogen pressure) and dehydrogenation (under vacuum at 598 K for 2 h) of the core–shell-structured ternary Mg@Co@V composite, which was ascribed by the authors [117] to the fact that the Co particles were of nanoscale size, possibly decreasing the formation temperature of the Mg_3CoH_5 phase.

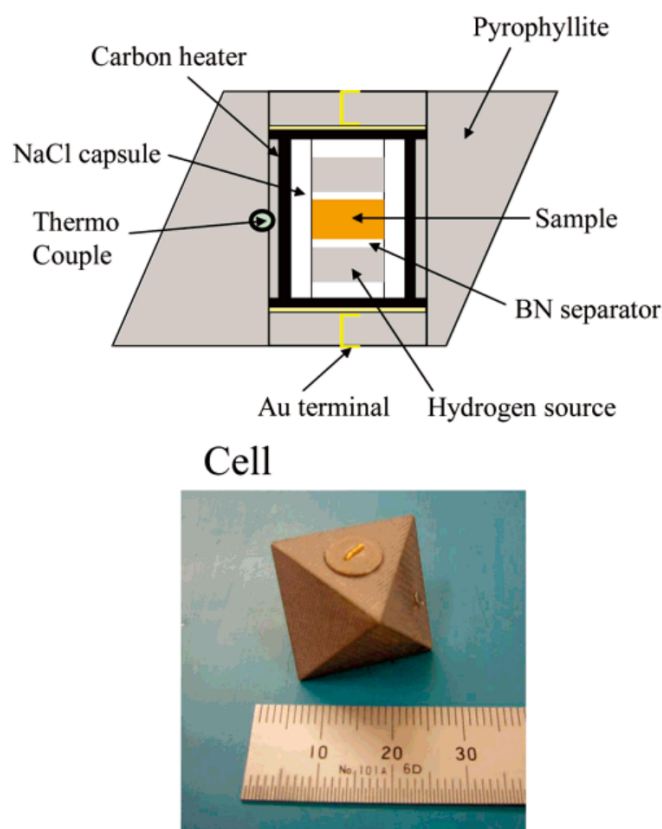


Figure 6. Illustration and photograph of the ultra-high-pressure cell assembly. Reproduced with permission [142]. Copyright 2007, American Chemical Society.

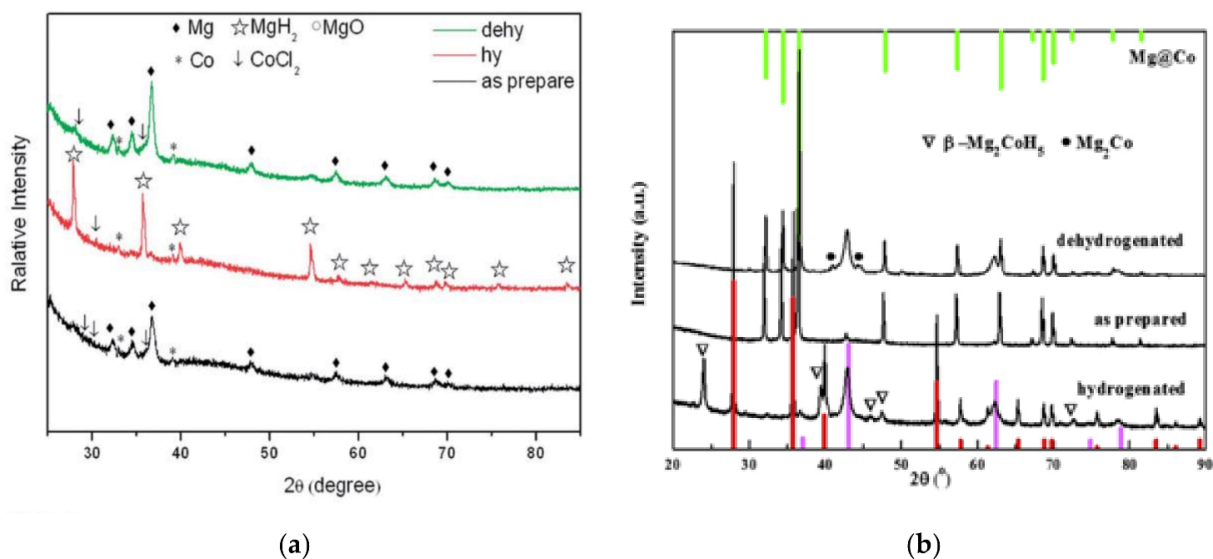


Figure 7. (a) The XRD profiles for the core-shell-structured Mg@Co samples in varying states (as prepared, hydrogenated, and dehydrogenated after 5 cycles). Reproduced with permission [102]. Copyright 2014, Royal Society of Chemistry. (b) XRD patterns of the core-shell-structured Mg@Co composites at different states (as-prepared, hydrogenated, and dehydrogenated after 10 cycles). Reproduced with permission [117]. Copyright 2017, Elsevier.

Table 3. Mg–TM alloy and Mg–TM–H system under thermodynamic equilibrium conditions.

TM	Miscible or Not	Mg–TM Intermetallic Compound	Hydride of Mg–TM Intermetallic Compound	Mg–TM–H Ternary Hydride	Mg–TM–H Ternary Hydride			Ref.
					Chemical Formula	Structure	ΔH ^(c) [kJ mol ^{−1} H ₂]	
Sc	yes	yes	no	yes	Mg ₇ ScH ₁₆	face-centered cubic (FCC) unit cell with Ca ₇ Ge space group	−54.54	[31,148,153]
Ti	no	no	no	yes	Mg ₇ TiH ₁₆	FCC unit cell with Ca ₇ Ge space group	−48.54; −44.8; −69.03	[128,147–149,154]
					Mg ₆ TiH ₁₆	FCC unit cell with Ca ₇ Ge space group	−28.8	
V	no	no	no	yes	Mg ₇ VH ₁₆	FCC unit cell with Ca ₇ Ge space group	−39.38; −40.3	[128,136,147,148,155]
					Mg ₆ VH ₁₆	FCC unit cell with Ca ₇ Ge space group	−26.3	
					Mg ₆ VH _y	cubic F-centered substructure with an additional superstructure related to the Ca ₇ Ge-type structure	-	
Cr	no	no	no	yes	Mg ₃ CrH _x	-	-	[137,156]
Mn	no (a)	no (a)	no (a)	yes	Mg ₃ MnH ₇	space group P6 ₃ /mmc	-	[139,157,158]
Fe	no	no	no	yes	Mg ₂ FeH ₆	-	−77.9	[34,128,159]
Co	yes	yes	not reported	yes	Mg ₂ CoH ₅	-	−82	[117,128,150,151]
Ni	yes	yes	for Mg ₂ Ni, yes	yes	Mg ₃ CoH ₅	-	−70	[34,128,160]
Cu	yes	yes	for Mg ₂ Cu, no	not reported	Mg ₂ NiH ₄	-	−64.5	[34,128,129,161]
Zn	yes	yes	for MgZn, no	yes	-	-	-	
Y	yes	yes	no	yes	Mg ₇ ZnH ₁₆	FCC unit cell with Ca ₇ Ge space group	−29.74	[128,149,162]
					Mg ₇ YH ₁₆	FCC unit cell with Ca ₇ Ge space group	−53.33	
Zr	no	no	no	yes	Mg ₇ ZrH ₁₆	FCC unit cell with Ca ₇ Ge space group	−52.50	[128,140–143,148,164,165]
					Mg ₂ Zr ₃ H _y	monoclinic structure	-	
					MgZr ₂ H _{5,9}	monoclinic structure	-	
					Mg _{0.82} Zr _{0.18} H _x	FCC structure	−73.0 ± 0.8	
					Mg _{4.5} ZrH _x	FCC structure	-	
Nb	no	no	no	yes	Mg ₇ NbH ₁₆	FCC unit cell with Ca ₇ Ge space group	−47.72; −51.1	[128,140,141,145,147,148,166]
					Mg ₆ NbH ₁₆	FCC unit cell with Ca ₇ Ge space group	−25.1	
					Mg ₄ NbH _y	-	-	
					MgNb ₂ H _{5,9}	Monoclinic structure	-	
					Mg _{6.2} NbH _{14.4}	FCC structure	-	
Mo	no	no	no	yes	MgNb ₂ H _{−4}	C-centered monoclinic structure	-	[140,167]
Tc	not reported	not reported	-	not reported	Mg ₃ MoH ₆	hexagonal structure	-	
Ru	no	no	no	yes	-	-	-	
Rh	yes	yes	for Mg ₂ Rh, yes	yes	Mg ₃ RuH ₆	space group Cmcn	-	[168,169]
Pd	yes	yes	for AgMg, no; for AgMg ₃ , no	yes	MgRhH _{1−x}	space group P4/mmm	-	[170–172]
					Mg ₂ RhH _{1,1}	Ti ₂ Ni-type structure (b)	-	
Ag	yes	yes	for AgMg, no; for AgMg ₃ , no	not reported	-	FCC unit cell with Ca ₇ Ge space group	−30.24	[128,149,173]
Cd	yes	yes	no	yes	Mg ₇ PdH ₁₆	-	-	[127,128,174–176]
					-	FCC unit cell with Ca ₇ Ge space group	−27.75	[130,131,149]

(a) The complete Mg–Mn phase diagram has not been determined, except for the Mg-rich region (0 to 3.7 at% Mn), which indicates that Mn is almost immiscible with Mg. Thus, the Mg–Mn intermetallic compound and thereby the hydride of the Mg–Mn intermetallic compound can not be determined. (b) Hydrogen occupies octahedral and tetrahedral voids in the Ti₂Ni-type arrangement of magnesium and rhodium atoms. Retrieval of hydrogen by desorption destabilizes the structure and leads to a binary metal compound of composition Mg₂Rh which crystallizes with the Ti₂Pd-type structure. (c) ΔH represents the formation enthalpy of Mg–TM–H ternary hydride.

3. The Micro-Catalytic Mechanism of TM Dopants on the Hydrogen Desorption Properties of MgH₂

3.1. The Change Trends of Interactions (Ionic and Covalent) in TM-doped MgH₂

A significant amount of theoretical research is concerned with the nature of the interaction between TMs and MgH₂ matrix in TM-doped MgH₂ systems. Ab initio electronic structure calculations of the Mg₁₅TMH₃₂ (TM = entire 3d TM series) conducted by Mamula and coworkers [28] showed well-matched observed trends of TM–nnH distances (Figure 8b), which agrees with the trends of the average TM–H distances in the Mg₁₁TM₂H₂₆ cluster models along the whole 3d metal series [177], and Bader excess charge (BEC) (Figure 8c), which is defined as the difference between the charge contained in a Bader atom and its atomic charge and can be considered as the exact measure of the ion charge in the crystal lattice. Based on the results that the TM–nnnH1 distances have the opposite trend, the authors [28] revealed the screening and compensation of the nnnH1 shell towards the TM-introduced perturbation of the host MgH₂ lattice, which resulted in considerably less pronounced changes in the more distant coordination nnnH2 shell. This conclusion can be evidenced by the results shown in Figure 8c that only the value of ρ_{b3} in the third coordination is approximately the same as in MgH₂, indicating the more prominent influence exerted by the TM dopant on its nearest two coordinations than on other neighbor atoms. As is also shown in Figure 8c, compared with the Mg–H bond, the

TM–H bond is more covalent with the more localized charge in the TM–H bonding region, which leads to the depleted region between the nnH atoms in the TM first coordination and thereby prevents the H–H bonding formed in the rest of the MgH_2 matrix further away from the TM atom [28]. Furthermore, it can be seen that ρ_{b1} obeys the opposite trend to that of the BEC of TM and nnH, suggesting that the decrease in ionic charge on TM and nnH is accompanied by an increase in covalent charge on the TM–nnH bond. Figure 8d demonstrates that generally, the stability of $\text{Mg}_{15}\text{TMH}_{32}$ follows the observed TM–H distances and BEC trends, which is especially pronounced at the beginning and the end of the TM series, but is deviated for Mn, Fe, Co, and Ni. The potential cause is attributed by the authors [28] to the possible excluded magnetic contribution to the stability of compounds caused by the non-polarized-spin manner of all calculations for doped systems. In fact, the spin polarization can exert strong influence on the stability of the Mg–TM–H system, originating from the considerably wider d band and much lower particular peaks than in the non-polarized spin case, which are caused by the high un-symmetric distribution (spin splitting) of the partial DOSs of spin-up and spin-down electrons of TM atoms, such as in Mn (Figure 9a,b [178]) and Co (Figure 9c,d [179]). Furthermore, spin polarization in Mg–TM–H system also changes the position of the Fermi level and the width of the energy gap [179], thereby affecting hydrogen sorption properties. In addition to the magnetic contribution of TM to the stability of compounds, the deviation of the stability of $\text{Mg}_{15}\text{TMH}_{32}$ (TM = Mn, Fe, Co, and Ni) from the observed TM–H distances and BEC trends may also be explained by the contribution of other interatomic interactions other than TM–H interactions, such as nnnMg–nnH interactions, since the spin polarization shows little influence in Ni-doped MgH_2 systems, as neither Mg_2Ni nor its hydride presents magnetic properties [178,180,181].

The DFT investigation conducted by Chen et al. [182] toward the alloying effect of TM on the electronic structure of a MgH_2 cluster containing 33 magnesium atoms and 64 hydrogen atoms demonstrated almost TM-independent atomic ionicities of H(1), H(2), Mg(1), and Mg(2) around TM (Figure 10a,b), indicating that the effect of the substitution of TM for Mg (or alloyed by TM) on the atomic ionicity may be limited in a small area around TM. The fact that in MgH_2 , Mg–H covalent bonding predominates over the covalent bonding of Mg–Mg and H–H has been proved by atomic bond order BO_{AB} analysis, which is used to evaluate the strength of the covalent bond between two atoms A and B and can be calculated by the Mulliken population analysis according to the following equation [182]:

$$\text{BO}_{AB} = \sum_l n_l \sum_{m' \in B} \sum_{m \in A} \alpha_{lm'} \alpha_{lm} S_{m'm} \quad (8)$$

where α_{lm} and $\alpha_{lm'}$ are the coefficients of the atomic orbitals m and m' in the molecular orbital l , $S_{m'm}$ is an overlap matrix element between two atomic orbitals m' and m , and n_l is the occupied charge of the molecular orbital l . As can be seen from Figure 10c the covalent bonds between TM and H atoms (H(1)) and H(2)) are stronger than between TM and Mg atoms (Mg(1), Mg(2), Mg(3), and Mg(4)), similar to those for pure MgH_2 . Comparing Figure 10c,d, one can see that $\text{BO}_{\text{Mg(1)}-\text{H(1)}}$ and $\text{BO}_{\text{Mg(2)}-\text{H(2)}}$ have an inverse trend to $\text{BO}_{\text{TM}-\text{H(1)}}$ and $\text{BO}_{\text{TM}-\text{H(2)}}$ [182]. According to the results demonstrated in Figures 8b,c and 10, the following propositions can be made: (1) the variation of TM–nnH interatomic distance is more significant than that of TM–nnnMg; (2) the variation of ionicities of TM and nnH is more significant than that of nnnMg; (3) the variation of TM–nnH covalent bond is more significant than that of both nnnMg–nnH and TM–nnnMg. Therefore, the influence of TM on the interatomic interaction in TM-doped MgH_2 is mainly reflected in the TM–nnH ionic bond (bigger variation in TM–nnH bond length, TM ionicity, and nnH ionicity), the TM–nnH covalent bond (bigger variation in TM–nnH bond length, ρ_{b1} , and TM–nnH bond order), the nnnMg–nnH ionic bond (nnnMg–nnH length varies significantly as a result of the big variation in TM–nnH bond length and the small variation in TM–nnnMg bond length, ionicity of nnH varies more than that of nnnMg), the nnnMg–nnH covalent bond (nnnMg–nnH length varies significantly or nnnMg–nnH bond order varies significantly in

some TM-doped MgH_2 as shown in Figure 10d), and the TM–nnnMg ionic bond (ionicity of TM varies significantly despite the small variation in both the TM–nnnMg distance and the ionicity of Mg), all of which control $\Delta H(\text{Mg-TM})_{\text{Diff}}$, which is defined as the hydride formation enthalpy difference between ΔH for MgH_2 and ΔH for Mg-TM-H system.

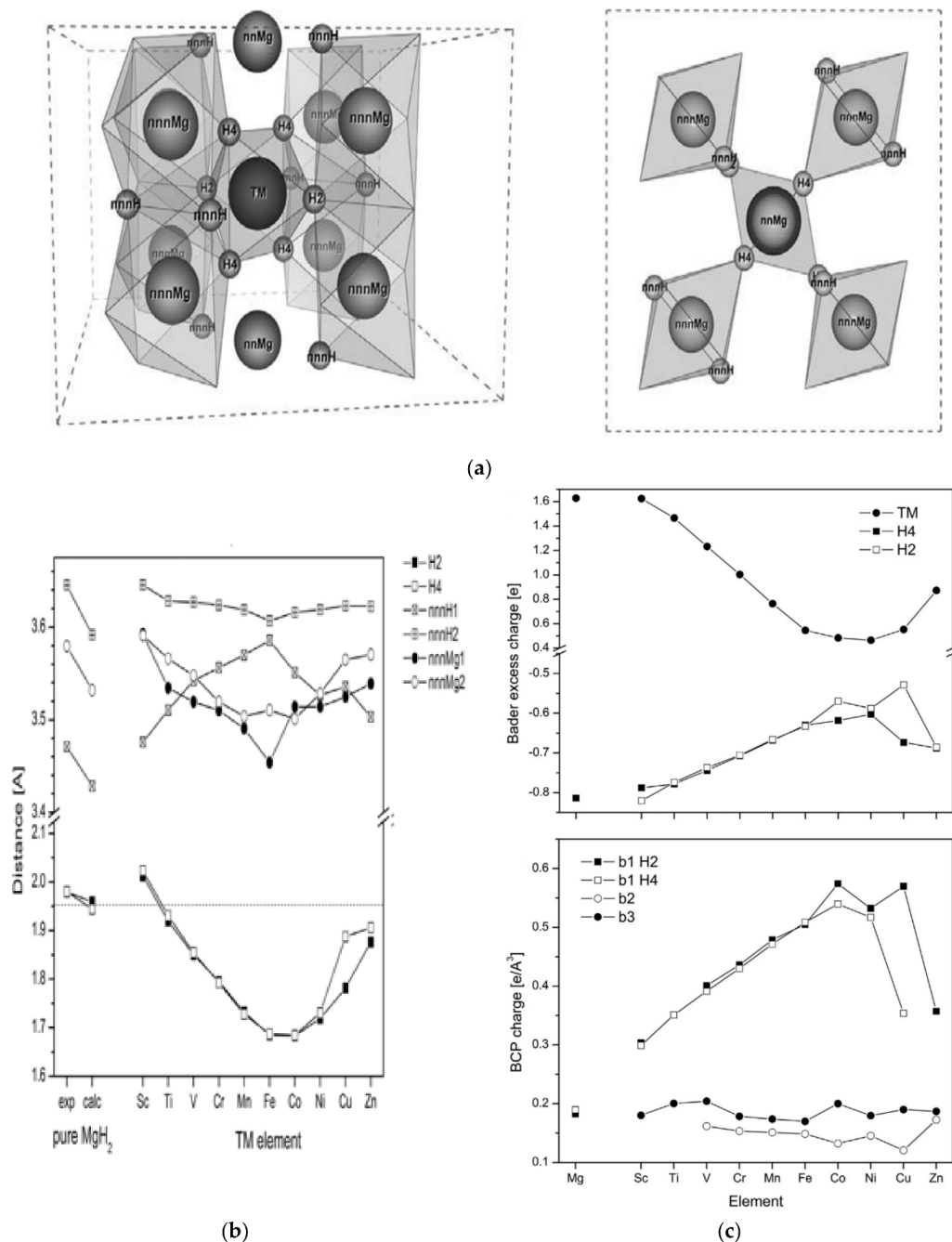


Figure 8. Cont.

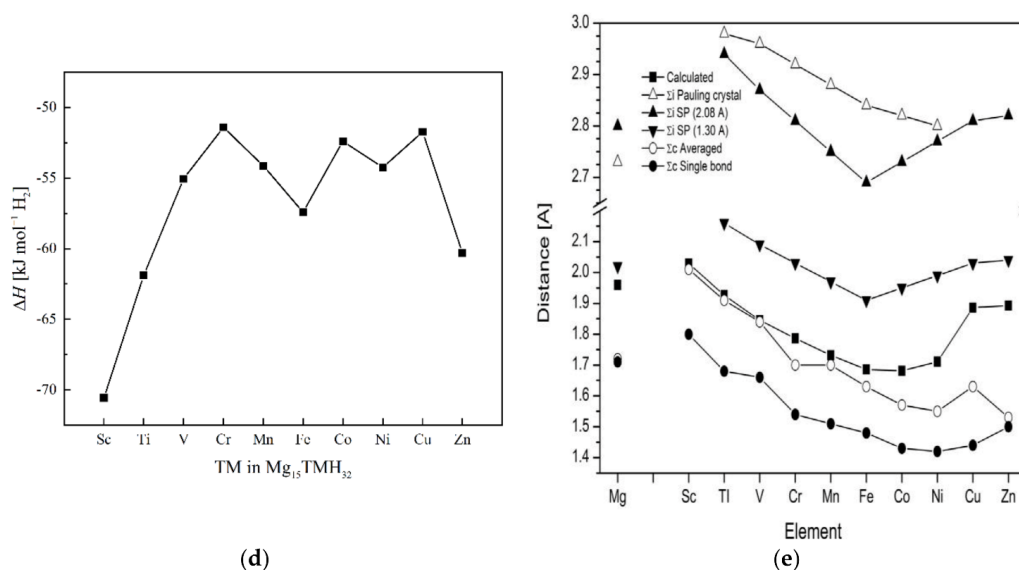


Figure 8. (a) Nearest (nn) and next-nearest neighbor (nnn) atoms of TM, with their coordination polyhedra, side perspective view (left), and top view (right). (b) Relaxed interatomic distances in TM-doped MgH_2 ($\text{Mg}_{15}\text{TMH}_{32}$ system) obtained using Abinit PAW formalism. The nearest neighbor H (nnH) atoms forming the first coordination octahedron are marked as two top and bottom H2 and four coplanar H4 atoms. nnnMg are the nearest and the next nearest Mg atom, while nnnH1 and nnnH2 stand for the next-nearest neighbor H atom. Corresponding experimental and calculated values for pure MgH_2 are given on the left. Dashed lines represent the Mg–nnH (H2 and H4) average relaxed distance in pure MgH_2 compound. (c) Top—BEC on TM and nnH atoms for MgH_2 (left) and entire MgH_2 :TM series. Positive values correspond to charge depletion. Bottom—charge densities (ρ_b) at the specific bonding critical points (bCPs) between TM and nnH atoms (b1), nnH, and nnnMg (b2) and nnnMg and nnnH (b3), corresponding to the first, second, and third coordination of TM. The corresponding ρ_b value in MgH_2 is given for comparison on the left. (d) Enthalpy of formation of $\text{Mg}_{15}\text{TMH}_{32}$. The values come from Table 2, from the work of Mamula and coresearchers. (e) Bond distances obtained from $\text{Mg}_{15}\text{TMH}_{32}$ structures relaxation (calculated) and by summing Pauling crystal and Shannon–Prewitt (SP) effective ionic (Σ_i), averaged, and single-bond (SB) covalent radii (Σ_c). 2.08 Å and 1.30 Å are used as H^- effective ionic radii. (a–e) Reproduced with permission [28]. Copyright 2014, Elsevier.

This proposition can be supported by more current evidence. Figure 11 shows that the strong interaction between Ti and H3 leads to the weakening of the interaction between Mg2 and H3. DFT calculations performed by Zhang et al. [183] showed that the Nb atom doped into MgH_2 interacted with H atom ionic-covalently, leading to lower structural stability and the enhancement of dehydrogenation kinetics in MgH_2 . Although the first-principles study performed by Abdellaoui et al. [22] on Mg_6H_{12} , $\text{Mg}_5\text{LiH}_{12}$, and $\text{Mg}_4\text{BLiH}_{12}$ showed that the stability and also the desorption temperature of the hydride systems depend on the charge quantity received by the hydrogen, such that when the charge received by H decreases, the stability and decomposition temperature decrease, the results presented in Figure 8c,d and Table 4 do not suggest the same correlation. Thus, to evaluate the stability of TM-substituted MgH_2 , the four interactions proposed above are still needed. Unfortunately, the relative contributions of these four interactions on $\Delta H(\text{Mg-TM})_{\text{Diff}}$ may vary in different Mg–TM–H systems. Mamula and coresearchers [28] compared trends of bond distances obtained from $\text{Mg}_{15}\text{TMH}_{32}$ structure relaxation (calculated) and by summing Pauling crystal and Shannon–Prewitt (SP) effective ionic (Σ_i), averaged, and single-bond (SB) covalent radii (Σ_c), found that the calculated distance trend is much better-matched by the distances obtained from the SB covalent radii (systemic deviation is about 0.2 Å), indicating a considerable covalent contribution to the TM–nnH bonding (Figure 8e). It was also reported that the enhanced overlap of the electron cloud between the H atom and the substitutional atom

(Ni, Cu) is accompanied by the weakened electron cloud overlap between the H atom and the other two neighboring Mg atoms [184]. Khatabi et al. [26] observed in the DOS of $\text{Mg}_{15}\text{TMH}_{32}$ (TM = Sc, Ti, V, Cr, Y, Zr, Nb, Mo) that the TM only created a bond with Mg atoms as the result of the hybridization of *s* and *d* orbitals of Mg and TM, respectively (Figure 12), and noted that as long as the difference of the electronegativity of TM and Mg increased, the stability of the $\text{Mg}_{15}\text{TMH}_{32}$ system decreased for TM in the same row of the periodic table of elements. The authors [26] explained this effect by the fact that the increase of the Mg–TM bond strength allows weakening of the Mg–H bond and thereby results in a decrease in system stability, which suggests that the TM–Mg interactions (covalent and ionic), including TM–nnnMg interactions, contribute to the main part of $\Delta H(\text{Mg–TM})_{\text{Diff}}$.

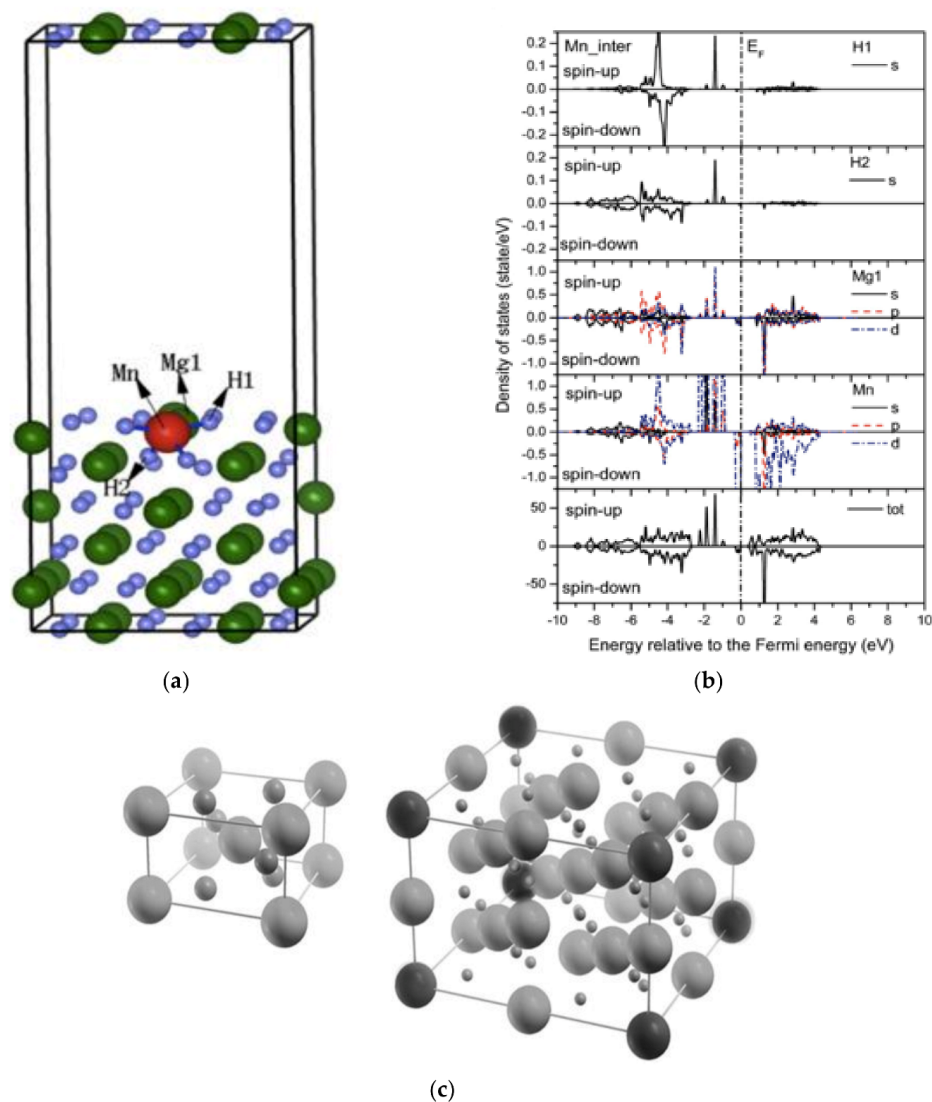


Figure 9. Cont.

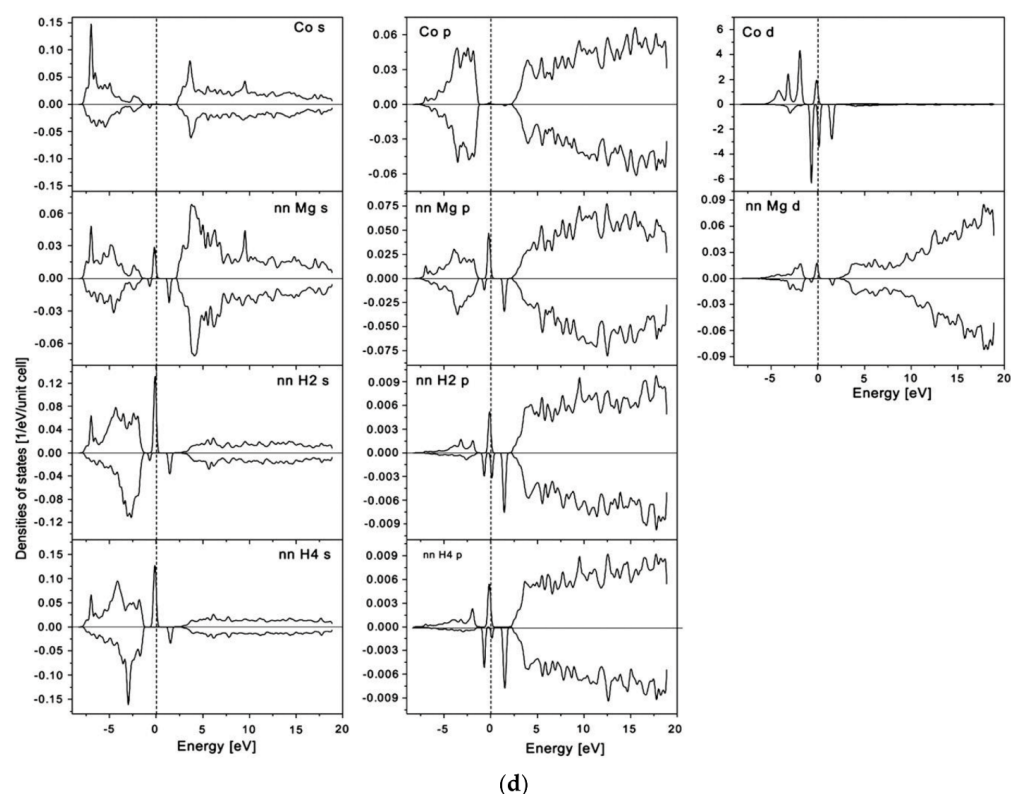


Figure 9. Interstitial occupation of Mn in the $\text{MgH}_2(001)$ surface. (a) The final structure and (b) the total and partial densities of states. The small blue, the medium green, and the large red balls denote H, Mg, and Mn atoms, respectively. (a,b) Reproduced with permission [178]. Copyright 2011, Elsevier. (c) (Left) original unit cell of MgH_2 , (right) $2 \times 2 \times 2$ primitive supercell used in $\text{MgH}_2\text{-TM}$ ($\text{Mg}_{15}\text{TMH}_{32}$) calculations. (d) Orbital momentum decomposition ($l = 0, 1, 2$ correspond to columns 1, 2, and 3, respectively) of spin-polarized $\text{MgH}_2\text{-Co}$ atomic densities of states: Co (top), Co nearest neighbor Mg (second row), and the two non-equivalent Co nearest neighbor H atoms (the two bottom rows). (c,d) Reproduced with permission [179]. Copyright 2009, Elsevier.

Table 4. The charge density of elements, electronegativity of TM, and heat of formation for single substituted Mg-based hydrides $\text{Mg}_{15}\text{TMH}_{32}$ [26].

Systems	MgH_2		$\text{Mg}_{15}\text{ScH}_{32}$		$\text{Mg}_{15}\text{TiH}_{32}$		$\text{Mg}_{15}\text{VH}_{32}$		$\text{Mg}_{15}\text{CrH}_{32}$	
Charges	Mg	1.509+	Mg	1.436+	Mg	1.419+	Mg	1.416+	Mg	1.438+
	H	0.754−	Sc	1.712+	Ti	1.622+	V	1.521+	Cr	1.365+
Heat of formation [$\text{kJ mol}^{-1} \text{H}_2$]		−62.57		−58.63		−51.27		−43.42		−38.79
Electronegativity (Pauling scale)	Mg	1.31	Sc	1.36	Ti	1.54	V	1.63	Cr	1.66
	H	2.20								
Systems	MgH_2		$\text{Mg}_{15}\text{YH}_{32}$		$\text{Mg}_{15}\text{ZrH}_{32}$		$\text{Mg}_{15}\text{NbH}_{32}$		$\text{Mg}_{15}\text{MoH}_{32}$	
Charges	Mg	1.509+	Mg	1.402+	Mg	1.362+	Mg	1.359+	Mg	1.368+
	H	0.754−	Y	2.039+	Zr	2.001+	Nb	1.856+	Mo	1.682+
Heat of formation [$\text{kJ mol}^{-1} \text{H}_2$]		−62.57		−51.07		−47.64		−40.96		−35.96
Electronegativity (Pauling scale)	Mg	1.31	Y	1.22	Zr	1.33	Nb	1.60	Mo	2.16
	H	2.20								

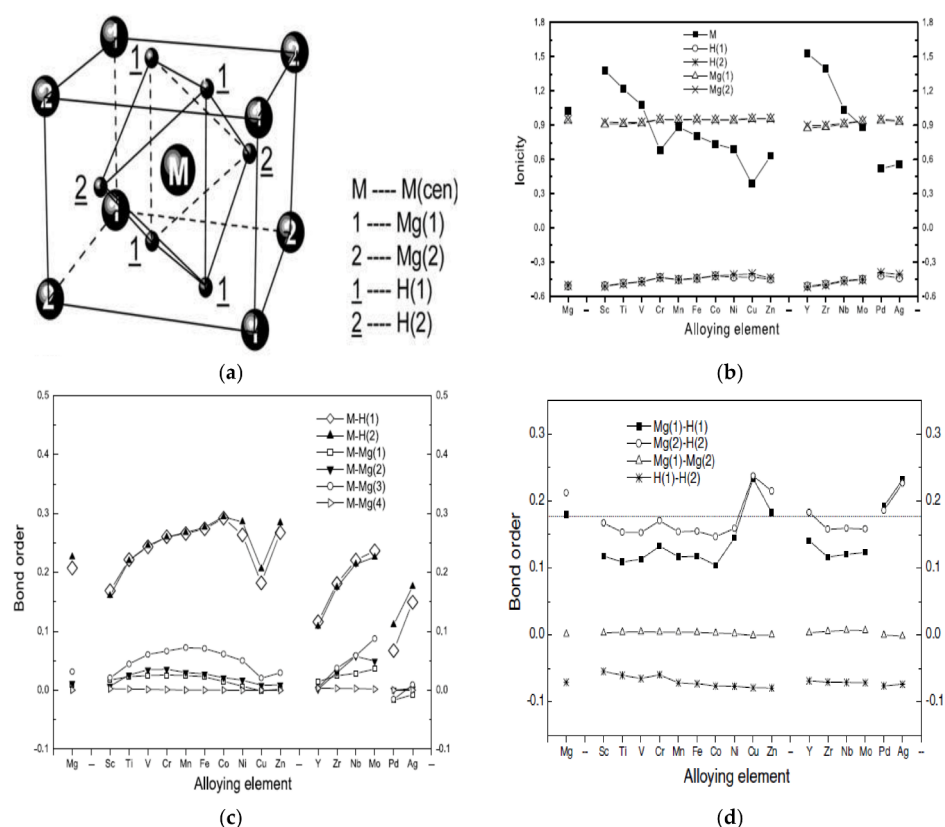


Figure 10. (a) The unit cell marked in cluster model of an alloyed magnesium hydride $\text{Mg}(\text{M})\text{H}_2$ containing 32 magnesium atoms, 1 M atom, and 64 hydrogen atoms with the substitution of the central Mg atom in the cluster by an M atom. As noted above, H(1) and H(2) represent nnH, and Mg(1) and Mg(2) represent nnnMg. (b) Ionicities (net charges according to the Mulliken population analysis) of the central atom M and its adjacent H(1), H(2), Mg(1), and Mg(2) atoms vary with alloying element M in $\text{Mg}(\text{M})\text{H}_2$. (c) Bond order between the central atom M and its adjacent atoms varies with alloying element M. (d) Bond orders BO of the adjacent atomic pairs of Mg(1)–H(1), Mg(2)–H(2), Mg(1)–Mg(2), and H(1)–H(2) to M vary with the alloying element M. In this figure, M is the transition metal (TM) element mentioned in the text. (a–d) Reproduced with permission [182]. Copyright 2003, Elsevier.

Unlike the investigation results of Khatabi et al. [26], the electronic structures of Ni and Y co-doped MgH_2 from the first-principles investigation of Sun et al. [27] show that the hybridization of dopants with Mg and H atom together weaken the Mg–H interaction. In the calculation of $\Delta H(\text{Mg-TM})_{\text{Diff}}$ for MgH_2 and $\text{Mg}(\text{TM})\text{H}_2$ clusters, Chen et al. [182] considered only the contribution of covalent interactions of TM–nnH, ionic interactions of TM–nnH (ionicity difference of TM and nnH), and covalent interactions of nnnMg–nnH and nnnMg–nnnH. The reason for not considering the contribution of ionic interaction of nnnMg–nnH was explained by Chen et al. [182] by taking into account the poor variation of ionicities of nnnMg and nnH with TM (Figure 10b). However, the ionic interaction also depends on the distance between two ions. Unfortunately, Chen et al. [182] did not provide the variation of nnnMg–nnH distance in $\text{Mg}(\text{TM})\text{H}_2$ clusters, and thus, the contribution of the ionic interaction of nnnMg–nnH to $\Delta H(\text{Mg-TM})_{\text{Diff}}$ remains uncertain. For evaluating the nnnMg–nnH interaction (covalent and ionic), the nnnMg–nnH distance is an important parameter, since the BCP charge between nnnMg and nnH (Figure 8c) and the ionicities of nnnMg (Figure 10b) vary indistinctively with TM. For example, DFT studies showed that the distance between Mg and H is larger than that of Ti and H in ordered $\text{Mg}_{0.75}\text{Ti}_{0.25}\text{H}_2$ [185], which agrees with the theoretical investigation of the bonding nature of $\text{Mg}_7\text{TMH}_{16}$ (TM = Sc, Ti, V, Y, Zr, Nb), showing stronger covalent bonding between

TM and H than between Mg and H [148]. In fact, the Mg–H bond length has been widely used to express the Mg–H bond strength, that is, the increase in the Mg–H bond length, which is in general caused by the presence of the TM support, allowing a strong interaction between TM and MgH_2 because of the strong interaction of d electrons with the hydrogen anti-bonding orbital, corresponds to the decrease in the Mg–H bond strength and thereby the reduction of the energy necessary to remove the hydrogen atoms surrounding Mg atoms [30,77,146,185–194].

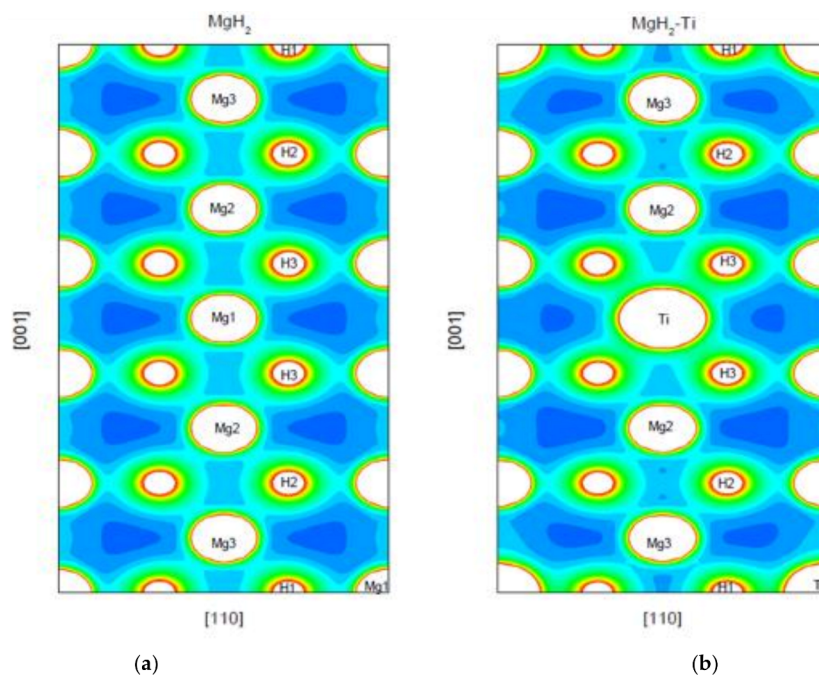


Figure 11. Charge distribution on the (110) plane of the (a) MgH_2 and (b) $\text{MgH}_2\text{-Ti}$. The symmetrically nonequivalent atoms are denoted by numbers 1–3, respectively. (a,b) Reproduced with permission [195]. Copyright 2003, Elsevier.

3.2. The Main Factors Affecting the Change Trends of Interactions (Ionic and Covalent) in TM-doped MgH_2

The discussion in Section 3.1 raised two factors that may influence the interatomic interactions in TM-doped MgH_2 : the d electrons and electronegativity of the TM. A distinct peak was observed near the Fermi level (E_F) in the calculated DOS (Figure 13) of a Mg(Nb)O-MgH_2 system, which was considered by the authors [30] to mainly originate from the contribution of the Nb($4d$) orbital. In addition, the contribution of the Nb atoms to the DOS in the vicinity of the E_F means that the Nb atoms are activation centers, which allows them to somewhat capture the electrons belonging to MgH_2 and consequently induce the charge transfer [190]. In fact, partial substitution of Mg in MgH_2 by a TM atom leads to the appearance of a narrow d band in the middle of the gap with the Fermi level within and thereby the increase in the bonding electron numbers $N(E_F)$ at E_F (a clear state density peak near Fermi level appears) as well as the decrease in the HOMO–LUMO gap near E_F , which makes it possible for the TM– MgH_2 system to obtain metallic characteristics [184,196–199] and reduce the structural stability of MgH_2 [29]. A crucial influence on the strength and length of TM–H bonds in $\text{Mg}_{15}\text{TMH}_{12}$ was reported to be exerted by the areas and directions of accumulation and depletion of the charge density ρ , which depends on the $3d$ orbital nature, such as the splitting of the $3d$ states in the octahedral crystal field, the position of $3d$ states in the DOS, and the Fermi level shift among the split $3d$ states, and is calculated as the difference between the charge obtained self-consistently (SCF) and the superposition of the atomic charges [28]. For example, the different Cu–nnH bond lengths and nature in $\text{Mg}_{15}\text{TMH}_{12}$ was found to be related to the difference between the bCP positions along the Cu–H2 and the Cu–H4 direction originating from the specific charge distribution of the Cu d -states split

in the crystal field of its first coordination [28]. As shown in Figure 14, for TM = Sc, which has only one 3d electron, the 3d band is almost empty, and E_F is at the bottom edge of the band. When the d band fills the 3d states of TM dopants together with a Fermi level shift towards lower energies down to the energy gap for Ti to Ni, typical impurity levels are formed and finally reach the top of the valence band for the almost fully occupied 3d bands of Cu and Zn [28,198]. For a more detailed description of the change trend of the 3d orbital nature, one can refer to reference [28], which suggests that the influence of d electrons on interactions in TM-doped MgH_2 is quite complicated.

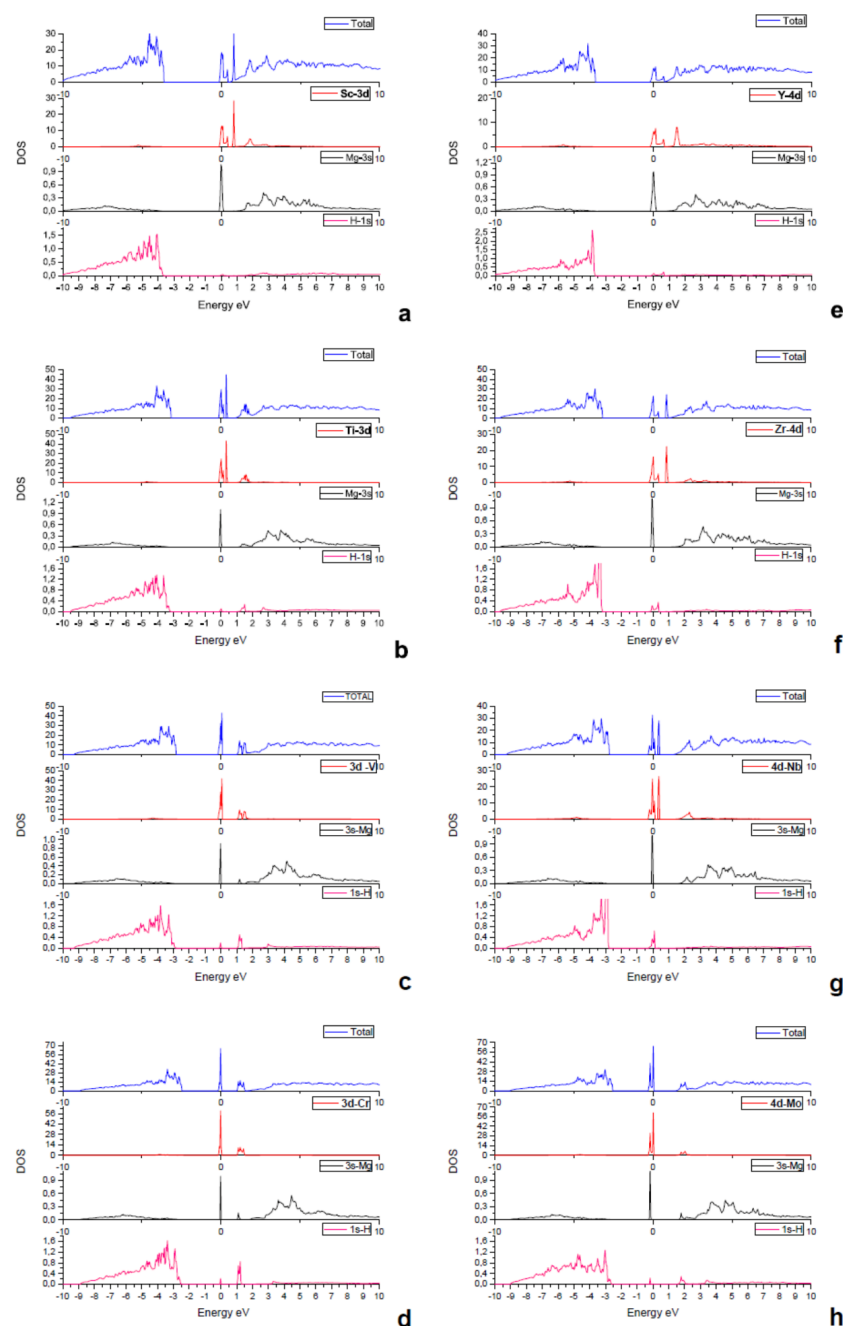


Figure 12. Total and partial density of state (T-DOS and P-DOS) of the systems. (a) $\text{Mg}_{15}\text{ScH}_{32}$. (b) $\text{Mg}_{15}\text{TiH}_{32}$. (c) $\text{Mg}_{15}\text{VH}_{32}$. (d) $\text{Mg}_{15}\text{CrH}_{32}$. (e) $\text{Mg}_{15}\text{YH}_{32}$. (f) $\text{Mg}_{15}\text{ZrH}_{32}$. (g) $\text{Mg}_{15}\text{NbH}_{32}$. (h) $\text{Mg}_{15}\text{MoH}_{32}$. (a–h) Reproduced with permission [26]. Copyright 2016, Elsevier.

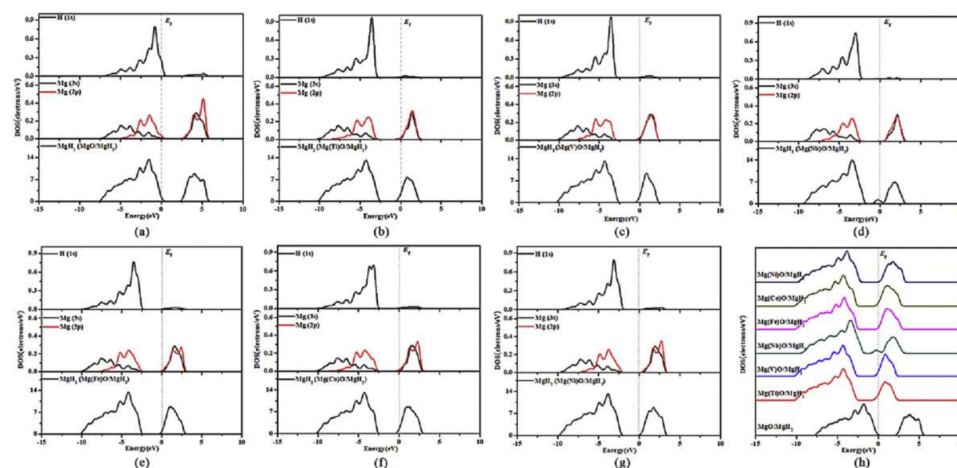


Figure 13. The calculated DOS of different interface models. (a) MgO–MgH₂. (b) Mg(Ti)O–MgH₂. (c) Mg(V)O–MgH₂. (d) Mg(Nb)O–MgH₂. (e) Mg(Fe)O–MgH₂. (f) Mg(Co)O–MgH₂. (g) Mg(Ni)O–MgH₂. h) The comparison of DOS of MgH₂ matrix in different interface models. (a–h) Reproduced with permission [30]. Copyright 2018, Elsevier.

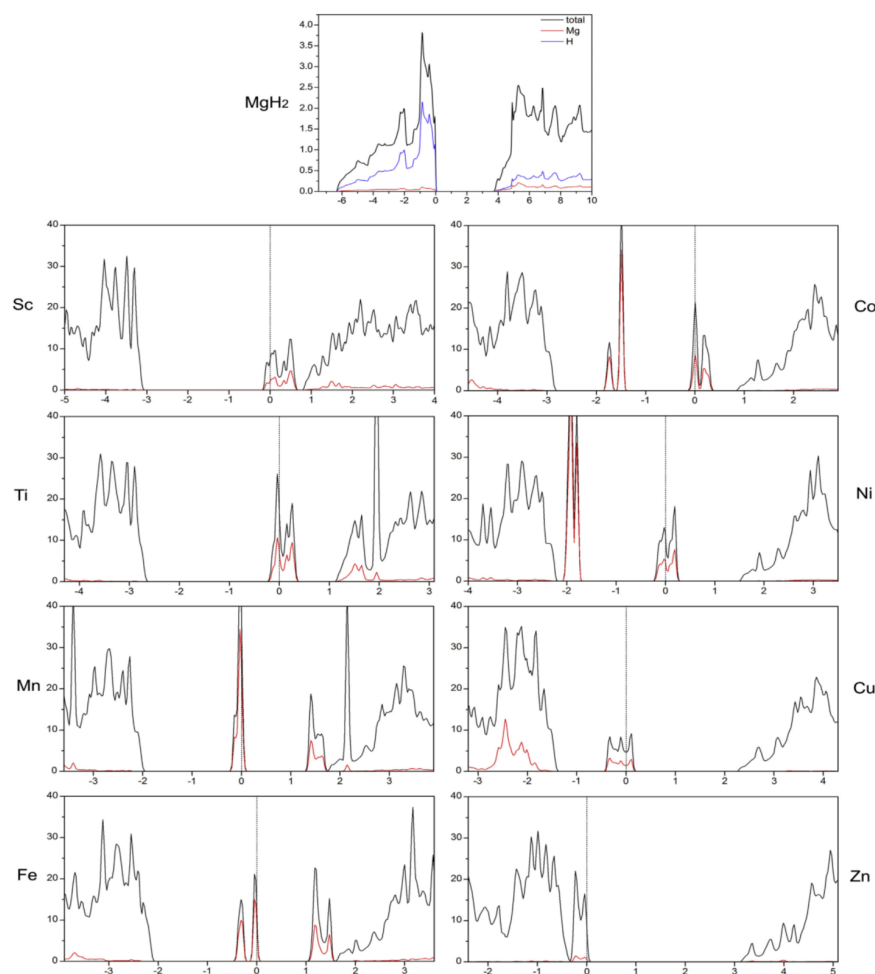


Figure 14. (Top) total and atomic DOS of MgH₂; (bottom) total (black) and TM projected (red) DOS of some of the MgH₂:TM series members (Mg₁₅TMH₃₂). Fermi level is denoted with the dashed vertical line. Only the top of valence and bottom of conduction bands are shown. Reproduced with permission [28]. Copyright 2014, Elsevier.

Based on the Mg–TM (TM = Ti, Nb, V, Co, Mo, or Ni) core–shell-like nanostructures, the electron transfer process in the Mg multi-valence TM system during dehydrogenation was proposed by Cui et al. [102] as containing the following steps: (1) formation of TM–H bonds and nucleation of Mg as a result of the diffusion of 2H^- on the interface between MgH_2 , the TM-based catalyst into the shell, and the simultaneous transfer of two electrons from the TM (the valence of TM changes) to Mg^{2+} ; (2) diffusion of H^- across the nano-shell of the TM-based catalyst onto the surface; (3) the break of the TM–H bond as a result of the transfer of two electrons from two H^- to TM^{2+} (the valence of TM is changed back), leading to the formation of H^0 and thereby the recombination of these two H^0 into a H_2 molecule on the surface of the TM-based catalyst. This redox-like mechanism, in which the multi-valence TM serves as a medium for electron transfer, suggests that the electronegativity (χ) of a TM, which is a measure of the capacity of an atom to entice a bonding pair of electrons, should be the key factor to influence the catalytic effect. Cui et al. [102] revealed that metals bind more strongly with H as χ decreases, which is in accord with the statements of other researchers [200]. This is due to the fact that, for a variation of electronegativity higher than 1.67, the ionic component of the bond predominates, while for a variation of electronegativity of less than 1.67, the covalent component of the bond predominates [26,65]; i.e., the larger the difference of electronegativity between the TM atom and H atom, the stronger the TM–H bonding. However, Cui et al. [102] considered the break of the TM–H bonds to be the control step, which is in conflict with their results (Figure 15), because if the breaking of the TM–H bonds is the control step, then as the χ of TM decreases, the TM–H bonds will become stronger, the breaking of the TM–H bonds will become more difficult, and the hydrogen release rate will thereby decrease. Thus, the control step should be the breaking of the Mg–H bonds [102], which means that compared with the variation of the breaking rate of the TM–H bonds, the variation of the breaking rate of the Mg–H bonds caused by the variation of TM exert more influence on the overall hydrogen release rate. In this way, the results of Cui et al. [102] can be explained as follows: (1) as the χ of TM decreases, the χ -difference between TM and H increases and thereby the TM–H bond strength increases, which decreases the Mg–H bond strength, and thus, the activation energy for dehydrogenation decreases (Figure 15b); (2) Cui et al. [102] believed that the lower the formation enthalpy of TM hydrides, the stronger the interaction between TMs and hydrogen; thus, the activation energy for dehydrogenation increases with the increase in the formation enthalpy of TM hydrides (Figure 15c).

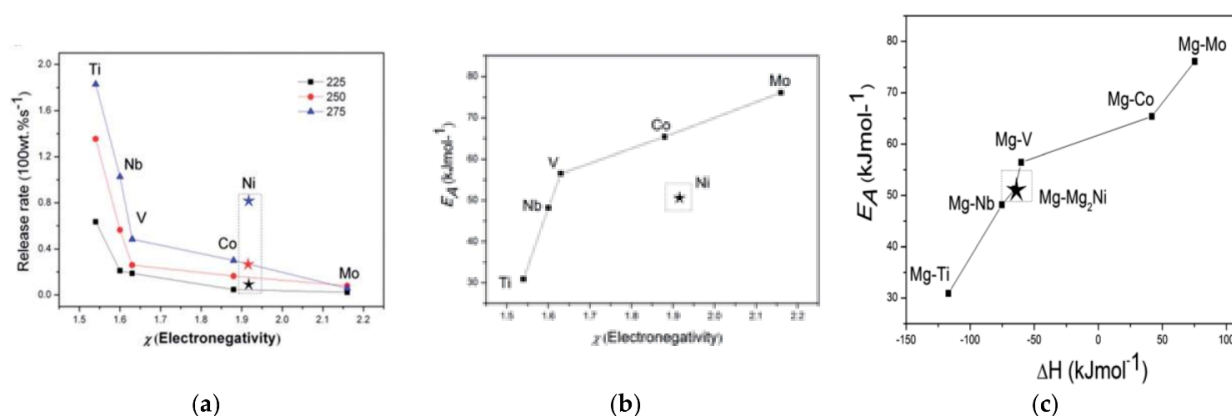


Figure 15. (a) Comparison in dehydrogenation average kinetics within 5 minutes of Mg–TM samples at 225, 250, and 275 °C. (b) Plot of E_A (activation energy for dehydrogenation) in Mg–TM systems vs. χ of TM. (b) Plot of E_A in Mg–TM systems vs. formation enthalpy of TM hydrides (TMH_x). (a–c) Reproduced with permission [102]. Copyright 2014, Royal Society of Chemistry.

3.3. Qualitative Analysis of the Effect of $\chi(\text{TM})$ on the Strength of Mg–H and TM–H Bond

Compared with the “ χ rule”, the regularity of the influence of d electrons on interactions in TM-doped MgH_2 is not that strong. According to the work of Khatabi et al. [26]

mentioned in Section 3.1 and the work of Cui et al. [102] mentioned in Section 3.2, the general “ χ rule” can be defined as follows: the increased χ -difference between TM and Mg and the increased χ -difference between TM and H enhance TM–Mg and TM–H bond strength, respectively, and thereby weaken Mg–H bond strength. Since there is no consensus on whether the control step is the breaking of TM–H bonds or Mg–H bonds, the effect of $\chi(\text{TM})$ on the overall hydrogen release rate in the TM-doped MgH_2 should be described for two cases. If the breaking of TM–H bonds is the control step, the overall hydrogen release rate will increase only with the decrease of χ -difference between TM and H, while if the breaking of Mg–H bonds is the control step, both the χ -difference between TM and Mg and the χ -difference between TM and H should be considered to estimate the overall hydrogen release rate. Consider TMs in the fourth and fifth periods as an example (Figure 16): (1) when the χ of TM is in zone A, then as the χ of TM increases, both $\chi(\text{H}) - \chi(\text{TM})$ and $\chi(\text{Mg}) - \chi(\text{TM})$ decrease; (2) when the χ of TM is in zone B, then as the χ of TM increases, $\chi(\text{H}) - \chi(\text{TM})$ decreases and $\chi(\text{TM}) - \chi(\text{Mg})$ increases; (3) when the χ of TM is in zone C, then as the χ of TM increases, both $\chi(\text{TM}) - \chi(\text{H})$ and $\chi(\text{TM}) - \chi(\text{Mg})$ increases. It seems that when the χ of TM is located in zone A and zone C, the Mg–H bond strength changes monotonously with the increase of the χ of TM, but it should be noted that, to date, there are no studies showing that the simultaneously decreased/increased TM–H and TM–Mg bond strength will always increase/decrease the Mg–H bond strength. All of these issues make the qualitative analysis of the stability of the Mg–TM–H system a complex problem.

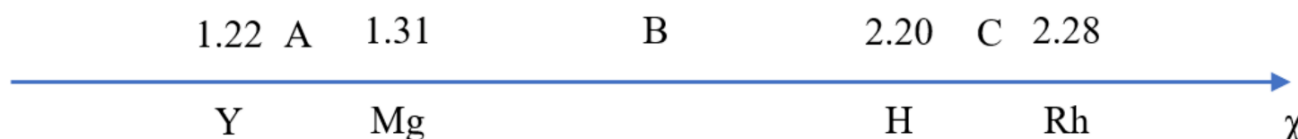


Figure 16. Electronegativity (Pauling scale) of d-TM.

The effect of $\chi(\text{TM})$ on the change trend of charge densities of TM and H in TM-doped MgH_2 is an important topic for study, despite the difference in results showing that the Mg–H interaction in MgH_2 is mainly determined by the ionicity of Mg and H (Figure 17) and that the charge densities of TM and H play a more dominant role for evaluating the ionic interaction of TM–H, Mg–H, and TM–Mg since the variation of charge densities of Mg with TM in TM-doped MgH_2 is negligible (as discussed in Section 3.1). For TM-substituted MgH_2 (Table 5), the Bader population analysis showed that as $\chi(\text{TM})$ increases, the charge density of H and TM almost monotonically decreases. The reason for this phenomenon may be as follows [128]: as $\chi(\text{TM})$ increases, the TM receives more electron charge from Mg atoms, and consequently, the charge density on hydrogen atoms decreases, which results in less available electron charge for hydrogen atoms to use for binding in the structure, and thereby, the hydrogen binding becomes weaker. Based on this and the discussion in Section 3.1, the “ χ rule” of charge transfer in the TM-substituted MgH_2 can be proposed as the following: the charge transfer caused by the variation of $\chi(\text{TM})$ occurs mainly between the central TM, nnH, and nnnMg, and as $\chi(\text{TM})$ increases, the positive charge density of TM and the negative charge density of hydrogen atoms decrease.

Table 4 shows that the variation of charge density of TM and H with TM does not fully agree with the “ χ rule”. We believe that this phenomenon can be explained based on the effect related to the radius of TM. For convenience, we arranged the data in Table 4 into Figure 18 and propose a “radius effect” on the change trend of charge density of TM and H as described below.

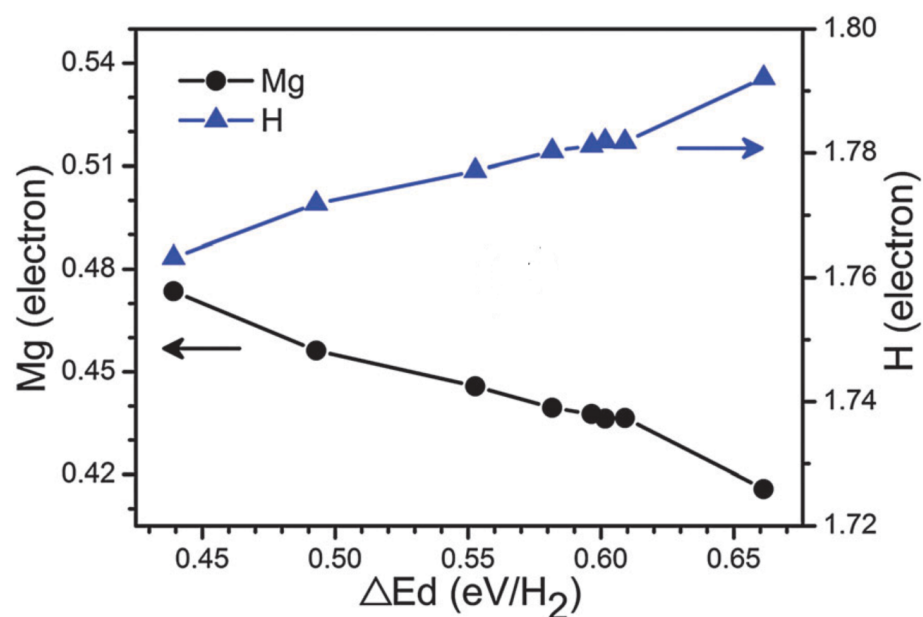


Figure 17. Hydrogen desorption energy ΔE_d (eV per H_2) as a function of average electron numbers around Mg and H atoms of MgH_2 nanowires and the bulk MgH_2 crystal. Reproduced with permission [201]. Copyright 2016, Royal Society of Chemistry.

Table 5. Calculated charge density on hydrogen, Mg, and X (X = V, Nb, Fe, Ni, and Pd) together with the electronegativity of additives. Reprinted/adapted with permission from Ref. [128]. Copyright 2016, Royal Society of Chemistry.

X (in $MgXH_4$)	Radius of X [pm] ^(a)	Electronegativity of X ^(b)	Charge Density		
			H	Mg	X
Mg	150	1.31	−1	+2	−
V	135	1.63	−0.88	+2	+1.50
Nb	145	1.6	−0.82	+2	+1.30
Fe	140	1.83	−0.72	+2	+0.88
Co	135	1.88	−0.65	+2	+0.60
Ni	135	1.91	−0.63	+2	+0.50
Pd	140	2.20	−0.58	+2	+0.30

^(a) These data represent the empirical radius of Mg and TM dopants from reference [125]; ^(b) These data represent the electronegativity (Pauling scale) of Mg and TM dopants from reference [202,203].

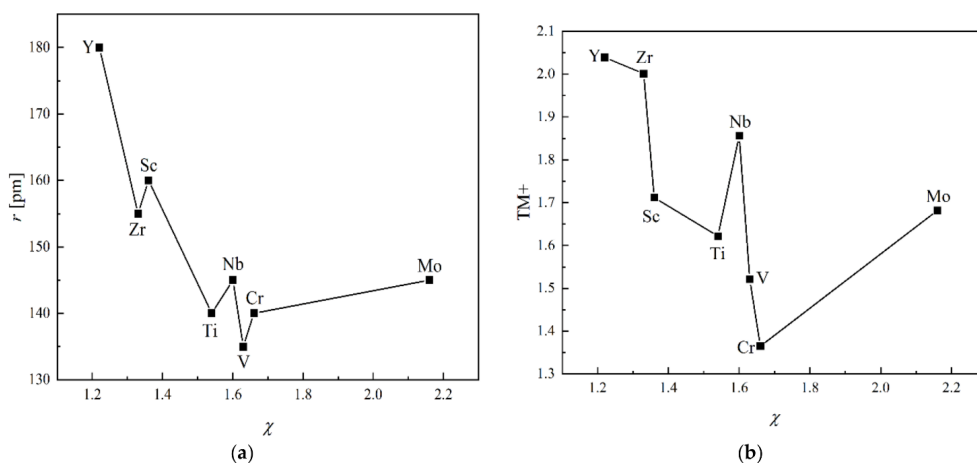


Figure 18. Cont.

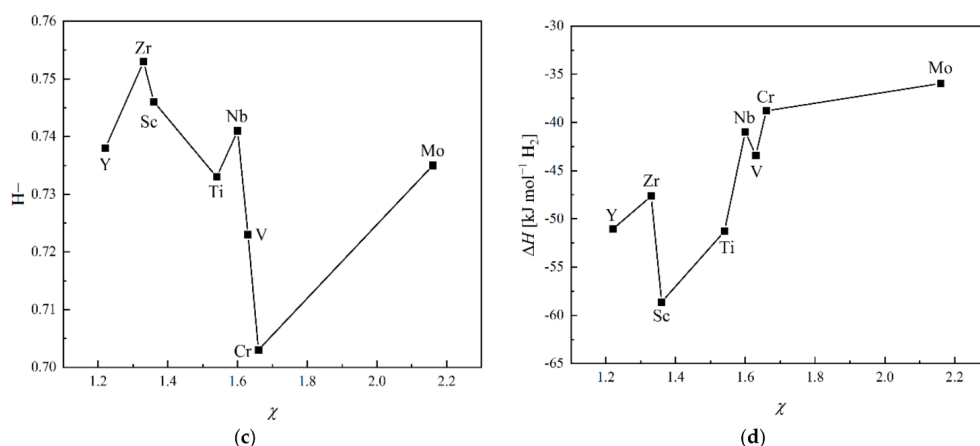


Figure 18. (a) The empirical radius (r) and electronegativities (χ , Pauling scale) of TM elements. The empirical radii of TM elements come from reference [125]. The electronegativity (Pauling scale) of TM dopant elements come from reference [202,203]. Charge densities of (b) TM and (c) H in $Mg_{15}TMH_{32}$ are presented in Table 4. (d) Heat of formation of $Mg_{15}TMH_{32}$ is presented in Table 4.

1. When TM has a radius below 140 pm (including 140 pm), such as in Ti, V, and Cr, the “ χ rule” plays the dominant role for electron transfer, and thus, in Figure 18, $H-(Ti) > H-(V) > H-(Cr)$ and $Ti+ > V+ > Cr+$.
2. When the TM has a radius of $140 < r \leq 155$ pm, such as in Zr, Nb, and Mo, the “radius effect” plays the dominant role for electron transfer. The increased driving force for electron transfer from TM to nnH induced by the increased TM radius is larger than other driving forces for electron transfer between TM, nnH, and nnnMg, which leads to an increase in the negative charge density of H and the positive charge density of TM with increases in TM radius. In Figure 18, $r(Zr) > r(Nb)$, and thus $H-(Zr) > H-(Nb)$ and $Zr+ > Nb+$. $r(Nb) = r(Mo) = 145$ pm, and thus, the charge density varies according to the “ χ rule”; i.e., $H-(Nb) > H-(Mo)$ and $Nb+ > Mo+$.
3. When the TM has a radius of $155 < r \leq 160$ pm, such as in Sc, the lattice begins to expand, which offsets the effect of the increase in the radius from Zr to Sc, and thus, the charge density varies according to the “ χ rule”; i.e., $H-(Zr) > H-(Sc)$ and $Zr+ > Sc+$.
4. From Sc to Y, the “radius effect” can be ignored, because the degree of lattice expansion is much greater than that of the increase in radius, which causes an increase in the interatomic distance and thereby hinders the electron transfer between TM, nnH, and nnnMg.

Thus, even if $\chi(TM)$ decreases, the negative charge density on H is still reduced. However, both the lattice expansion and the decreased $\chi(TM)$ hinder the electron transfer from nnnMg to TM, and thus, the positive charge density on TM increases. In fact, the $r(TM)$ located at the boundary of the two radius intervals proposed above can be considered to belong to either the lower radius interval or the upper radius interval, which does not affect the interpretation of the data. Based on this proposal, the change trend of the charge density of TM and H in Table 5 can be completely explained: for V, Fe, Co, Ni, and Pd with radius $r \leq 140$ pm, the charge densities of TM and H are controlled by the “ χ rule”, which leads to the decrease in the charge densities of TM and H with the increase in $\chi(TM)$, while for Nb, Fe, and Pd with a radius in the range of 140–155 pm, the charge densities of TM and H are controlled by the “radius effect”, which gives rise to the larger charge densities of TM and H in $MgNbH_4$ than those in $MgFeH_4$ and $MgPdH_4$. However, it should be noted that the proposal fails to completely explain the BEC of TM in Figure 8c and the ionicity of TM in Figure 10b, because according to the proposal, the relationship of $Ti+ > Mn+ > V+ > Zn+ > Cr+ > Fe+ > Co+ > Cu+ > Ni+ > Pd+$, $Zr+ > Nb+ > Mo+ > (Ti+, Mn+, Cr+, Fe+, Pd+)$, $Zr+ > Sc+ > Ag+$ and $Y+ > (Sc+, Ag+)$ should be obtained from Figure 19. In addition, the ionicity of nnH varies with TM more obviously in Figure 8c

than in Figure 10b, and the change trends of ionicity of TM do not exactly match in Figures 8c and 10b. These differences between the proposition and results of charge densities of TM and H in Figures 8c and 10b may be attributed to the difference in doping content and *d*-electron of TM, since the proposal is based on Table 4, which only presents results for ETMs with few *d*-electrons.

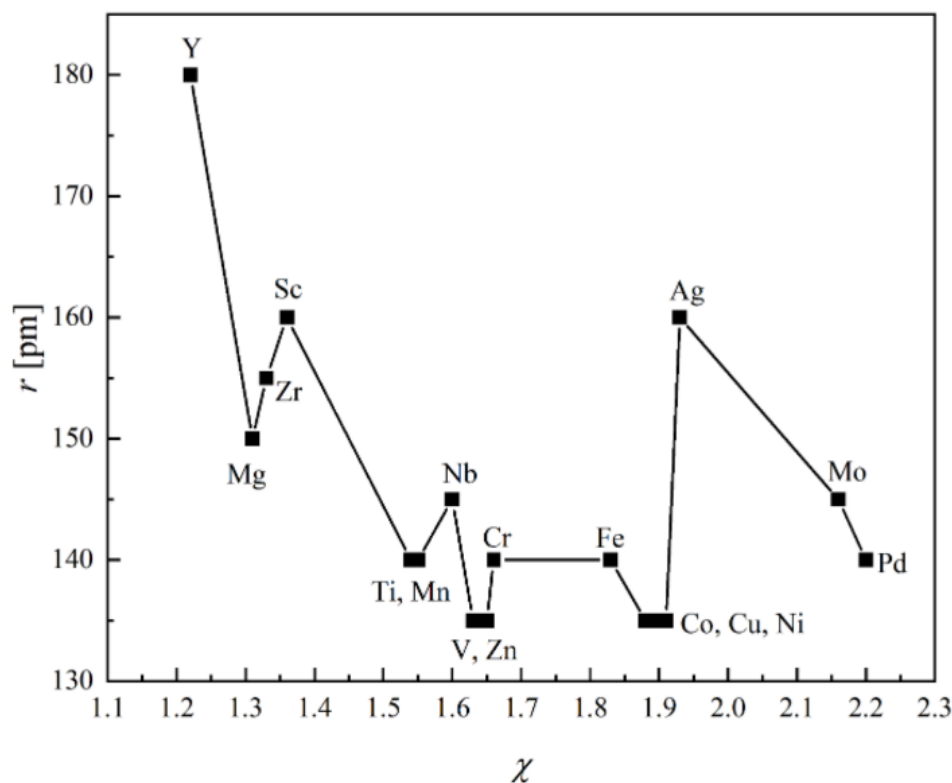


Figure 19. The empirical radiuses (r) and electronegativities (χ , Pauling scale) of Mg and TM elements. The empirical radius of Mg and TM elements come from reference [125], and the electronegativity (Pauling scale) of Mg and TM elements come from reference [202,203].

For TM-adsorbed MgH_2 , such as point-contact TM@Mg (Figure 20a), the TM@Mg of the core-shell structure (Figure 20a), and TM/MgH_2 film, a different, simpler mechanism can be expected. As can be seen from Table 6, compared with the TM atoms that substitute Mg atoms, TM atoms that are adsorbed on the surface of MgH_2 more weakly interact with adjacent atoms. Bader charge distribution analyses performed by Wang et al. [32] demonstrate that the electron redistribution in NbTi clusters increases the ability of the Nb atom to donate electron to H atom, which is believed by the authors [32] to facilitate the break of Mg–H bonding. Note that the NbTi– MgH_2 interface demonstrated in the microstructure of the milled NbTiC-containing MgH_2 sample (Figure 20b) and the calculation model (Figure 20c) in the work of Wang et al. [32] is similar to the TM– MgH_2 interface demonstrated in TM@MgH_2 core-shell-like structure (Figure 20a); thus, it can be proposed that for TM-adsorbed MgH_2 , the charge transfer between surface-adsorbed TM and the surface H controls the overall charge transfer process, and as $\chi(\text{TM})$ decreases, the electrons transferred from TM to the surface H increase, which leads to the weakening of the surface Mg–H bond. Although this proposal can also explain the results for the dehydrogenation properties of the core (MgH_2)-shell (TM)-like structure demonstrated in Figure 15, it is different from the proposal originating from Table 5 that as χ^{TM} increases, the TM receives more electron charge from Mg atoms, and consequently, the charge density on hydrogen atoms decreases, which indicates that the charge transfer between TM and Mg controls the overall charge transfer process. As the authors [32] did not give an explanation for how the

increase in the ability of Nb atoms to donate electron to H atoms can facilitate the break of Mg–H bonding, we offer two explanatory propositions for this phenomenon:

1. The increase of the ability of Nb to donate electron to H leads to the increase in positive and negative charge densities of TM and H, respectively, thereby leading to the increase in TM–H bond strength and decrease in Mg–H bond strength. This proposition agrees with the general “ χ rule” defined in this section.
2. By analogy with the proposal originating from Table 5, TM atoms contribute more electron charge to H atoms, and consequently, the charge density on Mg atoms decreases, which results in less available electron charge for Mg atoms for binding in the structure and thereby, weaker Mg binding. This agrees with the “ χ rule” of charge transfer in the TM-substituted MgH_2 , that as $\chi(\text{TM})$ increases, the positive charge density on TM and the negative charge density on hydrogen atoms decreases, while the positive charge density on Mg increases. The above qualitative analysis shows that the contribution of the “ χ rule” to the charge transfer trend between TM, H, and Mg, and thereby to the interactions in the Mg–TM–H system, is the same for TM-substituted and adsorbed MgH_2 . However, further investigations are required to verify this proposal, as theoretical study on the charge density on TM, H, and Mg in TM-adsorbed MgH_2 systems remains rare.

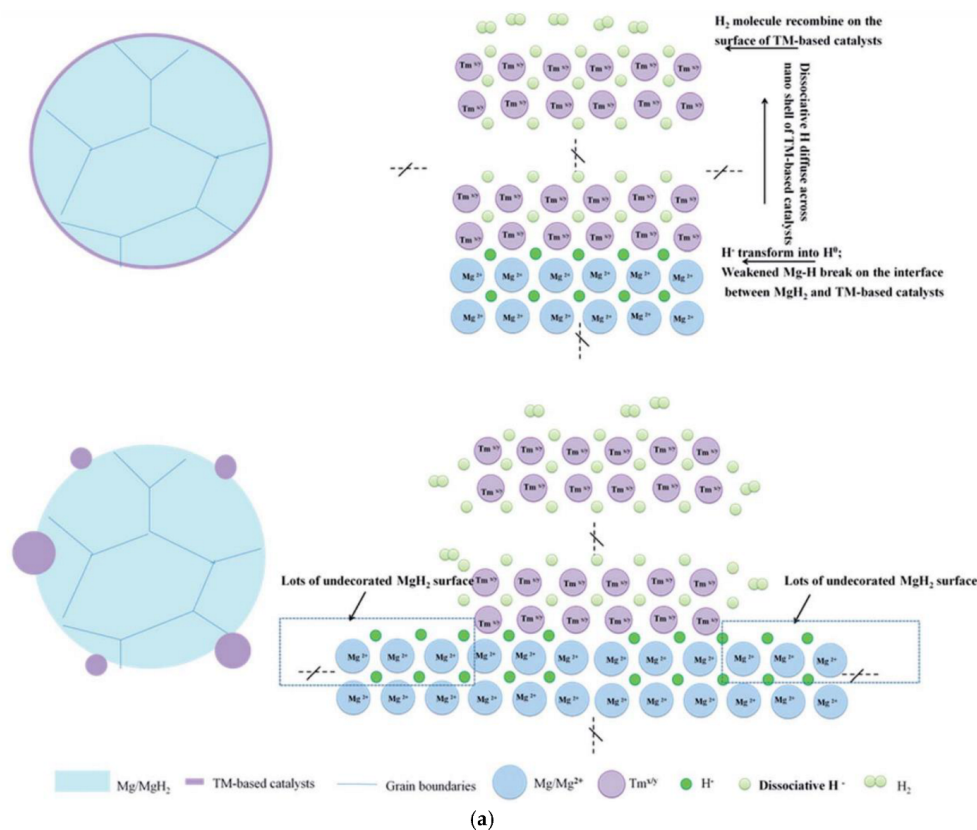


Figure 20. Cont.

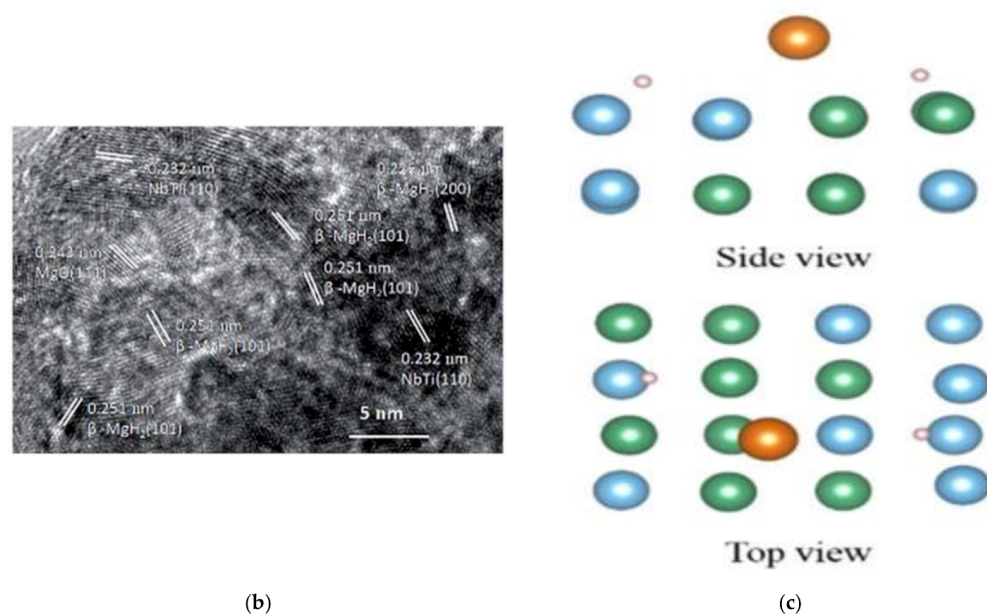


Figure 20. (a) A section schematic diagram of the TM@Mg core-shell structure and point-contact TM@Mg. Reproduced with permission [102]. Copyright 2014, Royal Society of Chemistry. (b) High-resolution transmission electron microscopy (HRTEM) of NbTiC–MgH₂ composite. (c) The optimized geometrical structures of MgH₂ adsorbed on (110) surfaces of NbTi, with Mg atoms in orange, H atoms in pink, Nb atoms in green, and Ti atoms in blue. (b,c) Reproduced with permission [32]. Copyright 2019, Royal Society of Chemistry.

Table 6. The binding energy of substitution of TMs at the first, second, and third layer and on-surface adsorption (in eV) at Mg (0001) surface with the substituted Mg placed on the new surface. E_{on} represents binding energy for TMs adsorption on the Mg surface; E_1 , E_2 , and E_3 represent TMs substituting one Mg atom from the first, second, and third layer, respectively. Reprinted/adapted with permission from Ref. [204]. Copyright 2014, Elsevier.

TM	E_{on} [eV atom ^{−1}]	E_1 [eV atom ^{−1}]	E_2 [eV atom ^{−1}]	E_3 [eV atom ^{−1}]
Sc	−2.260	−3.326	−3.532	−3.463
Ti	−2.050	−4.019	−4.030	−3.905
V	−3.648	−5.824	−5.856	−5.735
Cr	−0.871	−1.389	−1.135	−1.081
Mn	−0.395	−1.711	−1.279	−1.264
Fe	−2.279	−3.445	−3.104	−3.042
Co	−2.824	−4.432	−3.612	−3.485
Ni	−3.692	−4.998	−4.128	−4.032
Cu	−2.570	−3.154	−2.497	−2.454
Zn	−0.513	−0.641	−0.354	−0.302
Y	−2.613	−3.558	−3.664	−3.481
Zr	−2.998	−4.997	−5.411	−5.313
Nb	−2.310	−5.033	−5.292	−5.136
Mo	−4.618	−7.712	−7.604	−7.557
Tc	−5.894	−8.724	−8.395	−8.397
Ru	−4.756	−7.061	−6.651	−6.667
Rh	−4.850	−6.685	−6.055	−6.015
Ag	−2.199	−2.437	−2.171	−2.152
Pd	−3.780	−4.781	−4.240	−4.176
Cd	−0.480	−0.386	−0.290	−0.271

4. The Micro-Catalytic Mechanism of TM Dopants on the Hydrogen Adsorption Properties of Mg

Surface doping of TM atoms in the form of adsorption (Figure 21a) and substitution (capped (Figure 21b) or not capped (Figure 21c) by the kicked-out Mg atom) can improve the hydriding performance of Mg for hydrogen storage. However, due to hydrogen molecular dissociation on the surface, hydrogen atom penetration through the surface, and hydrogen atom subsurface diffusion, the TM catalytic mechanism for surface doping is more complicated than that for volume doping; the underlying mechanism is still unclear. As shown in Figure 21c, the dissociation of molecular hydrogen on the surface of TM-doped Mg goes through an initial state (IS), transition state (TS), and final state (FS). In the IS, there are no overlaps between the molecular hydrogen orbitals and orbitals of the TM-doped Mg surface. In the TS, instead, when molecular hydrogen dissociates on the TM-doped Mg surface, there are overlaps between TM-doped Mg surface and molecular hydrogen orbitals, especially between TM *d* orbitals and molecular hydrogen orbitals [187,204]. This overlap between the H₂ molecule and the TM atom is a quasi-molecular interaction called Kubas bonding that has an interaction energy that is often above 0.5 eV (48 kJ mol^{−1} H₂). It occurs as a result of molecular polarization and multiple σ -bonding instances between the H₂ molecule and the *d* orbitals of the TM atoms, as described in the paragraph that follows.

The electrons in the H₂ bonding (σ) orbital can be transferred to the unfilled *d* orbitals of the TM via overlapping H₂ σ and TM filled *d* orbitals; meanwhile, the *d* electrons of TM can be transferred to the antibonding orbital (σ^*) of H₂ via the overlapping effect between H₂ σ^* and TM unfilled *d* orbitals. These two overlapping effects make the TM act as a bridge to transfer electrons from the bonding orbital of molecular hydrogen to its anti-bonding orbital. The overall effect is called the bridging effect of the *d* orbital, which causes the H₂ bonding orbital to be weakened and the energy barrier of H₂ dissociation to be reduced (Figure 22) [16,18,64,110,187,205]. Thus, the adsorbed hydrogen atoms can spill over onto the surface of Mg particles according to the reverse “spillover” mechanism (Figure 23) [36,53,206–209]. For example, theoretical calculations have shown that the activation barrier for the hydrogen dissociation on the V-doped Mg(0001) surface is only 0.20 eV (19 kJ mol^{−1} H₂) [210].

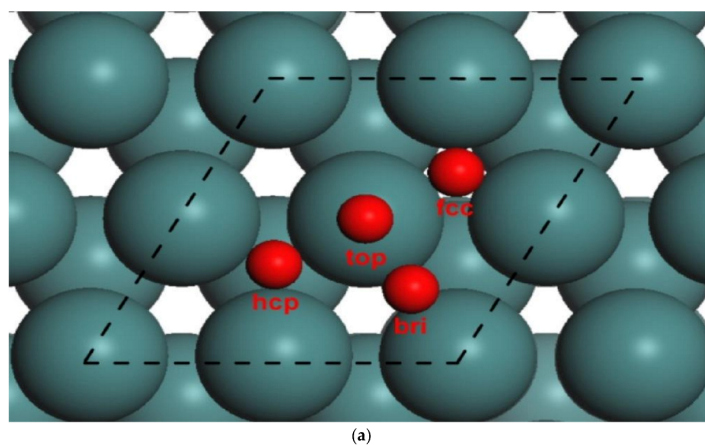


Figure 21. Cont.

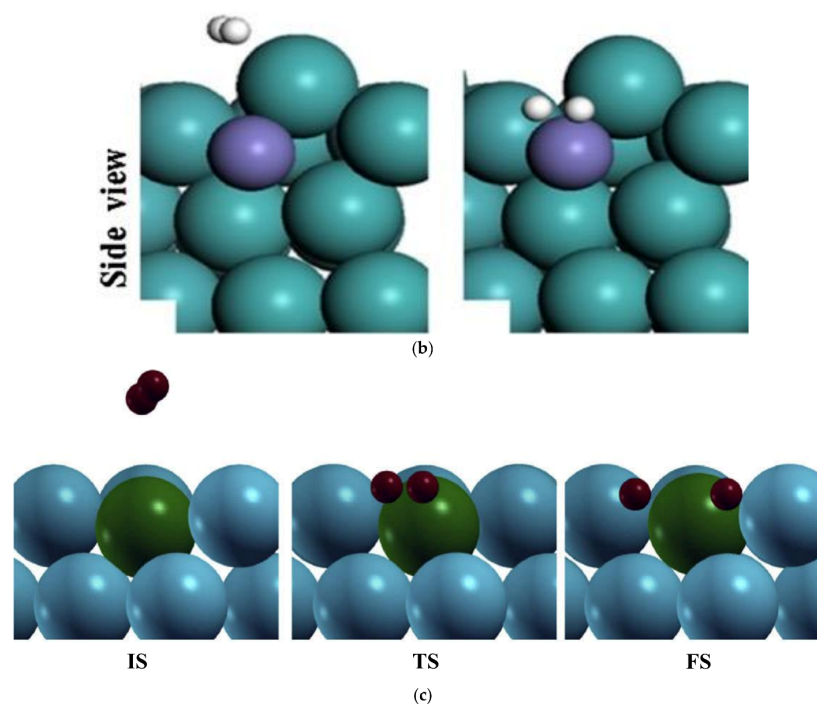


Figure 21. (a) Top view of four on-surface adsorption sites on the Mg(0001) surface. Dark blue balls denote Mg atoms, and red balls represent the four different adsorption sites. (b) H₂ (gray white balls) dissociation over the Fe-doped Mg(0001) surface when Fe (light blue ball) is in the subsurface (capped by a kicked-out Mg atom) as viewed from the side position. (a,b) Reproduced with permission [204]. Copyright 2014, Elsevier. (c) H₂ (dark red) dissociation over the Ag-doped Mg surface as viewed from the side position at IS, TS, and FS. The Mg, Ag, and H atoms are represented, respectively, by light grey, dark grey, and black colors. The TM is exposed to the surface, not capped by a kicked-out Mg atom. Reproduced with permission [211]. Copyright 2008, Elsevier.

Chen et al. [187] used a DFT calculation to compare the effect of atomic Fe in forms of adsorption and substitution (not capped by the kicked-out Mg atom) on the hydriding reaction of Mg(0001) surface; their findings follow.

1. The H–H bond lengths for the H₂ molecule on the atomic-Fe-substituted and the atomic-Fe-adsorbed Mg(0001) were 0.763 and 0.767 Å, respectively, which are both higher than that of a typical H₂ molecule (0.754 Å), and the H₂ molecule was more strongly attracted on the atomic-Fe-adsorbed Mg(0001) than on the atomic-Fe-substituted Mg(0001), as shown in Figure 24a,b.
2. The adsorbed Fe had a better catalytic performance for H₂ dissociation. The activation energy barriers for H₂ dissociation on the atomic-Fe-substituted and the atomic-Fe-adsorbed Mg(0001) were 1.76 and 0.37 eV (170 and 36 kJ mol^{−1} H₂), respectively. The H–H bond lengths at the TS were calculated to be 1.651 Å and 2.438 Å on the atomic-Fe-substituted and the atomic-Fe-adsorbed Mg(0001), respectively. This suggests that the stronger the attraction of H₂ by the surface, the smaller the activation energy of H₂ dissociation and the longer the H–H bond length in the TS.
3. During H₂ dissociation, the H–H bond length in the TS could be affected by the bridging effect of Fe *d* orbitals, Fe–H ionic interaction, and Mg–H interaction (ionic + covalent) between H₂ and Mg atoms adjacent to the Fe atom. In the case of atomic-Fe-adsorbed Mg(0001), a partial density of states (PDOS) calculation showed that during H₂ dissociation, compared with the overlapping of H *s* orbital with the Fe *s* and Fe *p* orbitals (which contribute 18.4% of the total electrons participating in the dissociation process), the Fe *d* orbitals contributed 81.6% of the total electrons participating in the dissociation process, overlapping with the H *s* orbital at higher energy levels of −2.79 and 0.35 eV, suggesting that the Fe *d* orbital plays a dominant role in the

Fe–H interaction during H_2 dissociation. Moreover, a Mulliken charge calculation (also known as Mulliken population analysis), which estimates the ionic interaction as a component of the interatomic interaction by the net charge difference between two atoms [182], showed that the charge values of H atoms were -0.134 and -0.155 , while those of Mg atoms adjacent to Fe atom were 0.086 , 0.071 , and 0.045 , implying a Mg–H ionic interaction. However, the Mulliken charge of Fe atom is only 0.003 . The electrically neutral performance of the adsorbed Fe during H_2 dissociation was ascribed by the authors [187] to the moderate $\chi(Fe)$ (1.83 , Pauling scale) as compared with $\chi(Mg)$ (1.31 , Pauling scale) and $\chi(H)$ (2.20 , Pauling scale) and the fact that electrons can be transferred from Mg atoms to H atoms through the Fe atom “bridge” as a result of the “ χ rule”. Unlike that of the adsorbed Fe, the substituted Fe exerted no obvious influence on H_2 dissociation (no obvious overlapping effect between the H s orbital and the Fe s , Fe p , Fe d orbitals), while there were overlaps between the H s orbital and the Mg s and Mg p orbitals during H_2 dissociation due to the steric hindrance effect, which was related to the radius of the Fe atom being smaller than that of the Mg atom. On the one hand, this hindrance effect inhibited the attraction of Fe electrons by the H atom, destroying the “ χ rule” and thereby leading to more electrons transferred from Mg to Fe than electrons transferred from Fe to H atom. Consequently, the Mulliken charge value of Fe became -0.138 , which suggests that the Fe–H interaction was screened. On the other hand, this hindrance effect led to a larger contact surface between the H atom and Mg atom, and as a result, more electrons were transferred from Mg to H, which explains the large Mulliken charges of Mg and H in the atomic-Fe-substituted Mg(0001) compared to those of the atomic-Fe-adsorbed Mg(0001), as shown in Figure 24c,d;

4. Compared with the adsorbed Fe, the substituted Fe was more favorable for the surface penetration of H atom from the fcc site (A site) to the octahedral interstice (B site) but is unfavorable for the bulk diffusion from the tetrahedral interstice (C site) to the octahedral interstice (D site) (Figure 24e,f) due to the difference in the orbital overlapping between H s and Fe s orbitals.

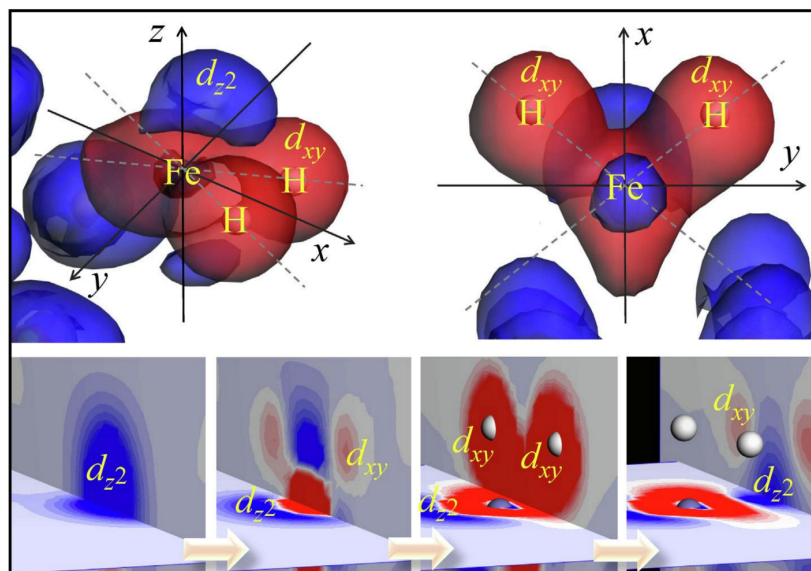


Figure 22. Deformation charge density distributions for the TS of H_2 dissociation on atomic-Fe-adsorbed Mg(0001). The red and blue indicate electron enrichment and depletion regions, respectively. Here, d_{z2} is the filled d orbital, which contributes the electrons during dissociation; d_{xy} is the unfilled d orbital, which accepts the electrons during dissociation. Reproduced with permission [187]. Copyright 2019, Elsevier.

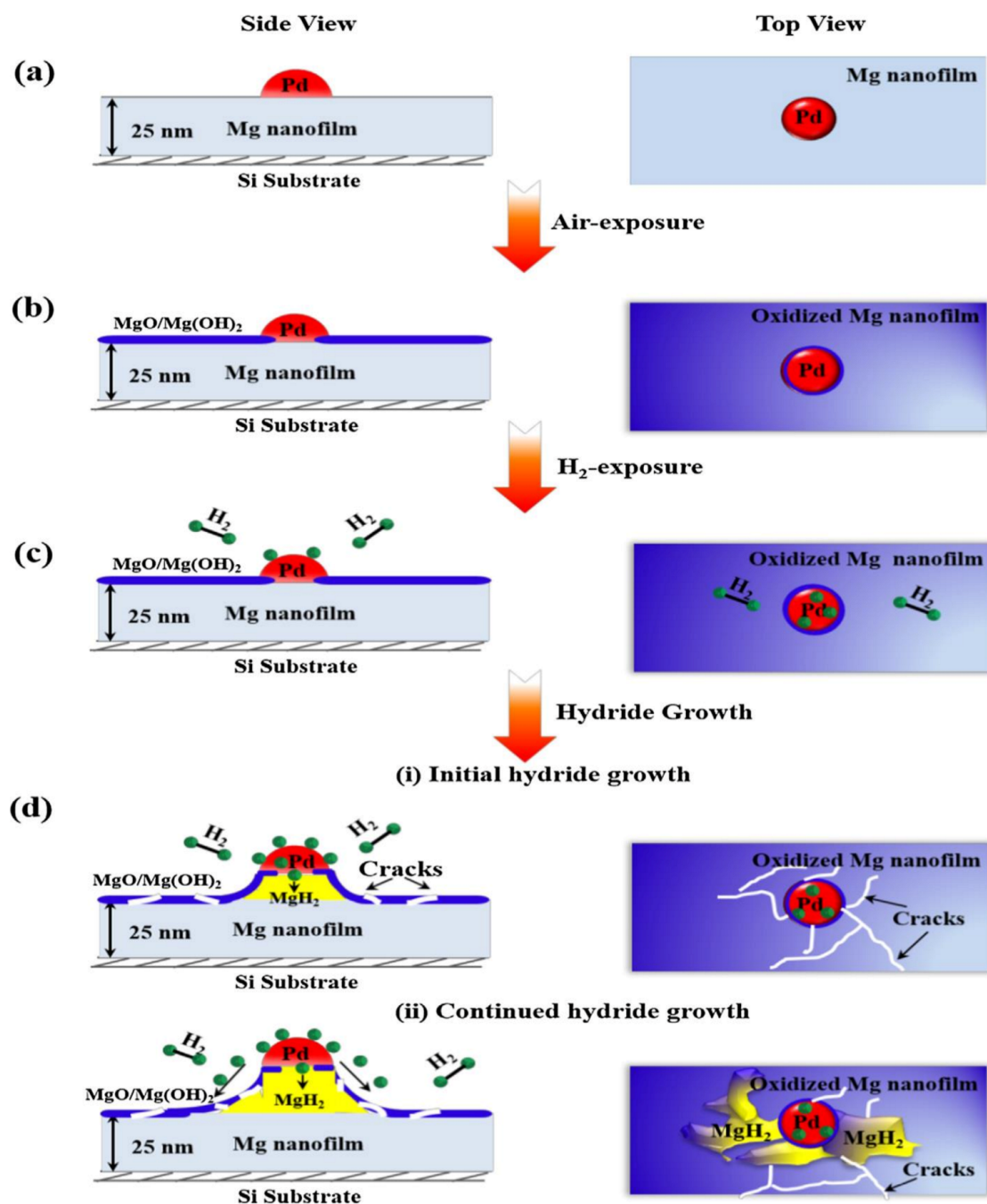


Figure 23. Schematic representation of the steps involved in the formation of localized MgH₂ nanodomains from the hydrogenation of Mg nanofilms catalyzed by Pd NPs. (a) Deposition of size-selected Pd NPs on a pristine Mg nanofilm. (b) Samples deliberately air-exposed before hydrogenation, leading to the formation of a very thin protective MgO/Mg(OH)₂ layer on the surface of the film. (c) Exposure of the sample to hydrogen, leading to dissociation of the hydrogen molecule to atoms on the Pd NP surface. (d) (i) Atomic hydrogen diffuses through the Pd NPs and reacts with the Mg nanofilm, forming MgH₂ and surface protrusions under the Pd NPs; (ii) these localized protrusions rupture the surrounding MgO/Mg(OH)₂ layer, permitting hydrogen atoms to spill over the Pd NPs and tunnel through the cracks to react with the underlying fresh Mg nanofilm. (a–d) Reproduced with permission [53]. Copyright 2016, Elsevier.

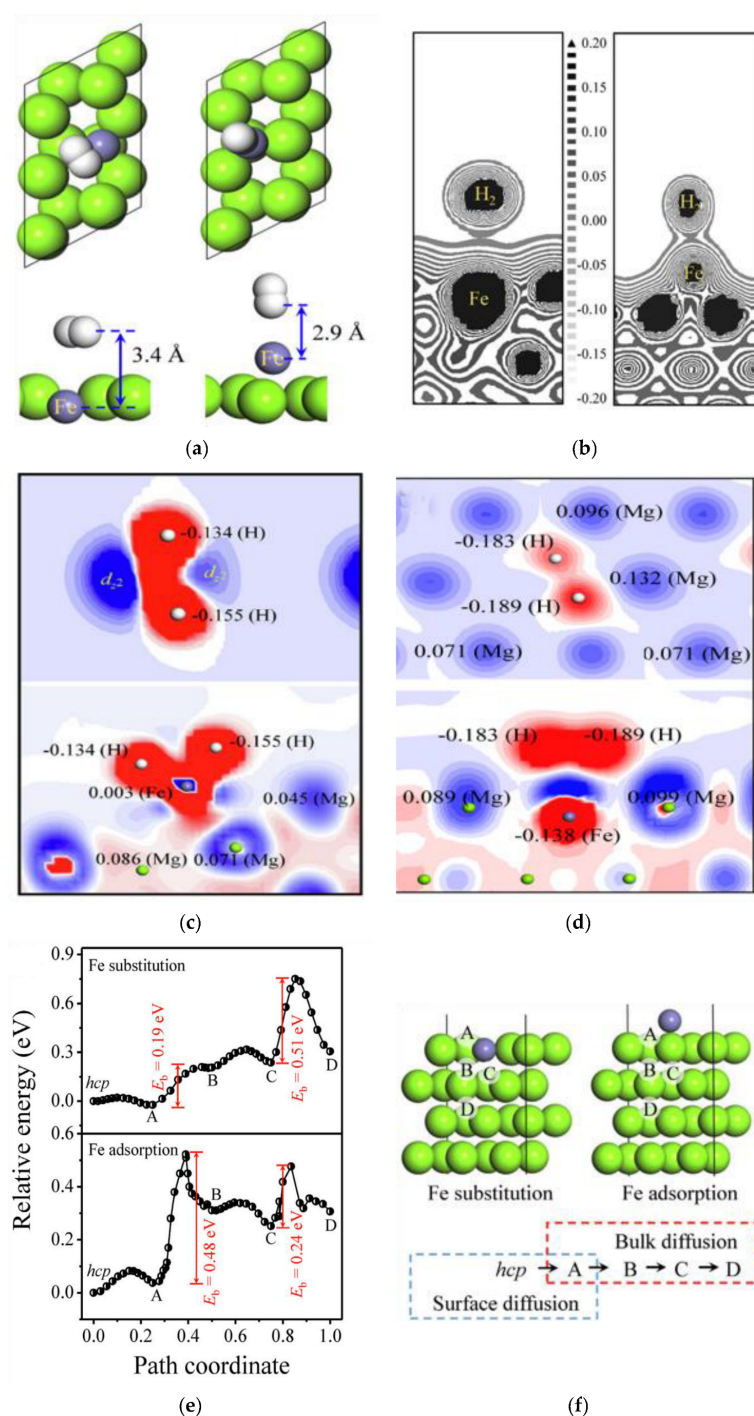


Figure 24. (a) Schematic images of H₂ molecule adsorption on the atomic-Fe-substituted (left) and the atomic-Fe-adsorbed (right) Mg(0001). The green, brown, and white balls represent Mg, Fe, and H atoms, respectively. (b) Charge density distributions for the atomic-Fe-substituted (left) and the atomic-Fe-adsorbed (right) Mg(0001) after H₂ adsorption. (c) Deformation charge density distributions and Mulliken charges for the TS of H₂ dissociation on the atomic-Fe-adsorbed Mg(0001). (d) Deformation charge density distributions and Mulliken charges for the TS of H₂ dissociation on the Fe-substituted Mg(0001). (e) Minimum energy paths (MEPs) for the H atom diffusion on the atomic-Fe-substituted and atomic-Fe-adsorbed Mg(0001). (f) Diffusion routes of the H atom on the atomic-Fe-substituted and atomic-Fe-adsorbed Mg(0001). (a–f) Reproduced with permission [187]. Copyright 2019, Elsevier.

In addition to considering the orbital overlapping between H *s* and Fe *s* orbitals, the difference in Figure 24e may be explained through another mechanism: (1) In the case of Fe substitution, the A site is located above the Fe atom; thus, the hydrogen diffusion energy barrier from the A site to the B site is small, benefiting from the downward component force of the Fe atom on the H atom located at the A site. Meanwhile, the C site is located directly below the Fe atom, so hydrogen diffusion from the C site to the D site is difficult. (2) In the case of Fe adsorption, the A site is located below the Fe atom, so hydrogen diffusion from the A site to the B site is difficult. Although the C site is located directly below the surface Mg atom, the attraction of the H atom located at the C site by the surface Mg atom can be expected to be weaker than that of the H atom located by the substituted Fe atom, since the adsorbed Fe atom may pull the electronic cloud of the surface Mg atom to itself to weaken the Mg–H interaction just like the Ti atom does to the adjacent H atoms, as shown in Figure 11. Thus, hydrogen diffusion from the C site to the D site in the case of Fe adsorption proceeds more easily than in the case of Fe substitution. This reveals the competitive phenomenon between surface dissociation of H₂ and surface diffusion of H atoms depending on the doping sites of TM on the surface of Mg.

The TM-dependent competition between the surface dissociation of H₂ and the surface diffusion of H atoms has been reported by Pozzo et al. [211], who studied (Figure 25a) hydrogen molecule dissociation and subsequent atomic hydrogen diffusion on TM (Ti, V, Zr, Fe, Ru, Co, Rh, Ni, Pd, Cu, Ag)-doped Mg(0001) surfaces by replacing one of the four surface Mg atoms with one TM atom (not capped by the kicked-out Mg atom). They found that TMs on the left of the periodic table strongly bind hydrogen, eliminating the barrier of hydrogen molecule dissociation on the surface but leading to the hard diffusion of atomic hydrogen. On the contrary, TMs on the right of the periodic table did not bind hydrogen, leading to the easy diffusion of atomic hydrogen but a high barrier to hydrogen molecule dissociation. Mg surfaces doped by Fe, Ni, and Rh had both reduced dissociation barriers and low diffusion barriers. Similar results (Figure 25b) were reported by Wang et al. [204]. The authors [204,211], without considering the hindrance effect of adjacent Mg atoms as mentioned in Chen et al. [187], attributed these results to the *d* band center positions of TM dopants, which control the binding ability of hydrogen to TMs and thereby the processes of hydrogen molecule dissociation and diffusion of atomic hydrogen with the following equation:

$$E_d = \int_{-\infty}^{E_0} dE (E - E_F) p_d(E) \quad (9)$$

where $p_d(E)$ represents the projection of the electronic density of states onto *d* type spherical harmonics, E_F represents the Fermi energy, and E_0 represents the cutoff energy, which usually sits at 7 eV above E_F . Based on the ‘*d* band center’ mechanism, Figure 25a fits on an ‘inverse volcano plot’ around E_F , which is in good agreement with the DFT calculation results of the TM–H chemical bond energy as a function of the *d* band center in the expanded MgTM alloy, as shown in Figure 25c, in which two regimes are present. One of these regimes is linear and displays increasing bond strength, going from low- to half-filling of the *d* band. The other regime displays decreasing bond strength as a consequence of the repulsive contribution originating from the coupling of the H (1*s*)–TM (*d*) anti-bonding state, which remains unoccupied until MgMnH₃ (Figure 25d) [212]. Another common characteristic of Figure 25a,c is that for the ETMs, the Fermi level lies in the strongly bonding levels near the bottom of the *d* band, while for the late transition metals (LTMs) the Fermi level is in the top of or above the *d* band.

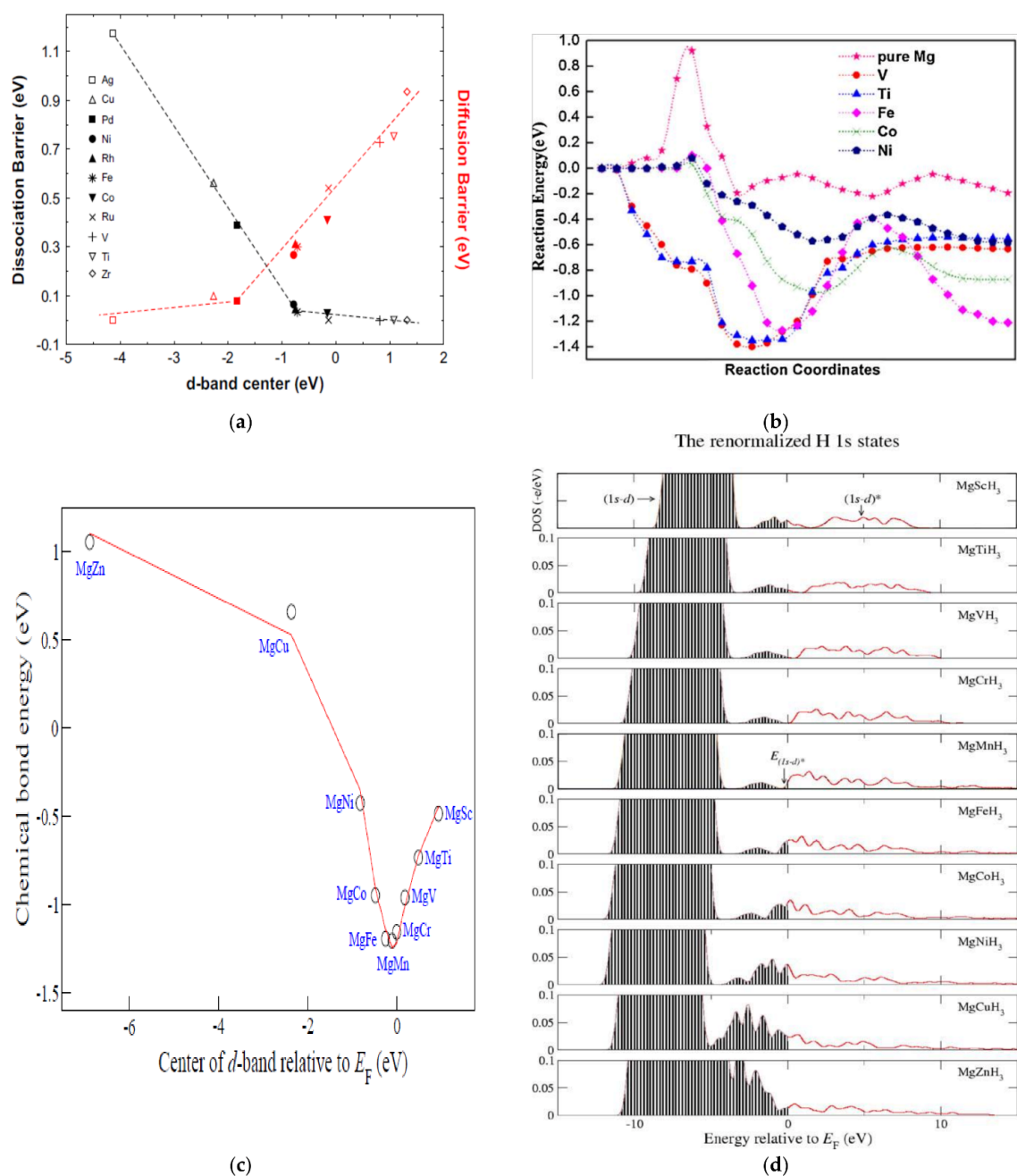


Figure 25. (a) Activation energy barrier for hydrogen dissociation (black) and diffusion (red) of hydrogen on pure Mg and TM-doped Mg(0001) surfaces (TM is not capped by the kicked-out Mg atom) as a function of the d band center positions. Reproduced with permission [211]. Copyright 2008, Elsevier. (b) Minimum energy paths for the dissociation of the H_2 molecule and subsequent diffusion of one of the two H atoms on a pure Mg(0001) surface and on a (Ti, V, Fe, Co, and Ni)-doped Mg(0001) surface when TMs in the first layer are not capped by the kicked-out Mg atom. Reproduced with permission [204]. Copyright 2014, Elsevier. (c) Chemical bond energy of hydrogen atoms in the expanded Mg–TM alloy as a function of the d band center, where magnetic effects have been excluded. (d) The local density of states projected onto the renormalized hydrogen 1s states as a function of the energy relative to the Fermi level, where gray states are occupied. Two effects are present: an attractive down-shift in the occupied bonding $(1s-d)$ state and a repulsive contribution scaling with the gradual filling of the anti-bonding $(1s-d)^*$ state from MgMnH₃ to MgZnH₃. $E_{(1s-d)^*}$ is the onset of occupancy of the anti-bonding state. (c,d) Reproduced with permission [212]. Copyright 2004, Elsevier.

Compared with Figure 25c, Figure 25a shows the following differences:

1. In the same period as the filling of d band, the d band center moves towards low energy as in Figure 25c, except for Fe→Co. In Pozzo et al. [211], Fe is considered to be the only required dopant for magnetic calculations (while Co is also magnetic, when used as a dopant of the Mg surface, Pozzo et al. [211] show that it can be treated as non-magnetic). Moreover, as mentioned in Section 3.1, spin-polarized calculations reveal the splitting of the d band, which may cause the shifting of the d band center.
2. For TMs in the same group, there is a deviation between the locations of the $4d$ band center and the $3d$ band center, especially for TMs with a nearly filled d band (e.g., Ni→Pd, Cu→Ag). This is most likely related to differences in the radii of TMs.
3. The top of the volcano is not located at the Fermi level, and on the right side of the top of the volcano, the dissociation activation energy of hydrogen does not decrease as the d band center moves toward the top of the volcano. This may be due to the difference in doping sites (surface doping in Figure 25a and volume doping in Figure 25c) or doping amount in the two cases.

It should also be noted that the hindrance effect reported for the atomic-Fe-substituted Mg(0001) (not capped by the kicked-out Mg atom) in the work of Chen et al. [187] is not observed in Figure 25a due to the good correlation of the barrier values with the d band center position, implying that the effects of the d orbital electrons are not screened by surface Mg atoms. Despite this debate surrounding the hindrance effect in the atomic-TM-substituted Mg(0001) with a TM that is not capped by the kicked-out Mg atom, one can believe that the hindrance effect exists when the TM is in the subsurface of Mg(0001). For example, in the work of Wang et al. [204], effects of some of the d orbital electrons of the TM atom substituted in the subsurface were reported to be screened by surface Mg atoms due to the low correlation of the barrier values with d band center position (Table 7). We believe that this hindrance effect leads to the transformation of partial direct TM–H interaction to indirect TM–H interaction, which occurs through the surface Mg atom as an intermediary, such as via (1) another Kubas interaction, wherein the polarization of H_2 molecules by the electric field produced by a positively charged metal ion facilitates H_2 dissociation [16,17,213], the electronegativity difference of $\chi(TM) - \chi(Mg)$ leads to the transfer of the electrons from the surface Mg to the subsurface TM, and as a result, the surface Mg creates a positive electric field, which facilitates the hydrogen dissociation due to the polarization of H_2 molecules; or (2) TM–Mg orbital hybridization (Figure 26), which may pull the electronic cloud of the surface Mg atom to TM to weaken the interaction between H_2 and the surface Mg, leading to a more difficult H_2 dissociation.

Table 7. The d band center position with respect to the Fermi energy (E_d), the activation energy barrier for the dissociation of H_2 (E_{diss}), and the activation energy barrier for the diffusion of atomic H (E_{diff}) when the TM atom is placed in the subsurface of Mg(0001) (TM is capped by the kicked-out Mg atom) [204].

Surface	E_d [eV]	E_{diss} [eV]	E_{diff} [eV]
Pure Mg	-	0.92	0.19
Zn-doped Mg	−1.04	0.63	0.18
Ni-doped Mg	−0.89	0.65	0.16
Fe-doped Mg	−0.73	0.59	0.12
Co-doped Mg	−0.52	0.61	0.14
Mn-doped Mg	−0.14	0.60	0.10
V-doped Mg	0.06	0.77	0.10
Ti-doped Mg	0.16	0.71	0.08
Sc-doped Mg	0.43	0.82	0.04

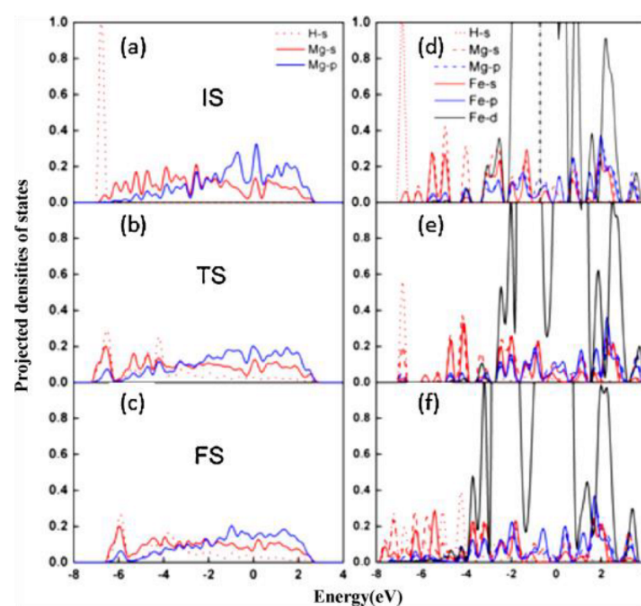


Figure 26. Projected densities of states for H_2 dissociating over a pure Mg(0001) surface as a function of the energy relative to the Fermi level for the (a) IS, (b) TS, and (c) FS. The same is shown for the Fe-doped Mg(0001) surface (Fe is placed in the subsurface) for the (d) IS, (e) TS, and (f) FS. The dashed vertical line shows the position of the d band center in (d). (a–f) Reproduced with permission [204]. Copyright 2014, Elsevier.

In order to facilitate the analysis of the influence of $\chi(TM)$, $r(TM)$, and d band center on E_{diss} , in Figure 27, we demonstrate $\chi(TM)$, d band center, and the E_{diss} data from Table 7 (for $r(TM)$, one can refer to Figure 19). As shown in Figure 27, the change trend of E_{diss} is consistent with that of $\chi(TM)$ except for Sc. However, it is not the case that, except for Sc, E_{diss} increases/decreases with the increase/decrease of $\chi(TM)$ in Figure 27, because for $Zn \rightarrow Co$, $r(Zn) = r(Co)$, and E_{diss} decreases with the increase of the $\chi(TM)$, while for $Ni \rightarrow Co$, $r(Ni) = r(Co)$, and E_{diss} decreases with the decrease of the $\chi(TM)$. The same phenomenon can also be observed for the dependence of E_{diss} on the d band center. For example, for $Ni \rightarrow Co$ and $Zn \rightarrow V$, $r(Ni) = r(Co) = r(Zn) = r(V)$, the decreases in $\chi(TM)$ are 0.03 and 0.02 respectively, which are approximately equal, and the increase of the d band center leads to the decrease of E_{diss} for $Ni \rightarrow Co$ but the increase of E_{diss} for $Zn \rightarrow V$. Thus, other factors that might influence the H_2 dissociation and thereby the diffusion of atomic H when a TM atom is placed in the subsurface of Mg(0001) should also be considered.

For example, based on Figure 25c, one can propose that in different d band center areas, the effect of the increase of d band center on E_{diss} may be different; that is, in some d band center areas, the TM–Mg orbital hybridization plays the dominant role, while in other d band center areas, the TM– H_2 orbital hybridization plays the dominant role. In fact, even if the TM–Mg(TM– H_2) orbital hybridization plays the dominant role in some d band center areas, the effect of the increase of the d band center on E_{diss} may be different in different d band center areas. Furthermore, as suggested by Wang et al. [204], magnetic (spin-polarized) calculations must be used for Mg(0001) surfaces doped by Fe and Co, which may influence the calculated d band center position and E_{diss} and thereby the change trend of E_{diss} with the d band center in Table 7 (Ni is also a magnetic element, but when it was located at the Mg surface, the system was found to be non-magnetic). Table 7 is also noteworthy in that E_{diff} does not strictly decrease with the increase of E_{diss} . In addition to being explained by the above-mentioned factors that influence H_2 dissociation, this phenomenon can also be explained by TM s –H s orbital overlapping. Chen et al. [187] believed that, compared with Fe s or Fe p orbitals, the Fe d orbitals can play the dominant role in overlapping with the H s orbital for H_2 dissociation, but they ascribed the beneficial effect of Fe on the H diffusion to the orbital overlapping between H s and Fe s orbitals.

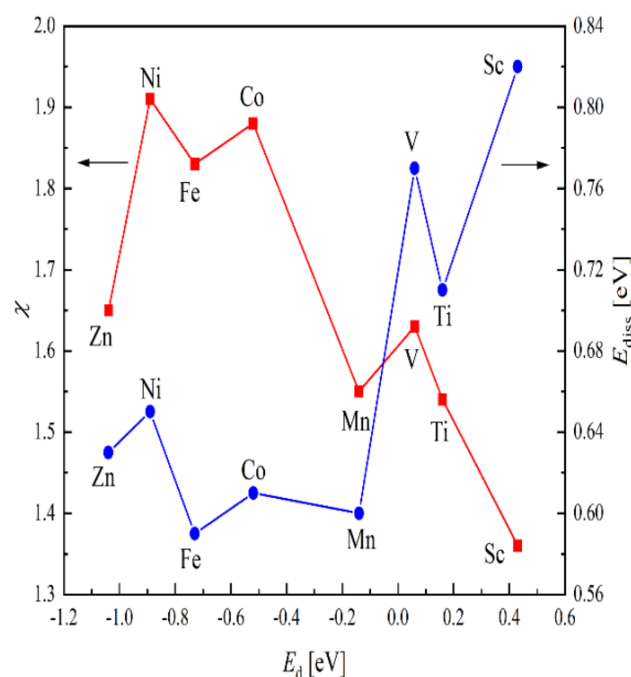


Figure 27. Electronegativity (Pauling scale) of TM and E_{diss} depending on the d band center of TM-doped Mg. E_{diss} and d band center come from Table 7, the electronegativity (Pauling scale) of TM come from reference [202,203].

5. “Hydrogen Pump”

5.1. Mg–TM Intermetallic Compound or Mg–TM–H Ternary Hydrides as “Hydrogen Pump”

The Mg–Ni system in Figure 15 is different from other Mg–TM systems; this was attributed by the authors [102] to the formation of Mg_2NiH_4 , which reveals another mechanism for TMs to improve the hydrogen sorption properties of Mg (MgH_2): a “hydrogen pump” that significantly facilitates hydrogen diffusion. The “hydrogen pump” initializes during dehydrogenation and requires the release of hydrogen from the “hydrogen pump” prior to MgH_2 [214]; thus, a typical “hydrogen pump” is in the intermediate hydride phase with higher hydrogenation enthalpy than MgH_2 , such as Mg_2NiH_4 , which has an enthalpy of formation of $-64 \text{ kJ mol}^{-1} \text{ H}_2$ [34,102,214–225], and Mg_3CoH_5 , which has a hydride formation enthalpy of $-70 \text{ kJ mol}^{-1} \text{ H}_2$ [117]. The pump works via an expansion–strain–de/absorption mechanism [205], since the de/hydrogenation process can be initiated via volume expansion and microstrain caused by the reversible conversion of $Mg_mTM_n/Mg_mTM_nH_x$, which can influence the neighboring Mg core [226,227]. For example, in the process of H_2 absorption in the Mg– Mg_2Ni system (Figure 28), after dissociation of H_2 molecules, the homogeneously distributed Mg_2Ni particles capture and absorb H atoms to form Mg_2Ni hydrides, leading to microstructural changes such as volume expansion and micro strain, which affects the attached Mg neighbor and hence triggers its hydrogen absorption [205]. Volume expansion from Mg_2Ni to Mg_2NiH_4 leads to the volume expansion of the attached Mg lattice, which causes new defects in the attached Mg lattice. These new defects allow for a dispelling of the accumulated elastic strain caused by the approximately 20% lattice expansion from the initial Mg metal to the rutile-type tetragonal phase of MgH_2 , making the nucleation and growth of MgH_2 fast and easy. Once the absorption of Mg is initiated, further hydrogen absorption proceeds through the same mechanism inside the Mg matrix [205], since from Mg to MgH_2 , the volume expansion occurs as mentioned above. Note that only marginal Mg_2NiH_4 is required in the composite to cause a sufficient synergetic effect for hydrogen absorption [205]. When the surface of Mg particles is covered by a large amount of MgH_2 , the hydrogenation of Mg will stop. Thus, the optimal “hydrogen pump” effect can be expected only when the amount of

Mg_2Ni distributed on the surface of the Mg particle is small. The dehydrogenation process is the opposite, and thus, the dehydrogenation of MgH_2 starts as a result of a clamping effect related to the volume compression that results from the transition of Mg_2NiH_4 to Mg_2Ni . The clamping effect will be discussed in Section 6.

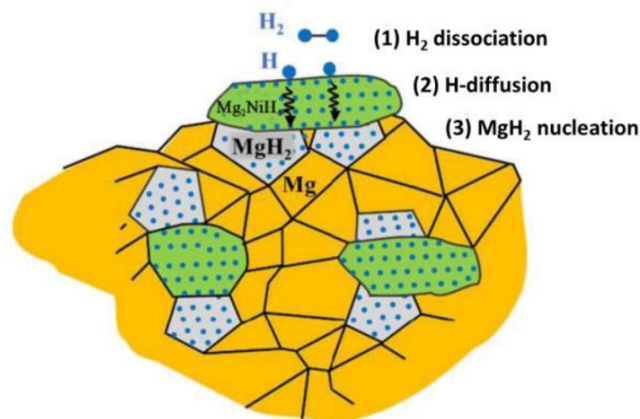


Figure 28. Schematic representation of a Mg– Mg_2Ni system showing the role of Mg_2NiH_4 to enhance hydrogen absorption kinetics in Mg. The H_2 molecules, Mg_2NiH_4 , Mg, and MgH_2 are represented, respectively, by blue, green, orange, and grey colors. Reproduced with permission [37]. Copyright 2019, Royal Society of Chemistry.

Theoretical studies have demonstrated that the Mg–ETM–H system of the Ca_7Ge structure (Figure 29) type (space group: $Fm\bar{3}m$), such as $\text{Mg}_7\text{TMH}_{16}$ (TM = Sc, Ti, V, Zn, Y, Zr, Nb, Pd, Cd), $\text{Mg}_6\text{NbH}_{16}$, $\text{Mg}_6\text{TiH}_{16}$, and $\text{Mg}_6\text{VH}_{16}$, are less stable than MgH_2 and have better hydrogen-releasing properties compared to MgH_2 [147–149,228]. This implies that a H-stabilized ternary hydride could serve as a “hydrogen pump”. For H-stabilized ternary hydrides, the “hydrogen pump” mechanism is informed by Lin et al. [229] and Lu et al. [207]. The DFT calculation conducted by Lin et al. [229] on the catalytic effect of $\text{CeH}_x/\text{CeO}_2$ ($x = 2, 2.25, 2.5, 2.75$ and 3) on the hydrogen storage properties of MgH_2 suggests that the “hydrogen pump” effect arises from the lowest formation energies (in absolute value) of V_{H} (hydrogen vacancy) at the $\text{CeH}_{2.75}$ – CeO_2 interface. Lu et al. [207] calculated the defect formation energy of H atoms depending on the hydrogen pressure at the tetrahedral (Figure 30a) and octahedral (Figure 30b) site of a H-stabilized Mg_3Pt lattice, which was formed during the hydrogenation process of the core–shell–nanostructured Mg@Pt composite. The calculation results (Figure 30c) showed a tendency towards a lower defect formation energy (in absolute value) from the H atom with decreasing hydrogen partial pressure. Based on these results, the authors [207] described the catalytic mechanism of Mg_3Pt as a “hydrogen pump” during the hydrogen desorption process: escape of the H atoms in Mg_3Pt from the interstitial tetrahedral and octahedral sites at low hydrogen pressure is followed by H atoms/ions in MgH_2 passing through the MgH_2 – Mg_3Pt interface and entering Mg_3Pt to stabilize it, which continuously proceeds until MgH_2 is completely dehydrogenated. A similar “hydrogen pump” mechanism can also be observed for Mg–Fe–H hydrides. Normally, Mg and Fe are immiscible, but the ternary hydride Mg_2FeH_6 with a formation enthalpy of $-77.9 \text{ kJ mol}^{-1} \text{ H}_2$ can be formed in the presence of hydrogen [34]. During the dehydrogenation process, while Mg_2FeH_6 has a lower formation enthalpy than does MgH_2 , the d electrons orbital from Fe causes hydrogen to first be released from Mg_2FeH_6 , which transforms into Mg and Fe, since Mg and Fe cannot form any intermetallics. After complete dehydrogenation of Mg_2FeH_6 , MgH_2 starts to release hydrogen, which can diffuse into the Fe nanoparticles to form Mg_2FeH_6 again [111,128].

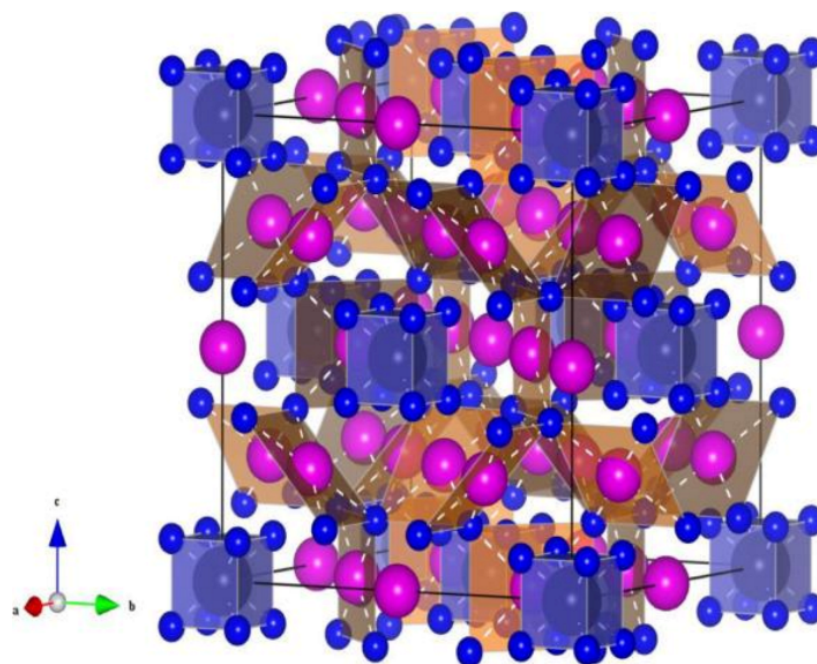


Figure 29. The high-pressure phase of $\text{Mg}_7\text{TiH}_{16}$ crystal structure within an FCC structure analogous to the Ca_7Ge type with a unit cell of 96 atoms. Pink (medium), black (big), blue (small) spheres represent Mg, Ti, and H atoms, respectively. Reproduced with permission [228]. Copyright 2013, Elsevier.

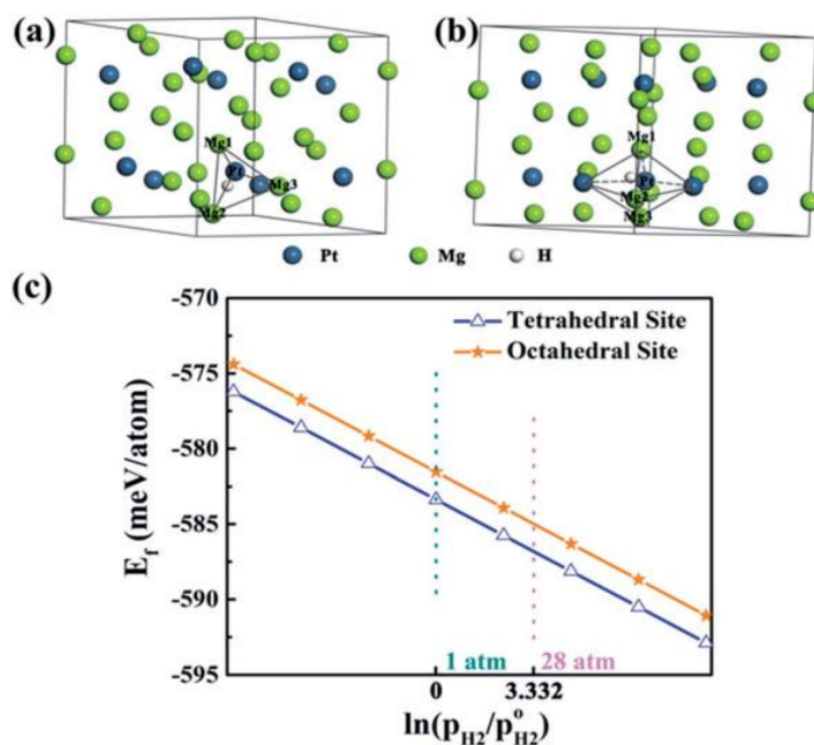


Figure 30. DFT calculation results for the Mg@Pt composite. (a) Interstitial hydrogen atom in the tetrahedral sites of Mg_3Pt . (b) Interstitial hydrogen atom in the octahedral sites of Mg_3Pt . (c) Defect formation energy of H-atom dependence on hydrogen pressure at the tetrahedral and octahedral sites. (a–c) Reproduced with permission [207]. Copyright 2019, Royal Society of Chemistry.

5.2. ETM or ETM Dihydride as “Hydrogen Pump”

A large number of studies have demonstrated that the surfaces of metallic Ti and V are very favorable for the dissociation and recombination of H_2 molecules by a spill-over effect and/or a hydrogen pump effect [230–234]. In one study, the vanadium was believed to work as a “hydrogen pump” by chemisorbing hydrogen atoms and transferring them to the Mg–V interface, which provides active nucleation sites for magnesium hydride [235]. In this case, the “hydrogen pump” mechanism of ETM for the hydrogenation of Mg can be also considered to be of an expansion–strain–de/absorption type. In the case of niobium-based additives, the improvement of hydrogen storage properties of the MgH_2 system after HEBM (high-energy ball milling) experiments has been explained by the formation of intermediate phases (NbH_x) that could act as a gateway for the hydrogen, favoring the desorption kinetics of MgH_2 , because the nano-interfaces between the phases of NbH_x – MgH_2 possess high diffusivity pathways for the hydrogen [236,237]. Based on the fact that the Nb–H bond is weaker than the Mg–H bond [200], it has been proposed that MgH_2 begins to dehydrogenate after the complete dehydrogenation of NbH. Here, the interfaces at the Nb– MgH_2 boundaries with high interfacial energy can act as fast hydrogen diffusion paths to accelerate the dehydrogenation process of MgH_2 ; that is, the released hydrogen from MgH_2 diffuses into the Nb through the interface of MgH_2 –Nb to form NbH, and then, NbH releases hydrogen again and transforms into Nb. Finally, via Nb/NbH hydrogenation/dehydrogenation cycling, MgH_2 completely changes into Mg [200].

While TiH_2 , with a formation enthalpy of $\Delta H \approx -130 \text{ kJ mol}^{-1} H_2$ [238], has even less favorable thermodynamics compared to MgH_2 , during the dehydrogenation process, TiH_2 releases hydrogen prior to MgH_2 and provides the hydrogen diffusion paths to accelerate the hydrogen desorption process of MgH_2 [239]. Indeed, for the $Na_2Ti_3O_7$ -nanotube-catalyzed MgH_2 , the TiH_2 that is formed during the hydrogen cycles is believed to serve as a “hydrogen pump” to promote the de/hydrogenation rate [43]. This may be due to the rapid diffusion of atomic hydrogen in TiH_2 [238,240]. In fact, hydrogen atoms can diffuse extremely fast in $ETMH_x$ (ETM = Y, Ti, Zr, V, and Nb) hydrides, having a diffusion coefficient that is five orders of magnitude higher than that of MgH_2 [37]. Moreover, the TM (TM = Sc, Ti, V, and Cr) dihydrides are reported to be metallic (Figure 31) [25], which may lead to the fast H_2 desorption kinetics due to the abundant gas of free electrons. Recently, Rizo-Acosta et al. [37] found that compared with other MgH_2 – $ETMH_x$ (ETM = Sc, Ti, Zr, V, and Nb) nanocomposites, the hydrogen desorption kinetics of the MgH_2 – YH_3 nanocomposite is almost as sluggish as those of RBM (reactive ball-milling)-made MgH_2 . The slow kinetics were attributed by the authors [37] to the fact that YH_3 hydride, being a semiconductor with no available electronic states at the Fermi level, has poor catalytic activity towards the recombination of hydrogen atoms into molecules at the YH_3 surface or YH_3 – MgH_2 interfaces, which led to a high content of retained MgH_2 in desorption sweeps (Figure 32). Unlike YH_3 , metallic hydrides from other ETMs (ScH_2 , TiH_2 , ZrH_2 , VH , and NbH) are characterized by partially occupied d bands near the Fermi level [37,241,242] that facilitate H_2 -surface reactions [37]. The irreversible hydrogen content stored in the form of thermodynamically stable $ETMH_x$, displayed in grey at the bottom of Figure 32, can be explained by the exothermic reaction between hydrogen and TMs in groups below group VI, which leads to higher hydrogen solubility and therefore more stable metallic hydrides, and the endothermic reaction between hydrogen and the group VI–VIII transition and noble metals, which leads to lower hydrogen solubility [182].

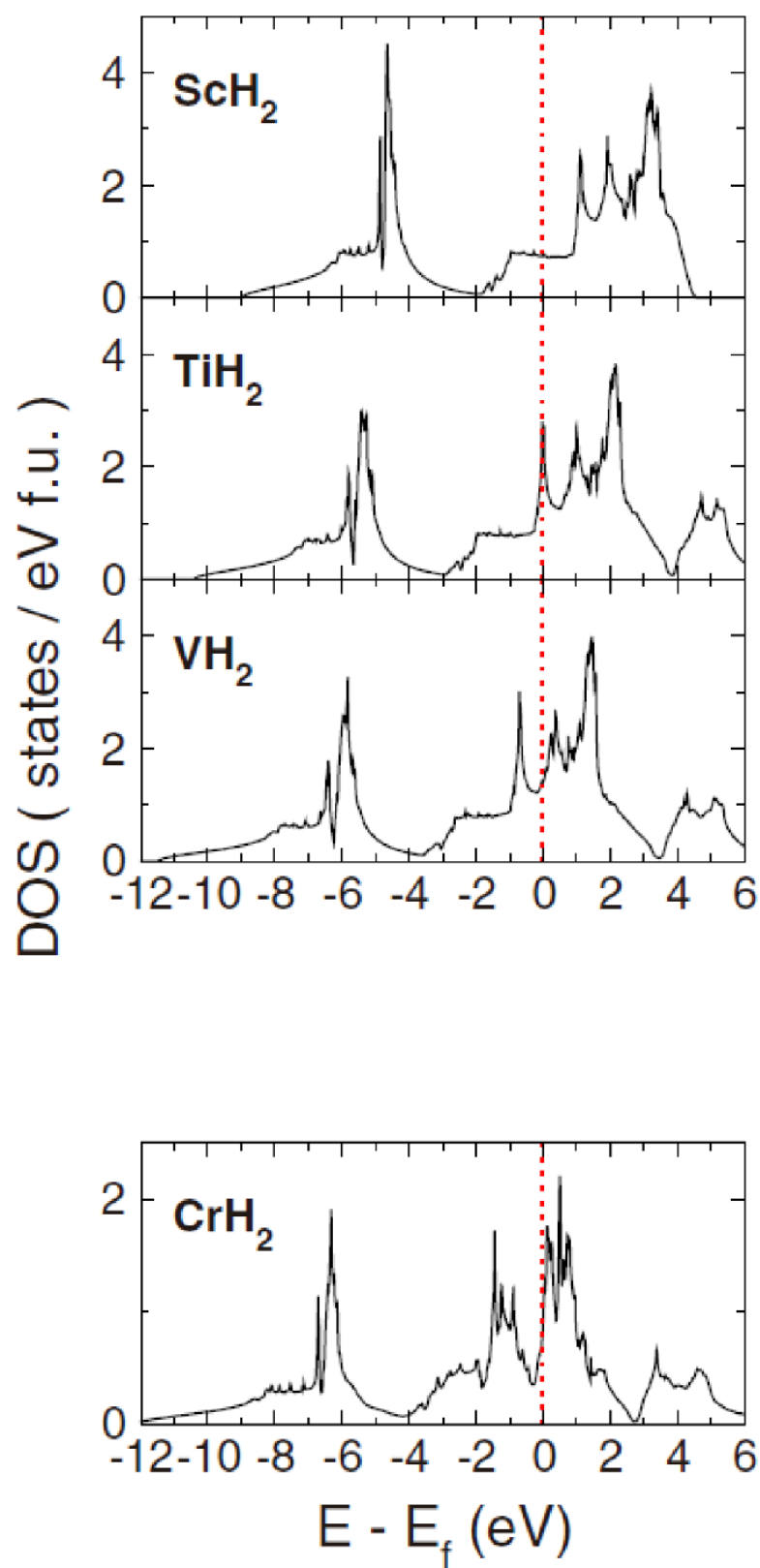


Figure 31. DOS of TMH₂ for TM = Sc, Ti, V, and Cr. For CrH₂, the nonmagnetic DOS is given. Reproduced with permission [25]. Copyright 2009, American Physical Society.

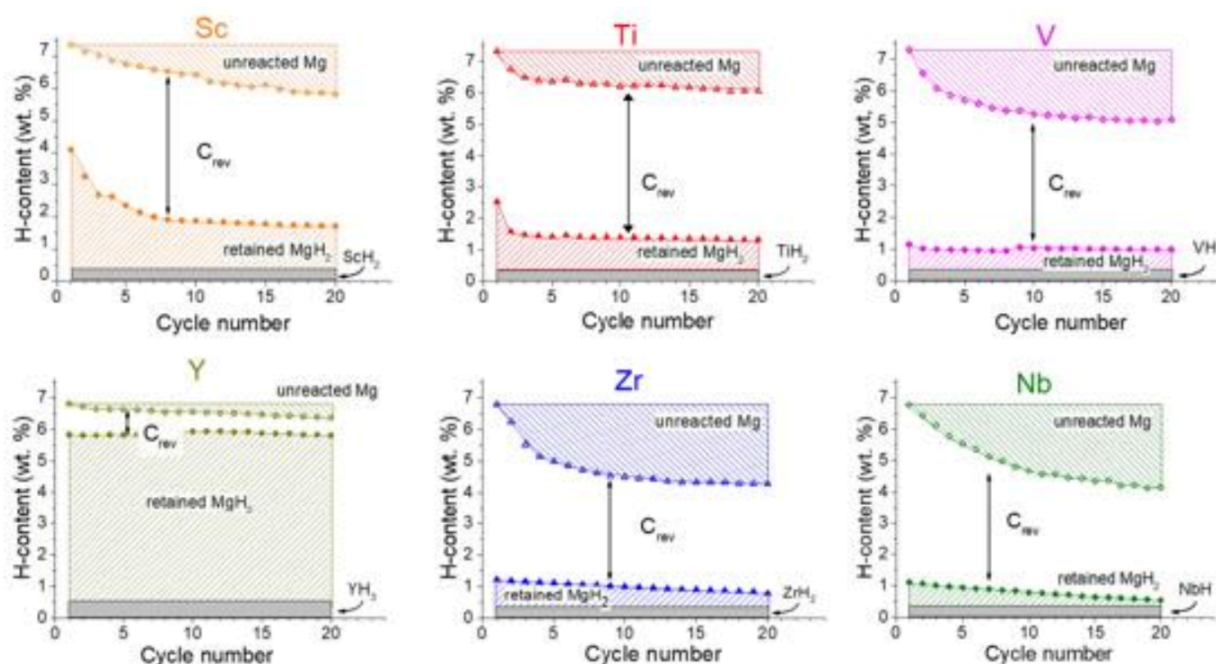


Figure 32. H content in $\text{MgH}_2\text{-ETMH}_x$ nanocomposites for subsequent desorption (full symbols) and absorption (empty symbols) sweeps. Hatched areas stand for retained MgH_2 and unreacted Mg at each sorption sweep, respectively. The irreversible hydrogen content stored in the form of thermodynamically stable ETMH_x is displayed in grey at the bottom. The white area located between the upper and lower hatched ones gives the reversible capacity C_{rev} . Reproduced with permission [37]. Copyright 2019, Royal Society of Chemistry.

6. Other Mechanisms

The nature of the H–H interaction in interstitial hydrides is elastic and therefore intrinsically long-ranged [243]. A net H–H attraction can result from the lattice dilatation, which is induced by an interstitial H atom, is constant throughout the whole crystal, and favors the absorption of further H atoms [243]. In metal with elastically free surfaces, two hydrogen atoms exhibit an effective attractive interaction that leads to high desorption temperatures [244,245], while if the lattice is not free to expand (stress relaxation is reduced) upon H absorption, the elastic contribution to the reduction of the H–H interaction energy increases, and the H–H interaction might even become repulsive, resulting in an increased (i.e., less negative) ΔH [243,246]. Thus, clamping, which would induce a repulsive H–H interaction (instead of the usual attractive interaction) via the elastic constraints imposed by the material capping the magnesium [244,245], can be used to tune the hydride formation enthalpy and consequently the equilibrium/plateau hydrogen pressure to the levels required for specific applications according to the van't Hoff equation [20]:

$$\ln \frac{p_{\text{H}_2}^{\text{eq}}}{p^{\ominus}} = \frac{\Delta H^{\ominus}}{RT} - \frac{\Delta S^{\ominus}}{R} \quad (10)$$

where \ominus represents the reference state of 1 bar, and R is the gas constant. The elastic model suggested by Pasquini et al. [243] shows that the elastic constraint in 3-D core-shell NPs, where the core is a hydride-forming metal, can exert a remarkable effect on the thermodynamic stability of the core in its hydride phase, which decreases with increasing stiffness and thickness of the shell and with decreasing NP size, inducing a change in its formation enthalpy on the order of 20–30% if a suitable morphology and proper elastic parameters coexist. Baldi et al. [245] believed that for Mg thin films capped with different TMs, two behaviors are clearly distinguishable:

1. Mg-alloy-forming TM elements, such as Ni and Pd, alloy between Mg and the top layer, leading to a strong clamping effect on the thermodynamic properties of Mg. This results in a much higher hydrogen plateau pressure (increased hydride formation enthalpy) than that measured for Mg films of equal thickness capped with Mg-immiscible elements such as Ti, Nb, and V. This is consistent with the finding that alloying at the interface between the Mg film and the clamping layer (Pd or Ni) adds to the elastic clamping, making it difficult to separate the two contributions to hydride destabilization [243,247,248].
2. Mg-immiscible elements effectively behave like “scissors” and lead to “quasifree” Mg layers with elastically disconnected interfaces. However, based on the assumption that MgH_2 and TiH_2 form immiscible phases, the DFT calculation performed by Hao and Sholl [249] indicated that among the low surface-energy faces of MgH_2 (Mg) and TiH_2 (Figure 33), strong epitaxial interfaces with favorable interface formation energy (an important feature for elastic clamping) can be formed; the strain induced by these interfaces in MgH_2 and Mg can exert a significant influence on the hydrogen desorption enthalpy of MgH_2 .

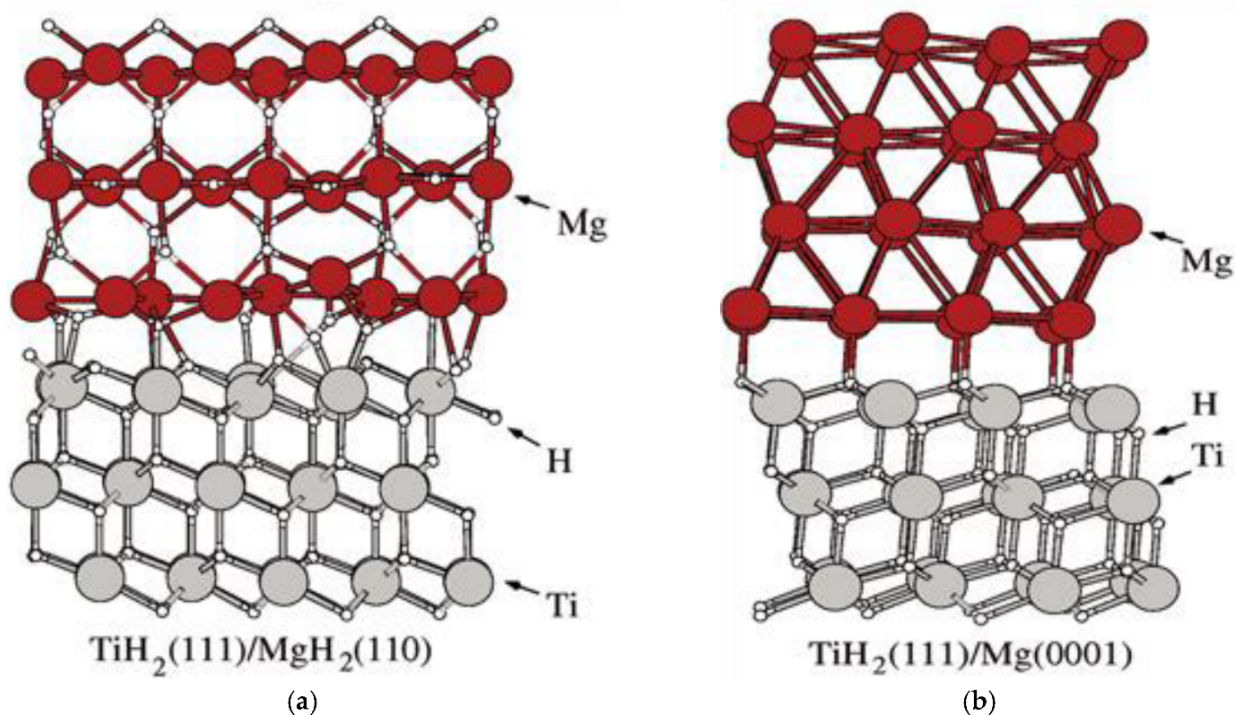


Figure 33. (a) Interface structure of $\text{TiH}_2(111)\text{--MgH}_2(110)$. (b) Interface structure of $\text{TiH}_2(111)\text{--Mg}(0001)$. (a,b) Reproduced with permission [249]. Copyright 2011, American Chemical Society.

Another key finding of the calculations is that, when the thickness of the TiH_2 substrate is large enough that the lattice constant of TiH_2 can be fixed at its bulk value, the reaction enthalpy can be reduced relative to that of bulk MgH_2 by $5\text{--}12\text{ kJ mol}^{-1}\text{ H}_2$, with the largest changes occurring for very thin MgH_2 films, while in systems where both the MgH_2 (or Mg) and TiH_2 lattice constants are allowed to relax, the reaction enthalpy is only reduced by $\sim 4\text{ kJ mol}^{-1}\text{ H}_2$. This finding suggests that making the grain size/film thickness ratio between MgH_2 and TiH_2 as small as possible will produce substantial improvement in thermodynamics relative to bulk MgH_2 [249]. Despite the controversy over the clamping effect in Mg thin films capped with different TMs, one can expect that in a $\text{core}(\text{MgH}_2)\text{@shell}(\text{TM})$ structure, the clamping effect always exists regardless of the TM present. This is because, in all-sides clamped metal–hydrogen systems, the H–H interaction becomes repulsive [245,250].

Based on the above discussion and the finding that elastic contributions increase with increasing coherency (i.e., evolving stress contributions are largest at coherent interfaces), while at semi- or incoherent interfaces formed by plastic deformation, stress can be partially released [246], it can be deduced that the clapping efficacy of a certain TM layer of the same stiffness and thickness follows this degressive order: core(MgH₂)@shell(TM) structure when TM and Mg forming alloy, core(MgH₂)@shell(TM) structure when TM immiscible with Mg, MgH₂ film capped by TM layer when TM and Mg forming alloy, and MgH₂ film capped by TM layer when TM immiscible with Mg. Based on one study on the hydrides of ETMs as grain-growth inhibitors of Mg that tentatively attributed the grain-growth inhibition effect of ETMH_x to coherent coupling between Mg and ETMH_x due to their close molar volume [37], the coherency of interfaces can also be considered to be related to the difference in molar volumes of Mg and TM dihydride. In addition, considering the expansion–strain–de/absorption mechanism for Mg₂Ni as a hydrogen pump during the hydrogen absorption of Mg, the volume expansion from Mg₂Ni to Mg₂NiH₄ may weaken the clamping effect of Mg₂Ni. However, in another study, this factor could not be considered for the clamping effect of Pd, since Mg₂Pd could not absorb hydrogen [128]. Thus, one must first determine whether the Mg–TM alloy has a corresponding hydride phase or even whether Mg-immiscible TM immiscible can form a TM–Mg–H ternary hydride to estimate the clamping effect of a given TM. It is also worth mentioning here that the repulsive H–H interaction in such systems may suppress the phase transition from Mg to MgH₂ [250] as the accumulation of hydrogen in compressively stressed lattice regions is restrained [246].

TM-enhanced hydrogen diffusion in MgH₂ may be explained by the mechanisms below.

1. The presence of large concentrations of TM impurities doped into MgH₂ can shift the Fermi level depending on the position of the TM acceptor/donor levels in the band gap, thereby influencing the formation energy and the concentration of the hydrogen vacancies that govern hydrogen diffusion [251]. In addition, TM dopants in a MgH₂ cell can influence the energy barrier in hydrogen vacancy diffusion. For example, the DFT calculations carried out by German and Gebauer [252] showed that the energy barrier in hydrogen vacancy diffusion is reduced by between 16% and 73% in Nb- and Zr-doped bulk magnesium hydride compared with the pure bulk magnesium hydride. This effect arises from the fact that TM impurities can influence the charge-neutrality condition of wide-band-gap insulators such as pure MgH₂, in which free carriers are not present, defects exist in charged states, and the Fermi level is pinned close to a position in the gap where the formation energy of the dominant and negatively charged native defect equals that of the dominant and positively charged defect [251]. Since the charge-neutrality condition, which determines the Fermi level, involves the concentration of the cation and anion in the system, it is imperative to better understand the charge transfer trends in TM-doped MgH₂ that were discussed in Section 3.3.
2. The presence of TM catalysts increases the adhesion of the MgH₂–Mg interfaces by shortening the bonding distances with the nearest atoms (both H and Mg), which causes changes in the nearest shells of coordination. This creates an empty space that facilitates the displacement of the surrounding atoms, leading to a local destabilization of the lattice that favors the diffusion of the H atoms toward the interface [253]. For example, DFT calculation showed that Fe coordination that is higher than the Mg coordination in the hydride creates a void in the second H-shell that is partially filled by the nearest Mg atoms and thereby facilitates the diffusion of H atom from MgH₂ to hcp Mg (Figure 34) [253]

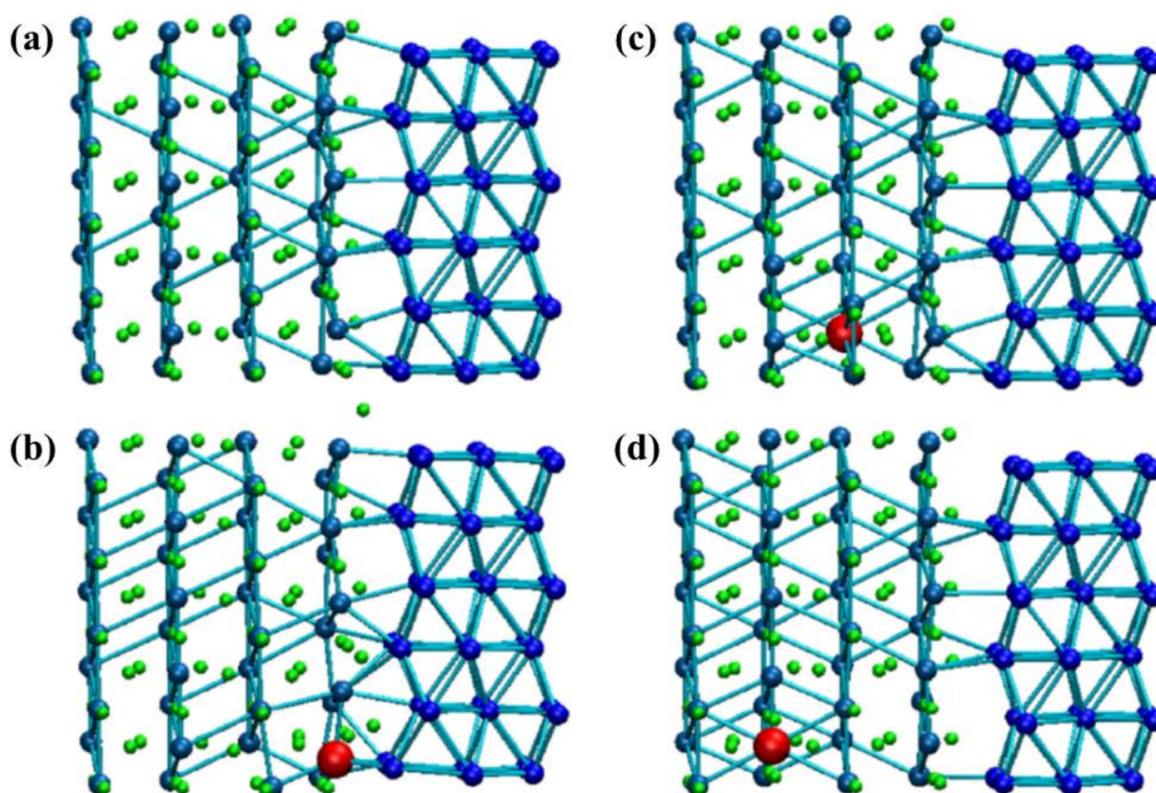


Figure 34. Snapshots of the MgH_2 –Mg interface without Fe catalyst and with Fe in POS1 (first Mg layer in the MgH_2 side), POS2 (second Mg layer in the MgH_2 side), and POS3 (third Mg layer in the MgH_2 side) at the end of ionic relaxation: panels (a), (b), (c), and (d), respectively. H atoms are in green, Mg atoms are in light (MgH_2 side) and dark (Mg side) blue, and the Fe atom is in red. (a–d) Reproduced with permission [253]. Copyright 2013, Elsevier.

- TM additives may change phase transformation process in magnesium during hydrogenation and thus improve the hydrogen diffusion process (Figure 35). In pure Mg, in the initial stage of hydrogenation (low hydrogen concentrations), the bcc (body-centered cubic) structure of Mg is less stable than both the hcp (hexagonal closed packed) and fcc structures, with the energy difference increasing as the hydrogen concentration increases. Upon hydrogenation-induced phase transformation to the rutile type (Figure 35 Schema 1) with hydrogen concentration close to 2 in MgH_x , the fcc stacking mode becomes more favorable [42]. The presence of TM layers or TM particles at the surface of the Mg grains should help locally stabilize the bcc-Mg arrangement (Figure 35 Schema 2), in which hydrogen diffusion is faster than in hcp- and fcc-Mg arrangements due to the lower activation energy E_a and the homogeneous distribution of hydrogen atoms over tetrahedral sites [42]. The latter fact prevents the so-called blocking layer effect, which is observed in other Mg lattices (hcp and fcc), because hydrogen atoms prefer to occupy adjacent interstitial sites, forming clusters [42,254–256]. It should be noted here that, with or without TM additives, sufficiently high local hydrogen concentration should allow for the clustering of MgH_2 aggregates, leading to a martensitic transformation involving the intermediate fcc- MgH_x structure that form the tetragonal bct (as found in the rutile MgH_2) of the Mg metal lattice [42].

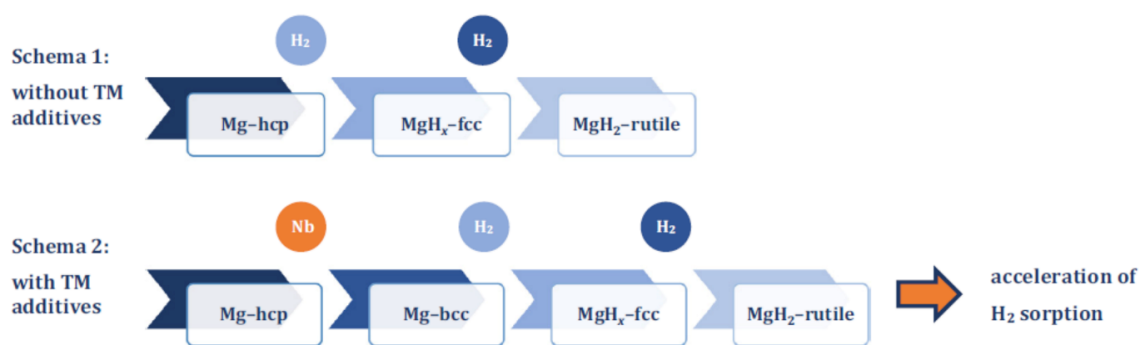


Figure 35. Scheme of hydrogen-induced structural phase transitions in Mg with and without TM additives. Reproduced with permission [42]. Copyright 2015, Elsevier.

In general, the use of TM compounds makes it difficult to determine the catalytic mechanism. TMs in TM-containing oxides are readily reduced to low-valence species and even zero-valence metals by reacting with MgH_2 due to the powerful reducing capability of MgH_2 [51,86,186,192,220,257–264]. Thus, some researchers [51,86,186,258–260] have proposed that metallic TM is the actual/key active catalytic species, while other researchers [192,261] have proposed that the unreduced TM-containing oxides or partly reduced TMs with lower oxidation states constitute the primary catalytic phase. Furthermore, $\text{Mg}_x\text{TM}_y\text{O}_z$ is believed to possess a significant role in the catalysis of TM-containing-oxide– MgH_2 systems, and it has been widely reported that in TM-containing oxides loaded with MgH_2 in situ, $\text{Mg}_x\text{TM}_y\text{O}_z$ (possibly of more than one type) may form as a result of the interaction between MgH_2 and TM-containing oxides [258,264–268]. While not considering the reaction between MgH_2 and TM-containing oxides, Liu et al. [269] suggested that oxygen vacancies are responsible for the decrease of hydrogen desorption temperature and activation energy of ball-milled $\text{Mg}-x\text{CeO}_2$ ($x = 0.7, 1.5, 3$, and 6 mol.%). Since the possible various products of the reaction between MgH_2 and a TM-containing oxide provide a multivalent environment of TMs, another charge transfer mechanism can be suggested. Compared with a single-valence TM atom, which affects the charge transfer between TM, H, and Mg in Mg–TM–H systems primarily through the “ χ rule”, multivalence TMs were reported to primarily act as intermediates during electron transfers between Mg^{2+} and H^- , which facilitated the recombination of H_2 on compounded TM surfaces [270].

Cui et al. [270] coated a Ti-based multi-valence catalyst of ~ 10 nm thickness and multiple valences in the form of Ti (0), $\text{TiH}_2(+2)$, $\text{TiCl}_3(+3)$, and $\text{TiO}_2(+4)$ on the surface of ball-milled Mg powders (~ 1 μm in diameter) via the chemical reaction between Mg powders and TiCl_3 in THF solution (Figure 36a–c). According to the change of valence states demonstrated in Ti 2p photo-electron lines for the de/hydrogenated samples, the authors [270] inferred that the electronic structure of Ti-based catalysts changes during the de/hydrogenation process. They described the electron transfers in the dehydrogenation process of the sample with the following steps (Figure 36d,e): (1) transformation of high valence Ti ($\text{Ti}^{3+/4+}$) into low valence Ti (Ti^{2+}) as a result of the transfer of e^- from H^- at the interface between MgH_2 and Ti compounds; (2) weakening of the Mg–H bond, formation of dissociative H, and initiation of the dehydrogenation reaction, followed by the nucleation and growth of Mg along with H_2 molecule recombination. Conversely, the hydrogenation process was described with the following steps (Figure 36d,e): (1) dissociation of H_2 into H, which receives e^- from low valence Ti (Ti^{2+}), leading to the formation of high valence Ti ($\text{Ti}^{3+/4+}$); (2) formation of Mg–H bonds and the initiation of the hydrogenation reaction, followed by the nucleation and growth of MgH_2 . The authors [270] proposed that the de/hydrogenation process of MgH_2 becomes easier due to the lower energy needed in the above inferred catalytic process (Figure 36f).

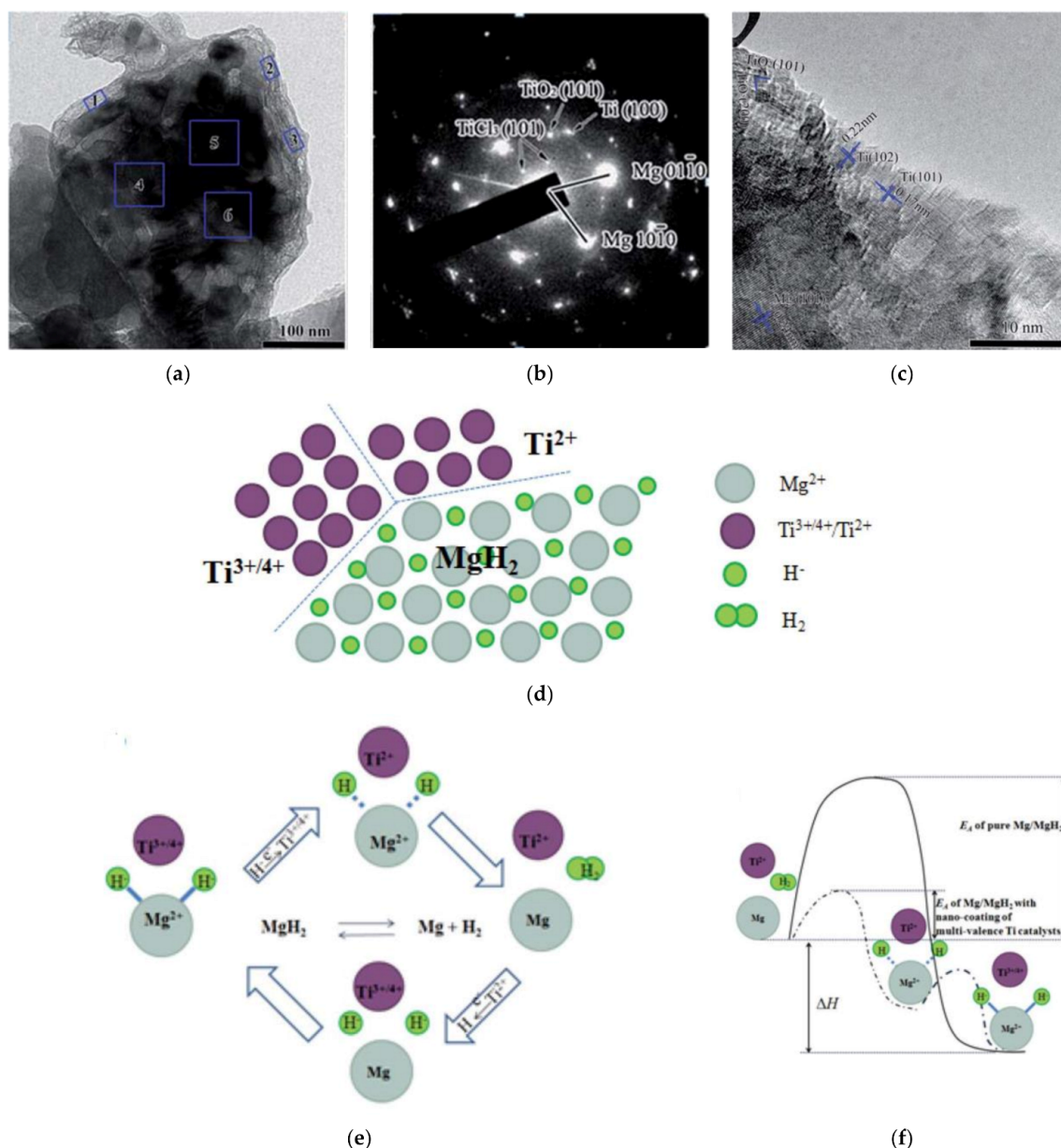


Figure 36. TEM micrographs of the samples as prepared by the chemical reaction between Mg powders and TiCl₃ in THF solution. (a) Bright field, (b) electron diffraction pattern, (c) HR-TEM images. (d–f) The schematic diagram of the catalytic mechanism in de/hydrogenation of the samples. (a–f) Reproduced with permission [270]. Copyright 2013, Royal Society of Chemistry.

While the above-described charge transfer mechanism does not involve the “ χ rule” for metallic TMs, Figure 37 shows that when the TM oxide is regarded as a “whole”, the “ χ rule” can still predict the stability of MgH₂ without needing to consider the effect of the possible reactions between MgH₂ and TM oxide on the stability of MgH₂. Similar to TM-containing oxides, an identical issue arises upon determining the catalytic mechanism of TM fluorides. A study on the hydrogen storage properties of core-shell-structured Mg–TMF_x (TM = V, Ni, La, and Ce) nano-composites prepared by arc plasma method indicated that the catalytic mechanism of TM fluorides involves oxidized TM nanoparticles covering Mg (MgH₂) particles due to the passivation of TM that is produced by the reaction between TM fluorides and Mg during arc plasma evaporation [271]. It was also reported

that adding TM fluorides into MgH_2 significantly accelerates the sorption kinetic process through the following reaction [146]:



Zheng et al. [272], based on the formation of TiH_x and MgF_2 as observed by XRD in dehydrogenated TiF_3 -doped MgH_2 , believed that electronegative H atoms may interact with Ti^{3+} , Mg, and F ions. As a result, the initial Mg–H bonds in MgH_2 are jointly weakened by the Ti and F ions of the TiF_3 and thus energetically favor the formation of the intra-H···H pairings in MgH_2 .

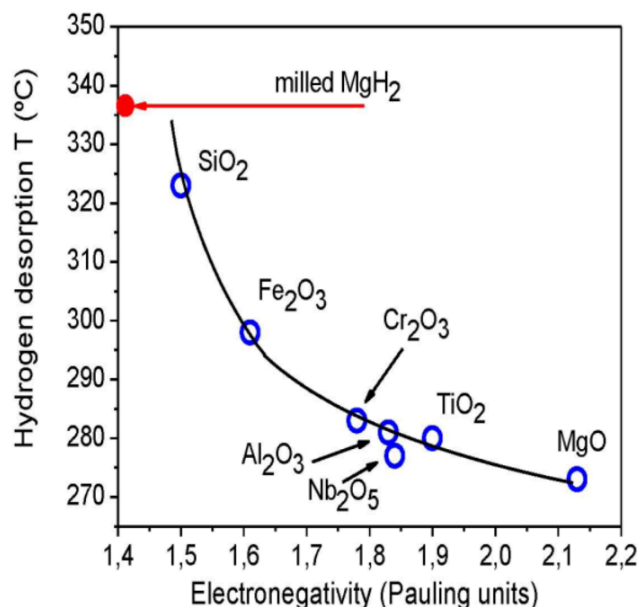


Figure 37. Correlation of the desorption temperature of hydrogen from MgH_2 , achieved upon oxide addition during milling and the electronegativity of the oxide additives. Reproduced with permission [273]. Copyright 2012, MDPI.

When multiple TMs are co-doped, one TM may affect the catalytic effect of another TM, or a synergistic effect between these TMs may occur. The DFT calculation results of Zhang et al. [184] indicate that the addition of Cu atoms increases the hybridization between $\text{Ni}_1(d)$ and $\text{H}(s)$ orbitals, suggesting an enhancement of covalent bond interactions between Ni and H after Cu doping. Based on the synergistic catalytic effect of Co/ TiO_2 nanocomposite on the hydrogen de/absorption properties of MgH_2 , Chen et al. [274] suggested that during the dehydrogenation process, the nearly full d band electron structure of Co causes Co to have a higher bond strength with H (Co–H) than Mg–H, thus facilitating the destabilization process of MgH_2 . In this case, the electrons around Co that form as a result of the migration of the thermally excited conduction band electrons of TiO_2 to the surfaces of Co due to the higher Fermi level of TiO_2 facilitate the reduction of Mg^{2+} to Mg, while the holes around TiO_2 facilitate H^- interfacing between Mg/ MgH_2 and Co/ TiO_2 to form H_2 . In addition, when Ni and another TM are co-doped in MgH_2 , a synergistic effect of Mg_2NiH_4 as a “hydrogen pump” with the TM can be observed.

Recently, Ma et al. [275], according to their observed microstructure and phase change, proposed a dehydrogenation mechanism for hydrogenated MgH_2 –TMA–TM MOFs (TMA = trimasic acid, TM = Fe, Ni) composite through the synergetic catalytic effects of in-situ-formed nano- Mg_2Ni and α -Fe derived from TMA–TM MOFs. In other words, the phase change of $\text{Mg}_2\text{NiH}_4/\text{Mg}_2\text{Ni}$ worked as a “hydrogen pump” to provide fast delivery channels for H atoms; meanwhile, α -Fe promoted the nucleation and growth of Mg on the MgH_2 – α -Fe interface by destabilizing the crystal structure of MgH_2 and reducing the nucleation energy of Mg. Huang et al. [214] showed that in the context of the catalytic effect

of NiTiO_3 on the hydrogen desorption performance of MgH_2 , Ti in a MgH_2 matrix with a multi-valence series (Ti^{2+} , Ti^{3+} , Ti^{4+}) and formed Mg_2NiH_4 can work like a “multistage pump” (Figure 38). The mechanistic steps might be described as follows: (1) Mg_2NiH_4 completes the hydrogen release to form Mg_2Ni in advance, compared with the hydrogen release from MgH_2 ; (2) H^- transfers an electron to Ti^{4+} to form H, while Mg^{2+} obtains electrons from Ti^{2+} to form neutral Mg, agreeing with the mechanism described in Figure 36; (3) H atoms diffuse to Mg_2Ni to release H_2 rather than diffuse to vacuum directly by the solid–gas interface.

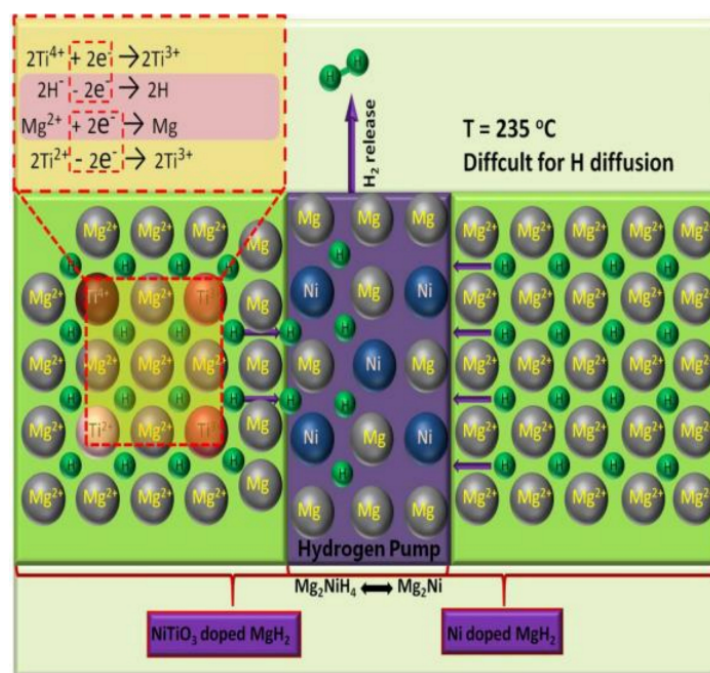


Figure 38. Schematic diagram of the catalytic mechanism of Ti and Ni in MgH_2 hydrogen storage system. Reproduced with permission [214]. Copyright 2018, American Chemical Society.

The surface morphology of TM-based catalyst can influence the catalytic effect. For TiO_2 catalysts, {001} facets may provide more active sites than {101} facets. Compared with {101} facets that expose both six-coordinated and five-coordinated Ti, {001} facets with low coordination of surface atoms expose five-coordinate Ti completely, which provides large numbers of active sites and therefore more options for electron transfer and interaction, leading to greater chemical reaction activity [276,277].

According to the DFT calculations conducted by Zhang et al. [278] to understand the catalytic effect of TiO_2 nanosheets on the hydrogen storage properties of MgH_2 , exposed high-surface-energy {001} facets had an average surface energy of 0.90 J m^{-2} , which was higher than the 0.44 J m^{-2} that was found for the {101} facets. Thus, a more reduced activation energy of MgH_2 can be expected if a TM-based catalyst with exposed high-surface-energy facets is doped. According to the work of Dai et al. [178,218], the influence of the surface morphology of MgH_2 on the mechanisms that cause TM dopants to improve the dehydrogenation properties of the MgH_2 surface should also not be negligible. They confirmed a stronger influence of Mn on the Mg–H bonding interactions in the vicinity of Mn on the MgH_2 (001) surface than on the MgH_2 (110) surface. This was caused by the Mn atom not bonding with all its surrounding H atoms on the MgH_2 (110) surface.

Instead of an interstitial intermetallic hydride, Mg_2NiH_4 is considered as a complex hydride due to hydrogen atoms being placed in the vertices of $[\text{NiH}_4]^{4-}$ tetrahedra in Mg_2NiH_4 , forming strong bounds with the central nickel atom [31]. Therefore, in spite of the much weaker Ni–H interaction in Mg_2NiH_4 than that in pure MgH_2 [34] and the higher affinity of Mg for hydrogen than Ni in binary metal hydrides [128], in Mg_2NiH_4 , the interac-

tion of Ni–H is stronger than Mg–H [128]. This implies that the TM–H interaction strength in the Mg–TM–hydride is also related to the crystal structure of the Mg–TM–hydride. In addition, as seen in Figure 39 in general, the larger the unit cell volume is, the less stable the Mg–TM–H system is. The catalytic effect of different TMs may change to different degrees during the hydrogen absorption and desorption cycles (Figure 40), which may be caused by severe microstructural modifications, including migration of TM catalysts, formed upon long-term cycling [37]. The “hydrogen spillover” effect of Mg₂Ni(Cu) phases formed in situ, which give rise to the enhanced hydrogen sorption kinetics of MgH₂/Ni–50%Cu, was reported by Zhang et al. [184], suggesting the important role of “hydrogen spillover” in the hydrogen sorption kinetics of MgH₂. However, although the “hydrogen spillover” mechanism has been reported in many kinds of metal-doped hydrogen storage materials [53,114,200,225,279–287], the study of the TM-depended influence of this mechanism on the hydrogen sorption properties of the Mg–TM–H system is rarely reported.

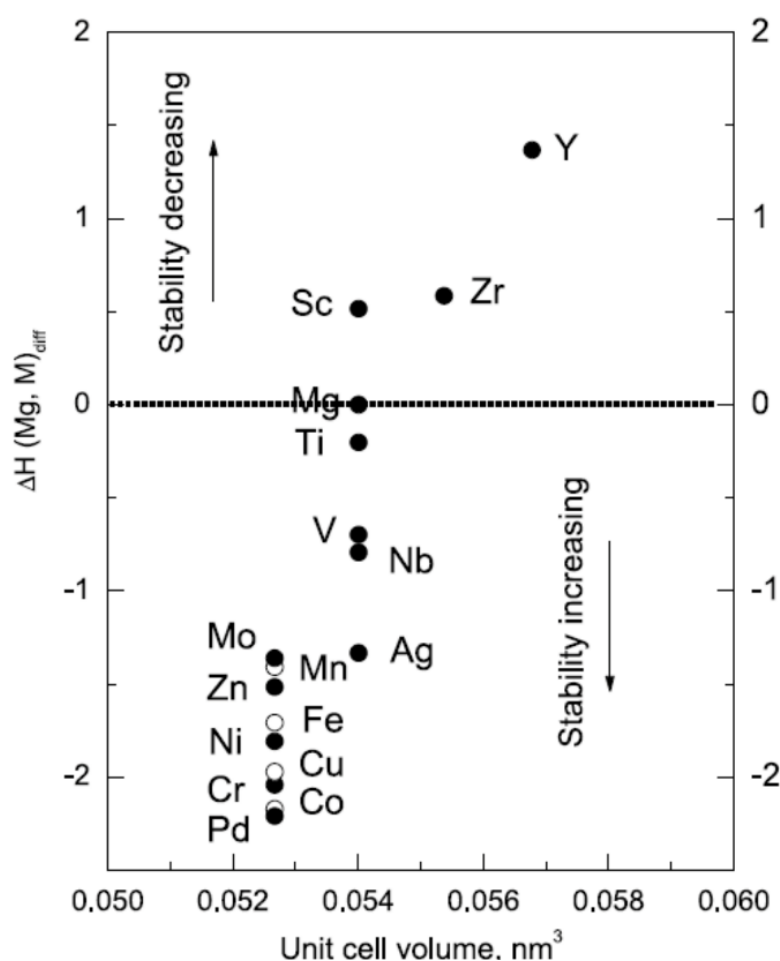


Figure 39. Calculated enthalpy difference $\Delta H(\text{Mg, TM})_{\text{Diff}}$ depends on the unit cell volume of Mg(TM)H₂ cluster containing 32 magnesium atoms, 1 TM atom, and 64 hydrogen atoms. When solid and open circles in figure overlap, the solid circle represents an element to the left of it, and the open circle, to the right of it. Reproduced with permission [182]. Copyright 2003, Elsevier.

For the benefit of nano-sized free-standing Mg/MgH₂ to more exposed atoms at the surface, the surface energies of both Mg and MgH₂ increase with the larger surface energy of MgH₂ rather than that of Mg [288,289]. Thus, MgH₂ destabilized more strongly than Mg, leading to a decreased enthalpy for de/hydrogenation temperature [98,289–295] according to van’t Hoff plot [296]:

$$T_d = \Delta H / \Delta S \quad (12)$$

where T_d is hydrogen desorption temperature, and ΔH and ΔS are the enthalpy and entropy of hydrogen desorption, respectively. Indeed, several experiment reports have shown a decrease in the enthalpy as low as 44.5–66 kJ mol^{−1} H₂ [297–300] and a significant decrease in the hydrogen release temperature (from >573 K to 526 K) for Mg nanoparticles with sizes below 4 nm [297,300,301]. However, theoretical calculations predicted that the reduced reaction enthalpy of MgH₂ nanoparticles relative to the bulk material can be realized only when the particles are smaller than 2 nm and containing <50 Mg atoms [27,302,303]. For example, it was theoretically predicted that the ΔH can be reduced to 63 kJ mol^{−1} H₂ at the size of 0.9 nm, and the corresponding T_d can be remarkably reduced to ~473 K if the ΔS is considered as a constant of ~130.5 J mol^{−1} K^{−1} [302], which is typical for a bulk MgH₂ system [304]. Discrepancies between the theoretical and experimental results are usually believed to originate from the complexity of the small nanoparticles, where thermodynamic properties can be strongly affected by several parameters such as the surface state of the studied material [31]. Regardless of this controversy, it can be confirmed that the significant decrease of ΔH of MgH₂ occurs only when the particles are a few nanometers.

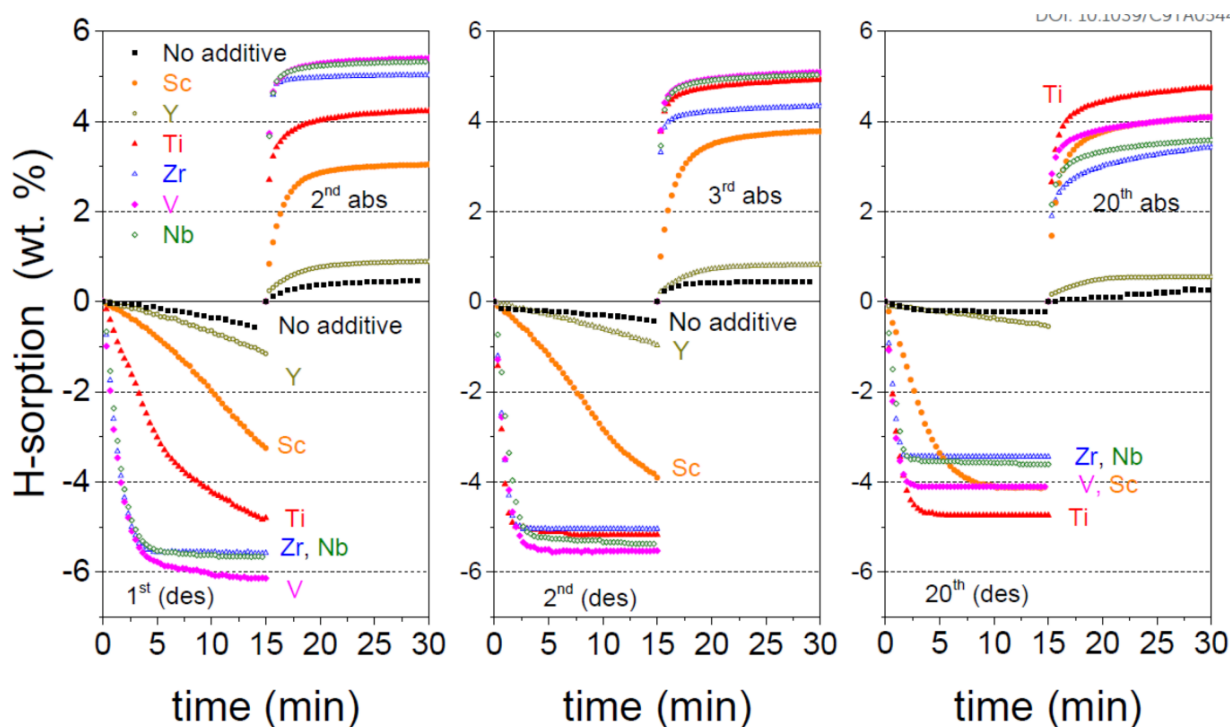


Figure 40. Hydrogen sorption curves at 573 K of MgH₂–ETMH_x nanocomposite for different sorption sweeps. Absorption and desorption hydrogen pressures are fixed to 0.8 and 0.03 MPa, respectively. Sorption time is limited to 15 min. Reproduced with permission [37]. Copyright 2019, Royal Society of Chemistry.

It should be also noted that despite such small particle sizes, the temperature at which hydrogen can be released is limited by the observed enthalpy/entropy compensation effect; i.e., the significant reduction of enthalpy is also accompanied by a decrease in entropy (Figure 41), limiting the hydrogen release at low temperatures, which challenges the idea of reaching low desorption temperatures via a nanosizing approach [20,133,300,305]. For instance, a significant decrease of the ΔH (63.8 ± 0.5 kJ mol^{−1} H₂) and the ΔS (117.2 ± 0.8 J mol^{−1} K^{−1}) was reported in MgH₂ nanoparticles with sizes of less than 3 nm by hydrogenation of Bu₂Mg inside the pores of a carbon scaffold. Although the ΔH was greatly decreased, the decrease of the T_d was only 11 K because of the counter effect of the decreased ΔS [133]. ΔS also increases with the concentration of dissociated H on the surface of Mg/MgH₂ particles; this depends on the activity and efficiency of catalyst on H₂ dissociation and hence, increases with the decrease of activation energy for H₂ dissociation [296]. A first-principles study

of the thermodynamic and electronic properties of Mg and MgH₂ nanowires showed that the band gaps and the hydrogen desorption energies of MgH₂ nanowires are controlled by the size of MgH₂ nanowires and that the surface effect and quantum size effect can be induced as the size of MgH₂ nanowires decreases [201]. The surface effect is based on the observation that the partial charge density distributions corresponding to the valence band maximum (VBM) and the conduction band minimum (CBM) are mainly located on H atoms and Mg atoms on the surface of the MgH₂ nanowire, respectively [201]. The effect of sizes of MgH₂ nanowires on the band gaps and hydrogen desorption energy is shown in Figures 42a and 42b, respectively. The extra surface electronic states lead to smaller band gaps in the MgH₂ nanowires than those of the bulk MgH₂ crystal, while the quantum size effect results from the increase of the band gaps of MgH₂ nanowires as the diameters of MgH₂ nanowires decrease [201]. The above discussion suggests at least two possible mechanisms for how TM exerts influence on the hydrogen sorption properties of free-standing nano-sized MgH₂: (1) the *d* band of TM atoms offsets part of the quantum size effect to enhance the hydrogen desorption kinetics; (2) the TM catalyst influences the activation energy for H₂ dissociation and thereby the value of ΔS , controlling the value of T_d . However, whether TM-based materials can act as a (de)hydrogenation catalyst for very small MgH₂ particles has not been confirmed. For example, to see whether the H-sorption properties of MgH₂ particles that were milled for 700 h (MgH₂^{700 h}), most of which have a nanometric size (Figure 43a,b), could be further improved, Aguey-Zinsou et al. [306] milled MgH₂^{700 h} with 17 wt% of Nb₂O₅ for 200 h, and observed no further improvement but only a loss of capacity due to the 17 wt% of Nb₂O₅ (Figure 43c). Hence, further investigation on possible catalytic mechanisms of TM for hydrogen sorption properties of free-standing nano-sized MgH₂ is required.

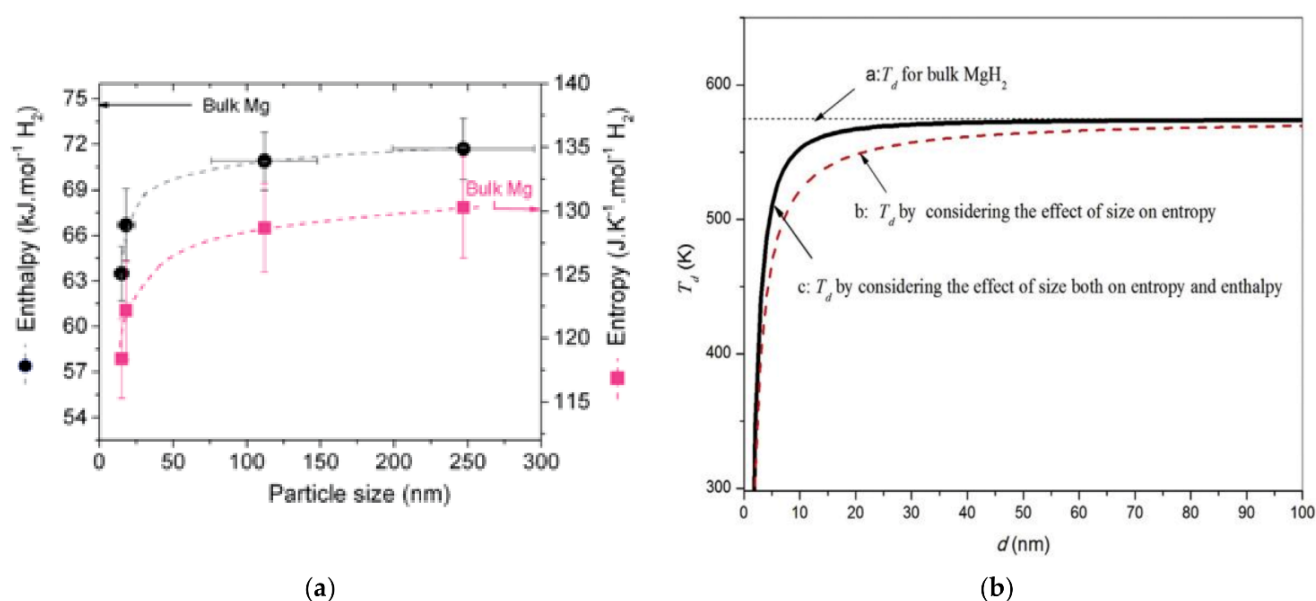


Figure 41. (a) Associated evolution of ΔH and ΔS versus the size of the magnesium nanoparticles. The dot line is a guide to the eye. Reproduced with permission [305]. Copyright 2014, Royal Society of Chemistry. (b) The curve of dehydrogenation temperature under 1 atm depended on grain size/particle size. Reproduced with permission [296]. Copyright 2017, Elsevier.

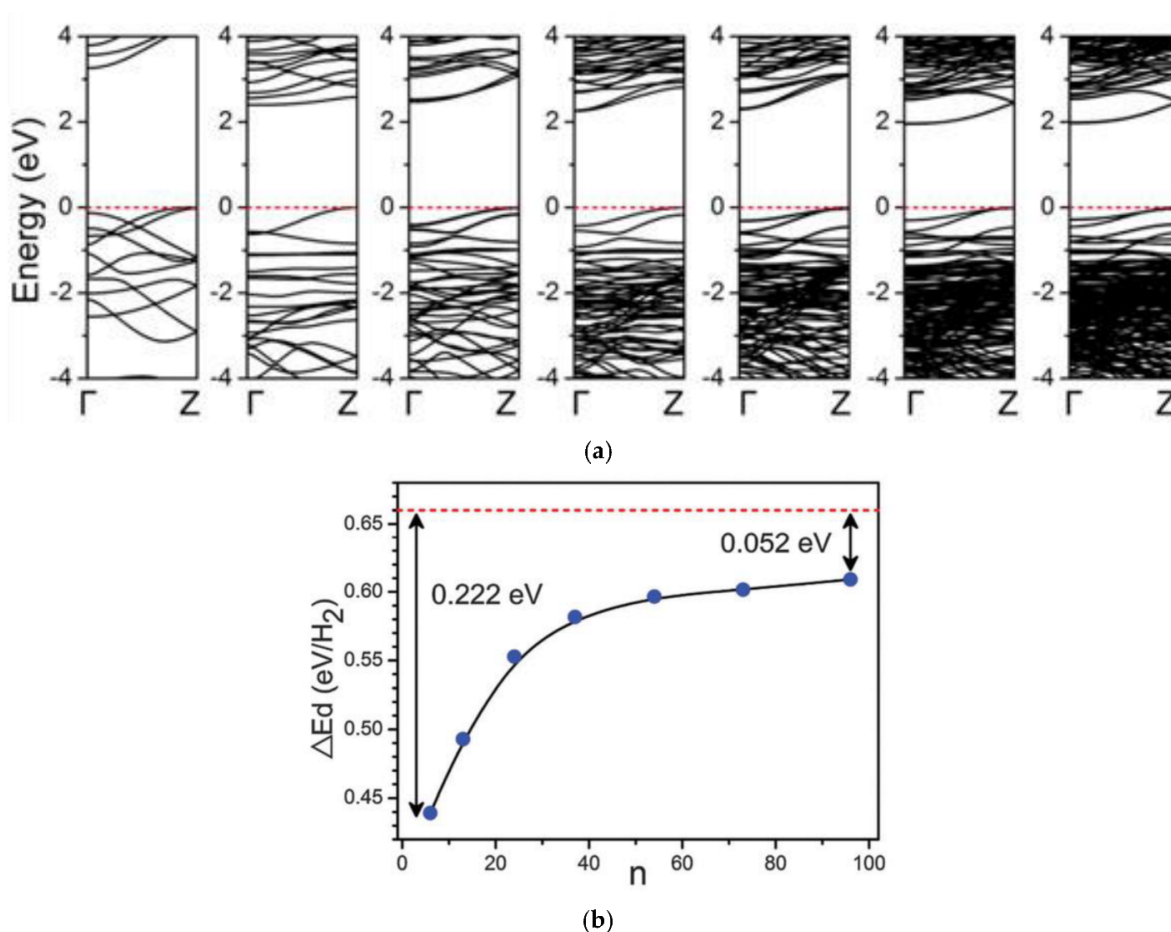


Figure 42. (a) Band structures of MgH₂ (n , D) nanowires, from left to right: MgH₂(6, 0.63), MgH₂(13, 0.87), MgH₂(24, 1.25), MgH₂(37, 1.56), MgH₂(54, 1.94), MgH₂(73, 2.25), MgH₂(96, 2.63) nanowire. The Fermi level is set to zero by the red horizontal line. n is the number of Mg atoms in the supercells and D is the calculated diameter in nm. (b) Hydrogen desorption energy ΔE_d (eV per H₂) of MgH₂ nanowires. Red dashed lines represent the hydrogen desorption energy of the bulk MgH₂ crystal. (a,b) Reproduced with permission [201]. Copyright 2016, ROYAL SOCIETY OF CHEMISTRY.

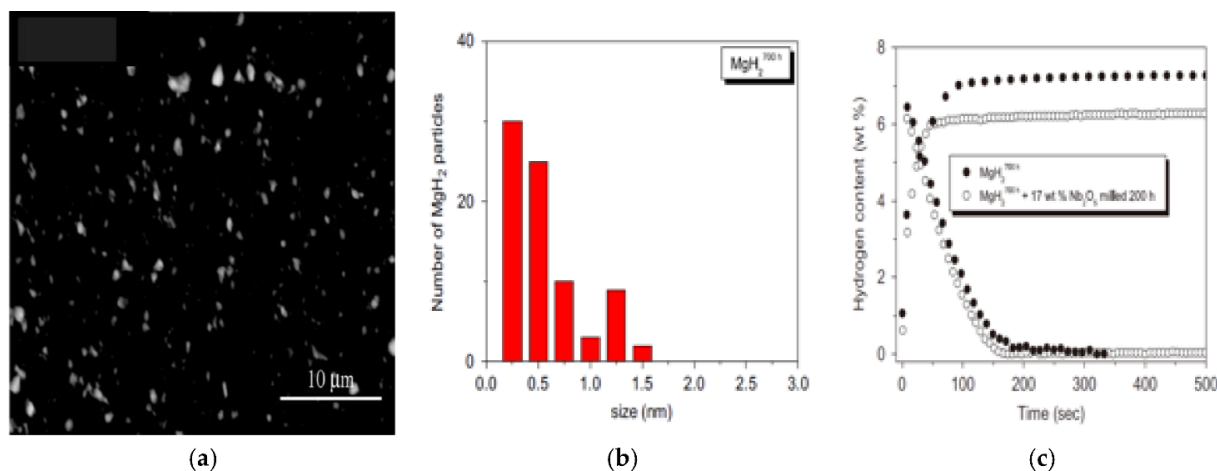


Figure 43. (a) SEM backscattered electron image of MgH₂^{700h}. (b) distribution of MgH₂^{700h} particle size determined by the analysis of the SEM image. (c) Absorption and desorption curves of MgH₂^{700h} and MgH₂^{700h} + Nb₂O₅ milled together for 200 h. (a–c) Reproduced with permission [306]. Copyright 2006, Elsevier.

Even now, it is difficult to find commercial magnesium hydride with a purity of more than 90% (despite the official specifications given by manufacturers) [3]. It has been also reported that even in a nominally fully hydrogenated bulk MgH_2 (hydrogen absorption at 623 K and 2 MPa for 20 hours), small islands of the Mg phase are still retained in the MgH_2 matrix (Figure 44a) [71]. Thus, the composition of magnesium hydride usually involves magnesium hydride, magnesium metal, which is present in the core of the particles (Figure 44b), and magnesium hydroxide contamination, which is usually present in the form of an amorphous layer on the surface of the particles [3]. However, it should be noted from Figure 44b that some Mg particles with small size are completely hydrogenated. Furthermore, Song et al. [257], based on the investigation on the hydrogen sorption properties of Mg by reactive mechanical grinding with Cr_2O_3 , Al_2O_3 , and CeO_2 , found that the quantities of absorbed or desorbed hydrogen increase as the average particle sizes decrease, implying that the decrease of the size of Mg particles to the nanoscale can be expected to increase the Mg to MgH_2 reacted fraction. As a general trend, the smaller crystal size is accompanied by the higher reacted fraction [37]. However, this trend may be broken in the $\text{TMH}_x\text{-Mg}$ system, as shown in Figure 45, which shows a deviation for some additives from a linear correlation between F and L_{MgH_2} ; that is, F is higher than expected for Zr-additive, whereas it is lower for V-additive. Rizo-Acosta et al. [37] believed that this scales with the relative difference in molar volume between the nucleating MgH_2 phase and ETMH_x hydrides (this difference is the lowest for Zr-additive, 11%, while it is the highest for V, 93%) and hence proposed that the nucleation of MgH_2 preferentially occurs at $\text{ETMH}_x\text{-Mg}$ interfaces and a lower molar volume difference between the nucleating MgH_2 phase and ETMH_x hydrides allows a lower energy barrier for nucleation.

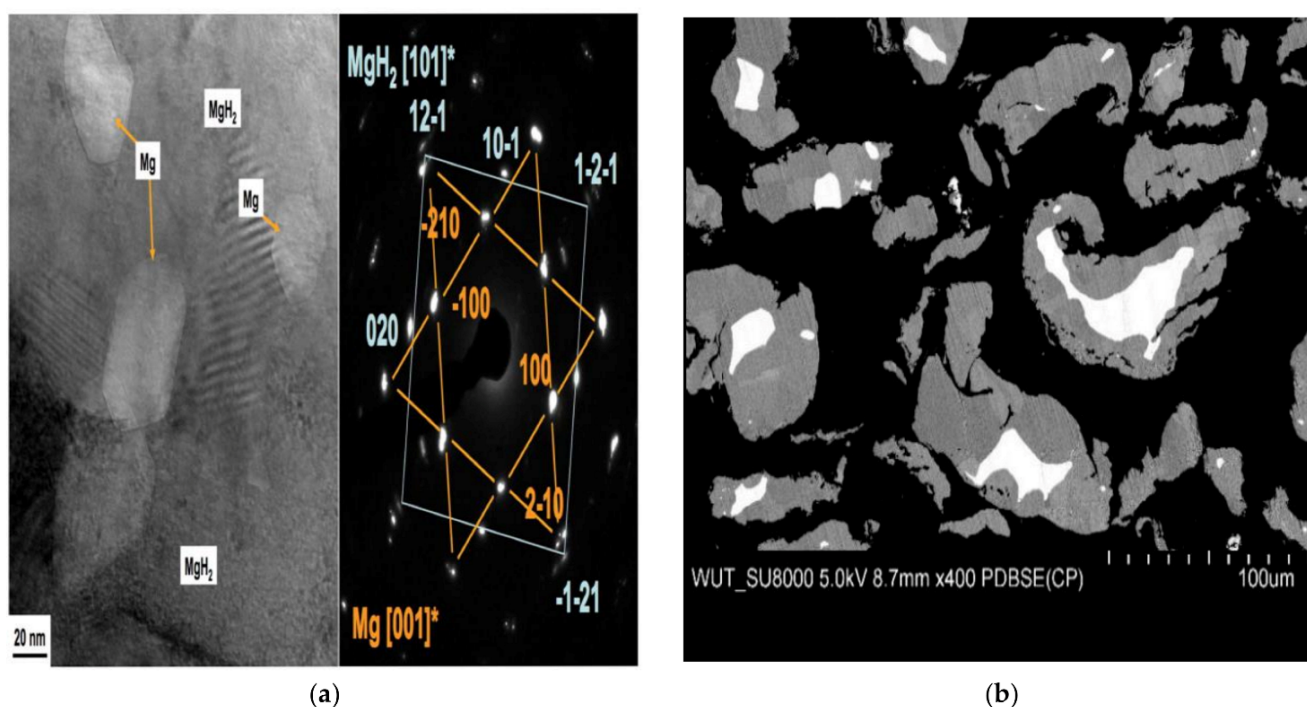


Figure 44. (a) A TEM image and selected area electron diffraction patterns from Mg and MgH_2 phases in a nominally fully hydrogenated sample. Reproduced with permission [71]. Copyright 2015, Springer Nature. (b) Cross-section of commercially available magnesium hydride particles with visible white magnesium cores. Reproduced with permission [3]. Copyright 2020, MDPI.

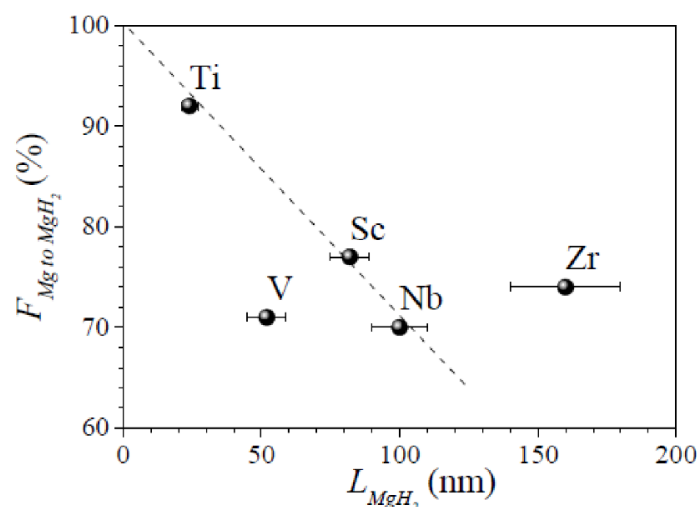


Figure 45. Dependence of the Mg to MgH_2 reacted fraction, F , on the MgH_2 crystallite size L_{MgH_2} for MgH_2 – $ETMH_x$ nanocomposites at the 20th absorption sweep. The dashed line is a guide to the eye. Reproduced with permission [37]. Copyright 2019, Royal Society of Chemistry.

7. Conclusions and Perspectives

An understanding of the mechanism by which TMs with d electrons influence the de/hydrogenation reaction of MgH_2 prove to be important to improve the process and to identify more efficient additives. However, pinpointing this mechanism is difficult due to series of practical issues, including variations in the amount of doped TM impurities, details of the physical and chemical states of the reactants resulting from ambient conditions (such as hydrogen partial pressure), and the synthesis process (such as duration and details of the ball-milling process, and the condition of the initial sample) [251]. In this paper, different mechanisms to explain the improved hydrogen sorption properties of TM-doped Mg/MgH_2 were reviewed. It is clear that TM dopants exist in Mg/MgH_2 in the following forms:

1. The Mg – TM – H ternary hydride is not formed when the Mg – TM intermetallic is formed (TM and Mg are miscible), which does not react with H_2 and form corresponding hydrides with MgH_2 forming and the alloying element precipitating in the form of element or new Mg – TM intermetallic instead. Typical TMs of this kind are Sc, Y, Cu, Ag, Cd, and Pd, which improve the hydrogen sorption properties of Mg/MgH_2 mainly by changing the dehydrogenation reaction path of MgH_2 to reduce the desorption energy and thereby the dehydrogenation temperature. Note from Equation (4) that, in addition to changing the dehydrogenation reaction path of MgH_2 , the hydride of RE element can also serve as the catalyst for dehydrogenation of MgH_2 .
2. The Mg – TM – H ternary hydride is formed when the Mg – TM intermetallic is formed (TM and Mg are miscible), which reacts with H_2 and forms corresponding hydrides. A typical TM of this kind is Ni, which catalyzes the hydrogen sorption properties of Mg/MgH_2 mainly by the “hydrogen pump” mechanism of the Mg – TM – H ternary hydride.
3. The Mg – TM – H ternary hydride is formed with H as glue. In this case, these TMs catalyze the hydrogen sorption properties of Mg/MgH_2 mainly by the “hydrogen pump” mechanism of the Mg – TM – H ternary hydride: (i) When the Mg – TM intermetallic is not formed (TM and Mg are immiscible); typical TMs of this kind are Ti, V, Cr, Mn, Fe, Zr, Nb, and Mo. ii) When the Mg – TM intermetallic is formed (TM and Mg are miscible), but the stable precursor is absent to produce a single hydride phase. A typical TM of this kind is Co. iii) The theoretical calculations on Mg_7ScH_{16} , Mg_7YH_{16} , Mg_7PdH_{16} , and Mg_7CdH_{16} suggest the possibility to form the Mg – TM – H ternary hydride when $TM = Sc, Y, Pd, \text{ or } Cd$, which expands the possible catalytic mechanism of these TMs in addition to the mechanism mentioned in case (1).

4. Mg–TM–H ternary hydride is not formed due to the absence of H as glue when the Mg–TM intermetallic is not formed (TM and Mg are immiscible) and the gigapascal hydrogen pressure thermal technique is not used. In this case, magnesium can be only slightly doped by TM elements.

Regardless of the form in which TM dopants exist in Mg/MgH₂, in the practical preparation process of TM-doped Mg/MgH₂, there is always atomic TM doped in Mg/MgH₂ in the forms of adsorption and substitution. In the case of atomic-TM substitution, the influence of TM on the interatomic interaction in TM-doped MgH₂ is mainly reflected in the TM–nnH ionic bond, the TM–nnH covalent bond, the nnnMg–nnH ionic bond, the nnnMg–nnH covalent bond, and the TM–nnnMg ionic bond. However, the relative contributions of these four interactions on $\Delta H(\text{Mg-TM})_{\text{Diff}}$ may vary in different Mg–TM–H systems. Thus, the results obtained regarding the changing trend of thermodynamic stability and interatomic bonding characteristics of TM-doped MgH₂ along TM series are not all the same. It can be confirmed that the destabilization of MgH₂ by TM doping is related to the specific interaction between the central TM atom and its immediate H neighbors (at least six octahedron of H atoms around a TM atom), which forms a tightly bounded multiple atom cluster with electronic distribution inside depending on the electronic structure of the TM impurity. In general, the denser and more homogenous electronic structure of the TM allows the stronger bonded TM–H clusters. In the cluster, vicinity bonds on atoms can be weakened as a result of the charge localization inside the clusters around TM and the strong bonding existing in them, and therefore the overall structure of the compound can be less stable in proportion to the amount of charge located inside the clusters, which is widely estimated by the *d* electron structure and the “ χ rule” of TM.

Compared with the “ χ rule”, the regularity of the influence of *d* electrons on interatomic interactions in TM-doped MgH₂ is not that strong; thus, our review proposed a relationship between electronic distribution inside TM–H clusters and the “ χ rule” and radius of doped TM elements, expanding the possible mechanism to explain the catalytic effect of TM-based materials on the hydrogen sorption properties of Mg/MgH₂. For atomic-TM substitution, the general “ χ rule” can be defined as the following: the increased χ -difference between TM and Mg and the increased χ -difference between TM and H enhance TM–Mg and TM–H bond strength, respectively, and thus a weakening of Mg–H bond strength. Nevertheless, estimating the Mg–H bond strength through TM–Mg and TM–H bond strength may be inaccurate, since the bond is directional. The “ χ rule” of charge transfer in TM-substituted MgH₂ can be proposed as the following: the charge transfer caused by the variation of $\chi(\text{TM})$ occurs mainly between the central TM, nnH, and nnnMg, and as $\chi(\text{TM})$ increases, the positive charge density of TM and the negative charge density of hydrogen atoms decrease. For a better explanation of the change trend of charge density of TM and H, we proposed the “radius effect” of TM, but some results still can not be explained. We suggest that the contribution of the “ χ rule” to the charge transfer trend between TM, H, and Mg, and thus to the interactions in the Mg–TM–H system, is the same for TM-substituted and adsorbed MgH₂. However, further investigations are required to determine this, since theoretical study of the charge density on TM, H, and Mg in the TM-adsorbed MgH₂ system is rare.

It should be noted here that whether the TM atom is adsorbed on the surface of MgH₂ or substitutes the Mg atom in the volume of MgH₂, tightly bonded H atoms with TM atoms lead to the easy breaking of the Mg–H bond but the difficult breaking of the TM–H bond. Obviously, a careful optimization including type, concentration, and spatial distribution of TM impurities in the MgH₂ crystal lattice is necessary to achieve the hydride with desired hydrogen sorption properties. The catalytic mechanism of TM near the surface of Mg is more complicated than that in the volume of Mg because of the competitive phenomenon between surface dissociation of H₂ and surface diffusion of H atoms, which depends on the kind and the doping sites of TM on the surface of Mg. Although the ‘*d* band center’ mechanism has been proposed to explain the influence of the kind of TM on this competitive phenomenon, the hindrance effect, which is related to the doping sites of TM,

leads to various possible contributions of the d band center to the dissociation of hydrogen molecules and the diffusion of hydrogen atoms nearby the surface of Mg, making the ‘ d band center’ mechanism more complicated. Furthermore, different from the theoretical calculation results shown in Figure 33a, experimentally, Ni, Fe, and Rh have not been reported to be the most effective catalysts [20], which indicates the imperfection of the d band center model and further highlights the difficulty of creating accurate models to help with the design of TM catalysts for the hydrogen/Mg reaction.

Compared with the thermodynamic stability of TM-doped Mg/MgH₂, which is controlled by multiple factors, the hydrogen sorption kinetics of TM-doped Mg/MgH₂ is mainly affected by the “hydrogen pump” mechanism. When the TM content is increased, an intervention between two competing factors, namely the speed up of the metal–hydride transformation and the loss of reversible capacity, may be observed, because the thermodynamic alteration comes at the cost of a reduced gravimetric capacity linked with the high weight fraction of TM [238]. However, a small amount of TM doping makes it difficult to change the thermodynamic stability of MgH₂. Therefore, to change the thermodynamics and kinetics at the same time, nano-sized Mg is required. The combination of freestanding nano-MgH₂ and nanocatalysts is expected to be an effective approach to achieve MgH₂ with enhanced hydrogen sorption properties but without losing significant H₂ capacity [307]. However, the fact that both nanostructuring and TM doping can facilitate one or multiple steps of the hydrogenation process makes the hydrogenation mechanism of nano-catalyzed Mg complicated. As a result, it is necessary to further investigate the relationship between hydrogenation kinetics, various catalysts, and refined nanostructure. To reveal the kinetic mechanism, a comparison of different kinetic models to analyze hydrogenation reactions is a useful approach [75,308]. Moreover, the clamping effect appeared to be a promising approach to realize the desired destabilization of Mg–H NPs in a detailed experimental assessment of the effect with special emphasis on its temperature dependence, stability upon cycling, and relation with the NPs size. The elastic model could be extended to NP shapes other than spherical [243]. Furthermore, it should also be noted that the various (even contradictory) trends of hydride stability with doped TM must be explained based on a combination of chemical (ionic plus covalent) bond nature and possible hydrogenation-induced lattice changes [182]. The close correlation of stability with unit cell volume would arise only in the case of much larger strain energy, which reflects the actual geometrical distribution of atoms rather than their chemical contributions [182]. More importantly, the modified hydrogen sorption mechanism in newly developed TM-doped Mg/MgH₂ systems should be determined in detail via reliable experimental and computational tools so that the related thermodynamic and kinetic properties can be elucidated to ensure technological reproducibility [12].

Author Contributions: Conceptualization, J.L. and A.L.; validation, J.L., V.K. and L.S.; resources, J.L.; writing—original draft preparation, J.L.; writing—review and editing, V.K., L.S., A.L. and K.D.; supervision, V.K.; project administration, V.K., L.S. and A.L.; funding acquisition, V.K., L.S. and A.L. All authors have read and agreed to the published version of the manuscript.

Funding: This research was funded by the Governmental Program, Grant № FSWW-2023-0005.

Data Availability Statement: The raw/processed data required to reproduce these findings cannot be shared at this time as the data also forms part of an ongoing study.

Acknowledgments: This research was supported by TPU development program.

Conflicts of Interest: The authors declare that they have no known competing financial interests or personal relationships that could have appeared to influence the work reported in this paper.

References

1. Wu, R.; Chen, Y.; Zhou, L.; Wei, X. Research progress and properties of Mg-based hydrogen storage alloy materials. *Pop. Sci. Technol.* **2016**, *18*, 49–52. (In Chinese) [[CrossRef](#)]
2. Mohtadi, R.; Orimo, S.-I. The renaissance of hydrides as energy materials. *Nat. Rev. Mater.* **2017**, *2*, 16091. [[CrossRef](#)]

3. Baran, A.; Polański, M. Magnesium-Based Materials for Hydrogen Storage—A Scope Review. *Materials* **2020**, *13*, 3993. [[CrossRef](#)] [[PubMed](#)]
4. Liao, Q. Reactive Ball-milling Synthesis of Mg-based Hydrogen Storage Materials. Master's Thesis, Chongqing University, Chongqing, China, 2017. (In Chinese).
5. Sadhasivam, T.; Kim, H.-T.; Jung, S.; Roh, S.-H.; Park, J.-H.; Jung, H.-Y. Dimensional effects of nanostructured Mg/MgH₂ for hydrogen storage applications: A review. *Renew. Sustain. Energy Rev.* **2017**, *72*, 523–534. [[CrossRef](#)]
6. Sirsch, P.; Che, F.N.; Titah, J.T.; McGrady, G.S. Hydride-Hydride Bonding Interactions in the Hydrogen Storage Materials AlH₃, MgH₂, and NaAlH₄. *Chem. Eur. J.* **2012**, *18*, 9476–9480. [[CrossRef](#)] [[PubMed](#)]
7. Rusman, N.; Dahari, M. A review on the current progress of metal hydrides material for solid-state hydrogen storage applications. *Int. J. Hydrog. Energy* **2016**, *41*, 12108–12126. [[CrossRef](#)]
8. Qin, T. Study on Nano-synthesis and Hydrogen Absorption/Desorption Properties of Mg-based Hydrogen Storage Materials with High Capacity. Master's Thesis, Zhejiang University, Hangzhou, China, 2016. (In Chinese).
9. Ding, X.; Chen, R.; Chen, X.; Cao, W.; Ding, H.; Su, Y.; Guo, J. De-/hydrogenation mechanism of Mg-based hydrogen storage alloys and their microstructure and property control. *Chin. J. Nat.* **2020**, *42*, 179–186. [[CrossRef](#)]
10. Ye, J. First-principles Investigation on the Hydrogen Storage Mechanism over Mg(10-13) Surface. Master's Thesis, Guangdong University of Technology, Guangdong, China, 2018. (In Chinese).
11. Züttel, A. Materials for hydrogen storage. *Mater. Today* **2003**, *6*, 24–33. [[CrossRef](#)]
12. Han, D.J.; Bang, K.R.; Cho, H.; Cho, E.S. Effect of carbon nanoscaffolds on hydrogen storage performance of magnesium hydride. *Korean J. Chem. Eng.* **2020**, *37*, 1306–1316. [[CrossRef](#)]
13. Zykov, B.M.; Krasnenkova, T.M.; Lazba, B.A.; Markoliya, A.I. Optimization of Magnesium-Based Solid-State Hydrogen Storage for Vehicles. *Tech. Phys.* **2020**, *65*, 946–956. [[CrossRef](#)]
14. Yang, J.; Hirano, S. Improving the Hydrogen Reaction Kinetics of Complex Hydrides. *Adv. Mater.* **2009**, *21*, 3023–3028. [[CrossRef](#)]
15. Allendorf, M.D.; Hulvey, Z.; Gennett, T.; Ahmed, A.; Autrey, T.; Camp, J.; Cho, E.S.; Furukawa, H.; Haranczyk, M.; Head-Gordon, M.; et al. An assessment of strategies for the development of solid-state adsorbents for vehicular hydrogen storage. *Energy Environ. Sci.* **2018**, *11*, 2784–2812. [[CrossRef](#)]
16. Lai, Q.; Paskevicius, M.; Sheppard, D.A.; Buckley, C.E.; Thornton, A.W.; Hill, M.R.; Gu, Q.; Mao, J.; Huang, Z.; Liu, H.K.; et al. Hydrogen Storage Materials for Mobile and Stationary Applications: Current State of the Art. *ChemSuschem* **2015**, *8*, 2789–2825. [[CrossRef](#)] [[PubMed](#)]
17. Lyu, J.; Kudiiarov, V.; Lider, A. An Overview of the Recent Progress in Modifications of Carbon Nanotubes for Hydrogen Adsorption. *Nanomaterials* **2020**, *10*, 255. [[CrossRef](#)]
18. Mojica-Sánchez, J.P.; Zarate-López, T.I.; Flores-Álvarez, J.M.; Reyes-Gómez, J.; Pineda-Urbina, K.; Gómez-Sandoval, Z. Magnesium oxide clusters as promising candidates for hydrogen storage. *Phys. Chem. Chem. Phys.* **2019**, *21*, 23102–23110. [[CrossRef](#)] [[PubMed](#)]
19. Viswanathan, B. Hydrogen storage. In *Energy Sources: Fundamentals of Chemical Conversion Processes and Applications*; Elsevier: Amsterdam, The Netherlands, 2017; pp. 185–212.
20. Sun, Y.; Shen, C.; Lai, Q.; Liu, W.; Wang, D.-W.; Aguey-Zinsou, K.-F. Tailoring magnesium based materials for hydrogen storage through synthesis: Current state of the art. *Energy Storage Mater.* **2018**, *10*, 168–198. [[CrossRef](#)]
21. Zhu, Q.-L.; Xu, Q. Liquid organic and inorganic chemical hydrides for high-capacity hydrogen storage. *Energy Environ. Sci.* **2014**, *8*, 478–512. [[CrossRef](#)]
22. Abdellaoui, M.; Lakhal, M.; Bhihi, M.; El Khatabi, M.; Benyoussef, A.; El Kenz, A.; Loulidi, M. First principle study of hydrogen storage in doubly substituted Mg based hydrides Mg₅MH₁₂ (M = B, Li) and Mg₄BLiH₁₂. *Int. J. Hydrog. Energy* **2016**, *41*, 20908–20913. [[CrossRef](#)]
23. Ouyang, L.; Liu, F.; Wang, H.; Liu, J.; Yang, X.-S.; Sun, L.; Zhu, M. Magnesium-based hydrogen storage compounds: A review. *J. Alloy. Compd.* **2020**, *832*, 154865. [[CrossRef](#)]
24. Vajeeston, P.; Ravindran, P.; Fjellvåg, H. Theoretical investigations on low energy surfaces and nanowires of MgH₂. *Nanotechnology* **2008**, *19*, 275704. [[CrossRef](#)] [[PubMed](#)]
25. Er, S.; Tiwari, D.; de Wijs, G.A.; Brocks, G. Tunable hydrogen storage in magnesium–transition metal compounds: First-principles calculations. *Phys. Rev. B* **2009**, *79*, 024105. [[CrossRef](#)]
26. El Khatabi, M.; Bhihi, M.; Naji, S.; Labrim, H.; Benyoussef, A.; El Kenz, A.; Loulidi, M. Study of doping effects with 3d and 4d-transition metals on the hydrogen storage properties of MgH₂. *Int. J. Hydrog. Energy* **2016**, *41*, 4712–4718. [[CrossRef](#)]
27. Sun, G.; Li, Y.; Zhao, X.; Wu, J.; Wang, L.; Mi, Y. First-principles investigation of the effects of Ni and Y co-doped on destabilized MgH₂. *RSC Adv.* **2016**, *6*, 23110–23116. [[CrossRef](#)]
28. Mamula, B.P.; Novaković, J.G.; Radisavljević, I.; Ivanović, N.; Novaković, N. Electronic structure and charge distribution topology of MgH₂ doped with 3d transition metals. *Int. J. Hydrog. Energy* **2014**, *39*, 5874–5887. [[CrossRef](#)]
29. Zhou, D.; Peng, P.; Liu, J. First-principles calculation of dehydrogenating properties of MgH₂-V systems. *Sci. China Technol. Sci.* **2006**, *49*, 129–136. [[CrossRef](#)]
30. Zhang, J.; Yan, S.; Yu, L.; Zhou, X.; Zhou, T.; Peng, P. Enhanced hydrogen storage properties and mechanisms of magnesium hydride modified by transition metal dissolved magnesium oxides. *Int. J. Hydrog. Energy* **2018**, *43*, 21864–21873. [[CrossRef](#)]

31. Yartys, V.; Lototsky, M.; Akiba, E.; Albert, R.; Antonov, V.; Ares, J.; Baricco, M.; Bourgeois, N.; Buckley, C.; von Colbe, J.B.; et al. Magnesium based materials for hydrogen based energy storage: Past, present and future. *Int. J. Hydrog. Energy* **2019**, *44*, 7809–7859. [\[CrossRef\]](#)
32. Wang, Z.; Zhang, X.; Ren, Z.; Liu, Y.; Hu, J.; Li, H.; Gao, M.; Pan, H.; Liu, Y. In situ formed ultrafine NbTi nanocrystals from a NbTiC solid-solution MXene for hydrogen storage in MgH₂. *J. Mater. Chem. A* **2019**, *7*, 14244–14252. [\[CrossRef\]](#)
33. Crivello, J.-C.; Dam, B.; Denys, R.V.; Dornheim, M.; Grant, D.M.; Huot, J.; Jensen, T.R.; De Jongh, P.; Latroche, M.; Milanese, C.; et al. Review of magnesium hydride-based materials: Development and optimisation. *Appl. Phys. A* **2016**, *122*, 1–20. [\[CrossRef\]](#)
34. Zhang, J.; Li, Z.; Wu, Y.; Guo, X.; Ye, J.; Yuan, B.; Wang, S.; Jiang, L. Recent advances on the thermal destabilization of Mg-based hydrogen storage materials. *RSC Adv.* **2019**, *9*, 408–428. [\[CrossRef\]](#)
35. Bhihi, M.; El Khatabi, M.; Lakhal, M.; Naji, S.; Labrim, H.; Benyoussef, A.; El Kenz, A.; Loulidi, M. First principle study of hydrogen storage in doubly substituted Mg based hydrides. *Int. J. Hydrog. Energy* **2015**, *40*, 8356–8361. [\[CrossRef\]](#)
36. Wu, X.-X.; Hu, W. First-principles study of Pd single-atom catalysis to hydrogen desorption reactions on MgH₂(110) surface. *Chin. J. Chem. Phys.* **2019**, *32*, 319–326. [\[CrossRef\]](#)
37. Rizo-Acosta, P.; Cuevas, F.; Latroche, M. Hydrides of early transition metals as catalysts and grain growth inhibitors for enhanced reversible hydrogen storage in nanostructured magnesium. *J. Mater. Chem. A* **2019**, *7*, 23064–23075. [\[CrossRef\]](#)
38. Xie, X.; Chen, M.; Hu, M.; Wang, B.; Yu, R.; Liu, T. Recent advances in magnesium-based hydrogen storage materials with multiple catalysts. *Int. J. Hydrog. Energy* **2019**, *44*, 10694–10712. [\[CrossRef\]](#)
39. Cheng, F.; Tao, Z.; Liang, J.; Chen, J. Efficient hydrogen storage with the combination of lightweight Mg/MgH₂ and nanostructures. *Chem. Commun.* **2012**, *48*, 7334–7343. [\[CrossRef\]](#) [\[PubMed\]](#)
40. Han, Z.; Chen, H.; Zhou, S. Dissociation and diffusion of hydrogen on defect-free and vacancy defective Mg (0001) surfaces: A density functional theory study. *Appl. Surf. Sci.* **2017**, *394*, 371–377. [\[CrossRef\]](#)
41. Jian, Z.; Dianwu, Z.; Yani, H.; Ping, P.; Jinshui, L. Study on H₂ Adsorption and Dissociation Properties on Mg(0001) Surface. *Rare Met. Mater. Eng.* **2009**, *38*, 1518–1525. [\[CrossRef\]](#)
42. Klyukin, K.; Shelyapina, M.G.; Fruchart, D. DFT calculations of hydrogen diffusion and phase transformations in magnesium. *J. Alloy. Compd.* **2015**, *644*, 371–377. [\[CrossRef\]](#)
43. Zhang, L.; Chen, L.; Fan, X.; Xiao, X.; Zheng, J.; Huang, X. Enhanced hydrogen storage properties of MgH₂ with numerous hydrogen diffusion channels provided by Na₂Ti₃O₇ nanotubes. *J. Mater. Chem. A* **2017**, *5*, 6178–6185. [\[CrossRef\]](#)
44. Zhang, Y.; Xiao, X.; Luo, B.; Huang, X.; Liu, M.; Chen, L. Synergistic Effect of LiBH₄ and LiAlH₄ Additives on Improved Hydrogen Storage Properties of Unexpected High Capacity Magnesium Hydride. *J. Phys. Chem. C* **2018**, *122*, 2528–2538. [\[CrossRef\]](#)
45. Chen, G.; Zhang, Y.; Chen, J.; Guo, X.; Zhu, Y.; Li, L. Enhancing hydrogen storage performances of MgH₂ by Ni nano-particles over mesoporous carbon CMK-3. *Nanotechnology* **2018**, *29*, 265705. [\[CrossRef\]](#)
46. Jangir, M.; Jain, A.; Agarwal, S.; Zhang, T.; Kumar, S.; Selvaraj, S.; Ichikawa, T.; Jain, I. The enhanced de/re-hydrogenation performance of MgH₂ with TiH₂ additive. *Int. J. Energy Res.* **2018**, *42*, 1139–1147. [\[CrossRef\]](#)
47. Zhang, Q.; Huang, Y.; Xu, L.; Zang, L.; Guo, H.; Jiao, L.; Yuan, H.; Wang, Y. Highly Dispersed MgH₂ Nanoparticle–Graphene Nanosheet Composites for Hydrogen Storage. *ACS Appl. Nano Mater.* **2019**, *2*, 3828–3835. [\[CrossRef\]](#)
48. Vegge, T. Locating the rate-limiting step for the interaction of hydrogen with Mg(0001) using density-functional theory calculations and rate theory. *Phys. Rev. B* **2004**, *70*, 035412. [\[CrossRef\]](#)
49. Zhang, L.; Wang, K.; Liu, Y.; Zhang, X.; Hu, J.; Gao, M.; Pan, H. Highly active multivalent multielement catalysts derived from hierarchical porous TiNb₂O₇ nanospheres for the reversible hydrogen storage of MgH₂. *Nano Res.* **2020**, *14*, 148–156. [\[CrossRef\]](#)
50. Webb, C. A review of catalyst-enhanced magnesium hydride as a hydrogen storage material. *J. Phys. Chem. Solids* **2015**, *84*, 96–106. [\[CrossRef\]](#)
51. Zhang, X.; Shen, Z.; Jian, N.; Hu, J.; Du, F.; Yao, J.; Gao, M.; Liu, Y.; Pan, H. A novel complex oxide TiVO_{3.5} as a highly active catalytic precursor for improving the hydrogen storage properties of MgH₂. *Int. J. Hydrog. Energy* **2018**, *43*, 23327–23335. [\[CrossRef\]](#)
52. Friedrichs, O.; Sánchez-López, J.; López-Cartes, C.; Dornheim, M.; Klassen, T.; Bormann, R.; Fernández, A. Chemical and microstructural study of the oxygen passivation behaviour of nanocrystalline Mg and MgH₂. *Appl. Surf. Sci.* **2006**, *252*, 2334–2345. [\[CrossRef\]](#)
53. Kumar, S.; Singh, V.; Cassidy, C.; Pursell, C.; Nivargi, C.; Clemens, B.; Sowwan, M. Hydrogenation of Mg nanofilms catalyzed by size-selected Pd nanoparticles: Observation of localized MgH₂ nanodomains. *J. Catal.* **2016**, *337*, 14–25. [\[CrossRef\]](#)
54. Yan, S. Study on Modifying Mechanism of Magnesium-Based Oxides on Hydrogen Storage Properties of Magnesium Hydride. Master's Thesis, Changsha University of Science & Technology, Hunan, China, 2019. (In Chinese).
55. Jeon, K.-J.; Moon, H.R.; Ruminski, A.M.; Jiang, B.; Kisielowski, C.; Bardhan, R.; Urban, J.J. Air-stable magnesium nanocomposites provide rapid and high-capacity hydrogen storage without using heavy-metal catalysts. *Nat. Mater.* **2011**, *10*, 286–290. [\[CrossRef\]](#)
56. Liu, H.; Sun, P.; Bowman, R.C.; Fang, Z.Z.; Liu, Y.; Zhou, C. Effect of air exposure on hydrogen storage properties of catalyzed magnesium hydride. *J. Power Sources* **2020**, *454*, 227936. [\[CrossRef\]](#)
57. Ostenfeld, C.W.; Chorkendorff, I. Effect of oxygen on the hydrogenation properties of magnesium films. *Surf. Sci.* **2006**, *600*, 1363–1368. [\[CrossRef\]](#)
58. Han, Z.; Yeboah, M.L.; Jiang, R.; Li, X.; Zhou, S. Hybrid activation mechanism of thermal annealing for hydrogen storage of magnesium based on experimental evidence and theoretical validation. *Appl. Surf. Sci.* **2020**, *504*, 144491. [\[CrossRef\]](#)

59. El-Eskandarany, M.; Saeed, M.; Al-Nasrallah, E.; Al-Ajmi, F.; Banyan, M. Effect of LaNi₃ Amorphous Alloy Nanopowders on the Performance and Hydrogen Storage Properties of MgH₂. *Energies* **2019**, *12*, 1005. [CrossRef]
60. Camirand, C.P. Measurement of thermal conductivity by differential scanning calorimetry. *Thermochim. Acta* **2004**, *417*, 1–4. [CrossRef]
61. Nordlander, P.; Holloway, S.; Nørskov, J. Hydrogen adsorption on metal surfaces. *Surf. Sci.* **1984**, *136*, 59–81. [CrossRef]
62. Hammer, B.; Nørskov, J. Electronic factors determining the reactivity of metal surfaces. *Surf. Sci.* **1995**, *343*, 211–220. [CrossRef]
63. Gabis, I.; Chernov, I.; Voyt, A. Decomposition kinetics of metal hydrides: Experiments and modeling. *J. Alloy. Compd.* **2013**, *580*, S243–S246. [CrossRef]
64. Wu, X. First-principles studies of magnesium hydride as a hydrogen storage material. Ph.D. Thesis, University of Science and Technology of China, Anhui, China, 2017. (In Chinese).
65. El Khatabi, M.; Naji, S.; Bhihi, M.; Benyoussef, A.; El Kenz, A.; Loulidi, M. Effects of double substitution on MgH₂ hydrogen storage properties: An Ab initio study. *J. Alloy. Compd.* **2018**, *743*, 666–671. [CrossRef]
66. Maark, T.A.; Hussain, T.; Ahuja, R. Structural, electronic and thermodynamic properties of Al- and Si-doped α -, γ -, and β -MgH₂: Density functional and hybrid density functional calculations. *Int. J. Hydrog. Energy* **2012**, *37*, 9112–9122. [CrossRef]
67. Vajeeston, P.; Ravindran, P.; Kjekshus, A.; Fjellvåg, H. Pressure-Induced Structural Transitions in MgH₂. *Phys. Rev. Lett.* **2002**, *89*, 175506. [CrossRef] [PubMed]
68. Zeng, X.Q.; Cheng, L.F.; Zou, J.X.; Ding, W.J.; Tian, H.Y.; Buckley, C. Influence of 3d transition metals on the stability and electronic structure of MgH₂. *J. Appl. Phys.* **2012**, *111*, 093720. [CrossRef]
69. Spatz, P.; Aebischer, H.A.; Krozer, A.; Schlapbach, L. The Diffusion of H in Mg and the Nucleation and Growth of MgH₂ in Thin Films. *Z. Phys. Chem.* **1993**, *181*, 393–397. [CrossRef]
70. Hao, S.; Sholl, D.S. Hydrogen diffusion in MgH₂ and NaMgH₃ via concerted motions of charged defects. *Appl. Phys. Lett.* **2008**, *93*, 251901. [CrossRef]
71. Nogita, K.; Tran, X.Q.; Yamamoto, T.; Tanaka, E.; McDonald, S.D.; Gourlay, C.M.; Yasuda, K.; Matsumura, S. Evidence of the hydrogen release mechanism in bulk MgH₂. *Sci. Rep.* **2015**, *5*, 8450. [CrossRef] [PubMed]
72. Čermák, J.; Král, L. Hydrogen diffusion in Mg–H and Mg–Ni–H alloys. *Acta Mater.* **2008**, *56*, 2677–2686. [CrossRef]
73. Kitagawa, Y.; Tanabe, K. Development of a kinetic model of hydrogen absorption and desorption in magnesium and analysis of the rate-determining step. *Chem. Phys. Lett.* **2018**, *699*, 132–138. [CrossRef]
74. Tien, H.-Y.; Tanniru, M.; Wu, C.-Y.; Ebrahimi, F. Effect of hydride nucleation rate on the hydrogen capacity of Mg. *Int. J. Hydrog. Energy* **2009**, *34*, 6343–6349. [CrossRef]
75. Li, J.; Zhou, C.; Fang, Z.Z.; Bowman, R.C., Jr.; Lu, J.; Ren, C. Isothermal hydrogenation kinetics of ball-milled nano-catalyzed magnesium hydride. *Materialia* **2019**, *5*, 100227. [CrossRef]
76. Yang, J.; Sudik, A.; Wolverton, C.; Siegel, D.J. High capacity hydrogen storage materials: Attributes for automotive applications and techniques for materials discovery. *Chem. Soc. Rev.* **2009**, *39*, 656–675. [CrossRef]
77. Wang, Z.; Ren, Z.; Jian, N.; Gao, M.; Hu, J.; Du, F.; Pan, H.; Liu, Y. Vanadium oxide nanoparticles supported on cubic carbon nanoboxes as highly active catalyst precursors for hydrogen storage in MgH₂. *J. Mater. Chem. A* **2018**, *6*, 16177–16185. [CrossRef]
78. Rajabpour, F.; Raygan, S.; Abdizadeh, H. The synergistic effect of catalysts on hydrogen desorption properties of MgH₂–TiO₂–NiO nanocomposite. *Mater. Renew. Sustain. Energy* **2016**, *5*, 20. [CrossRef]
79. Ismail, M. Influence of different amounts of FeCl₃ on decomposition and hydrogen sorption kinetics of MgH₂. *Int. J. Hydrog. Energy* **2014**, *39*, 2567–2574. [CrossRef]
80. Zhang, J.; Qu, H.; Yan, S.; Yin, L.R.; Zhou, D. Dehydrogenation properties and mechanisms of MgH₂–NiCl₂ and MgH₂–NiCl₂–graphene hydrogen storage composites. *Met. Mater. Int.* **2017**, *23*, 831–837. [CrossRef]
81. Korablov, D.; Nielsen, T.K.; Besenbacher, F.; Jensen, T.R. Mechanism and kinetics of early transition metal hydrides, oxides, and chlorides to enhance hydrogen release and uptake properties of MgH₂. *Powder Diffr.* **2015**, *30*, S9–S15. [CrossRef]
82. Plerdsranoy, P.; Thiangviriyi, S.; Dansirima, P.; Thongtan, P.; Kaewsuwan, D.; Chanlek, N.; Utke, R. Synergistic effects of transition metal halides and activated carbon nanofibers on kinetics and reversibility of MgH₂. *J. Phys. Chem. Solids* **2018**, *124*, 81–88. [CrossRef]
83. Peng, D.; Ding, Z.; Zhang, L.; Fu, Y.; Wang, J.; Li, Y.; Han, S. Remarkable hydrogen storage properties and mechanisms of the shell–core MgH₂@carbon aerogel microspheres. *Int. J. Hydrog. Energy* **2018**, *43*, 3731–3740. [CrossRef]
84. Chawla, K.; Yadav, D.K.; Sharda, P.; Lal, N.; Sharma, S.; Lal, C. Hydrogenation properties of MgH₂–x wt% AC (x = 0, 5, 10, 15) nanocomposites. *Int. J. Hydrog. Energy* **2020**, *45*, 23971–23976. [CrossRef]
85. Zhang, L.; Lu, X.; Ji, L.; Yan, N.; Sun, Z.; Zhu, X. Catalytic Effect of Facile Synthesized TiH_{1.971} Nanoparticles on the Hydrogen Storage Properties of MgH₂. *Nanomaterials* **2019**, *9*, 1370. [CrossRef]
86. Chen, M.; Xiao, X.; Zhang, M.; Mao, J.; Zheng, J.; Liu, M.; Wang, X.; Chen, L. Insights into 2D graphene-like TiO₂ (B) nanosheets as highly efficient catalyst for improved low-temperature hydrogen storage properties of MgH₂. *Mater. Today Energy* **2020**, *16*, 100411. [CrossRef]
87. Cermak, J.; Kral, L.; Roupova, P. Significantly decreased stability of MgH₂ in the Mg–In–C alloy system: Long-period-stacking-ordering as a new way how to improve performance of hydrogen storage alloys. *Renew. Energy* **2020**, *150*, 204–212. [CrossRef]
88. Yong, H.; Guo, S.; Yuan, Z.; Qi, Y.; Zhao, D.; Zhang, Y. Improved hydrogen storage kinetics and thermodynamics of RE–Mg-based alloy by co-doping Ce–Y. *Int. J. Hydrog. Energy* **2019**, *44*, 16765–16776. [CrossRef]

89. Yang, T.; Li, Q.; Liu, N.; Liang, C.; Yin, F.; Zhang, Y. Improved hydrogen absorption and desorption kinetics of magnesium-based alloy via addition of yttrium. *J. Power Sources* **2018**, *378*, 636–645. [\[CrossRef\]](#)
90. Tan, Z.; Ouyang, L.; Liu, J.; Wang, H.; Shao, H.; Zhu, M. Hydrogen generation by hydrolysis of Mg-Mg₂Si composite and enhanced kinetics performance from introducing of MgCl₂ and Si. *Int. J. Hydrog. Energy* **2018**, *43*, 2903–2912. [\[CrossRef\]](#)
91. Wang, Y.; Zhou, Z.; Zhou, W.; Xu, L.; Guo, J.; Lan, Z. Effects of in-situ formed Mg₂Si phase on the hydrogen storage properties of Mg Li solid solution alloys. *Mater. Des.* **2016**, *111*, 248–252. [\[CrossRef\]](#)
92. Zhong, H.; Wang, H.; Liu, J.; Sun, D.; Zhu, M. Altered desorption enthalpy of MgH₂ by the reversible formation of Mg(In) solid solution. *Scr. Mater.* **2011**, *65*, 285–287. [\[CrossRef\]](#)
93. Zhou, C.; Fang, Z.Z.; Lu, J.; Zhang, X. Thermodynamic and Kinetic Destabilization of Magnesium Hydride Using Mg–In Solid Solution Alloys. *J. Am. Chem. Soc.* **2013**, *135*, 10982–10985. [\[CrossRef\]](#) [\[PubMed\]](#)
94. Ouyang, L.; Cao, Z.; Wang, H.; Liu, J.; Sun, D.; Zhang, Q.; Zhu, M. Dual-tuning effect of In on the thermodynamic and kinetic properties of Mg₂Ni dehydrogenation. *Int. J. Hydrog. Energy* **2013**, *38*, 8881–8887. [\[CrossRef\]](#)
95. Lu, Y.; Wang, H.; Liu, J.; Ouyang, L.; Zhu, M. Destabilizing the dehydrogenating thermodynamics of MgH₂ by reversible intermetallics formation in Mg–Ag–Zn ternary alloys. *J. Power Sources* **2018**, *396*, 796–802. [\[CrossRef\]](#)
96. Lu, Y.; Wang, H.; Liu, J.; Li, Z.; Ouyang, L.; Zhu, M. Hydrogen-Induced Reversible Phase Transformations and Hydrogen Storage Properties of Mg–Ag–Al Ternary Alloys. *J. Phys. Chem. C* **2016**, *120*, 27117–27127. [\[CrossRef\]](#)
97. Rabkin, E.; Skripnyuk, V.; Estrin, Y. Ultrafine-Grained Magnesium Alloys for Hydrogen Storage Obtained by Severe Plastic Deformation. *Front. Mater.* **2019**, *6*, 240. [\[CrossRef\]](#)
98. Norberg, N.S.; Arthur, T.S.; Fredrick, S.J.; Prieto, A.L. Size-Dependent Hydrogen Storage Properties of Mg Nanocrystals Prepared from Solution. *J. Am. Chem. Soc.* **2011**, *133*, 10679–10681. [\[CrossRef\]](#) [\[PubMed\]](#)
99. Au, Y.S.; Obbink, M.K.; Srinivasan, S.; Magusin, P.C.M.M.; de Jong, K.P.; de Jongh, P.E. The Size Dependence of Hydrogen Mobility and Sorption Kinetics for Carbon-Supported MgH₂ Particles. *Adv. Funct. Mater.* **2014**, *24*, 3604–3611. [\[CrossRef\]](#)
100. Wang, H.; Zhang, S.; Liu, J.; Ouyang, L.; Zhu, M. Enhanced dehydrogenation of nanoscale MgH₂ confined by ordered mesoporous silica. *Mater. Chem. Phys.* **2012**, *136*, 146–150. [\[CrossRef\]](#)
101. Zhang, L.; Cai, Z.; Yao, Z.; Ji, L.; Sun, Z.; Yan, N.; Zhang, B.; Xiao, B.; Du, J.; Zhu, X.; et al. A striking catalytic effect of facile synthesized ZrMn₂ nanoparticles on the de/rehydrogenation properties of MgH₂. *J. Mater. Chem. A* **2019**, *7*, 5626–5634. [\[CrossRef\]](#)
102. Cui, J.; Liu, J.; Wang, H.; Ouyang, L.; Sun, D.; Zhu, M.; Yao, X. Mg–TM (TM: Ti, Nb, V, Co, Mo or Ni) core-shell like nanostructures: Synthesis, hydrogen storage performance and catalytic mechanism. *J. Mater. Chem. A* **2014**, *2*, 9645–9655. [\[CrossRef\]](#)
103. Zhou, C.; Fang, Z.Z.; Ren, C.; Li, J.; Lu, J. Effect of Ti Intermetallic Catalysts on Hydrogen Storage Properties of Magnesium Hydride. *J. Phys. Chem. C* **2013**, *117*, 12973–12980. [\[CrossRef\]](#)
104. Yao, X.; Wu, C.; Du, A.; Zou, J.; Zhu, Z.; Wang, P.; Cheng, H.; Smith, S.; Lu, G. Metallic and Carbon Nanotube-Catalyzed Coupling of Hydrogenation in Magnesium. *J. Am. Chem. Soc.* **2007**, *129*, 15650–15654. [\[CrossRef\]](#)
105. Wang, Y.; Liu, G.; An, C.; Li, L.; Qiu, F.; Jiao, L.; Yuan, H. Bimetallic NiCo Functional Graphene: An Efficient Catalyst for Hydrogen-Storage Properties of MgH₂. *Chem.–Asian J.* **2014**, *9*, 2576–2583. [\[CrossRef\]](#)
106. Galey, B.; Auroux, A.; Sabo-Etienne, S.; Grellier, M.; Postole, G. Enhancing hydrogen storage properties of the Mg/MgH₂ system by the addition of bis(tricyclohexylphosphine)nickel(II) dichloride. *Int. J. Hydrog. Energy* **2019**, *44*, 11939–11952. [\[CrossRef\]](#)
107. Galey, B.; Auroux, A.; Sabo-Etienne, S.; Dhaher, S.; Grellier, M.; Postole, G. Improved hydrogen storage properties of Mg/MgH₂ thanks to the addition of nickel hydride complex precursors. *Int. J. Hydrog. Energy* **2019**, *44*, 28848–28862. [\[CrossRef\]](#)
108. Cheng, H.; Chen, G.; Zhang, Y.; Zhu, Y.; Li, L. Boosting low-temperature de/re-hydrogenation performances of MgH₂ with Pd–Ni bimetallic nanoparticles supported by mesoporous carbon. *Int. J. Hydrog. Energy* **2019**, *44*, 10777–10787. [\[CrossRef\]](#)
109. Valentoni, A.; Mulas, G.; Enzo, S.; Garroni, S. Remarkable hydrogen storage properties of MgH₂ doped with VNbO₅. *Phys. Chem. Chem. Phys.* **2018**, *20*, 4100–4108. [\[CrossRef\]](#) [\[PubMed\]](#)
110. Zhang, J.; Shan, J.; Li, P.; Zhai, F.; Wan, Q.; Liu, Z.; Qu, X. Dehydrogenation mechanism of ball-milled MgH₂ doped with ferrites (CoFe₂O₄, ZnFe₂O₄, MnFe₂O₄ and Mn_{0.5}Zn_{0.5}Fe₂O₄) nanoparticles. *J. Alloy. Compd.* **2015**, *643*, 174–180. [\[CrossRef\]](#)
111. Zhang, W.; Xu, G.; Cheng, Y.; Chen, L.; Huo, Q.; Liu, S. Improved hydrogen storage properties of MgH₂ by the addition of FeS₂ micro-spheres. *Dalton Trans.* **2018**, *47*, 5217–5225. [\[CrossRef\]](#)
112. Khan, D.; Zou, J.; Zeng, X.; Ding, W. Hydrogen storage properties of nanocrystalline Mg₂Ni prepared from compressed 2MgH₂Ni powder. *Int. J. Hydrog. Energy* **2018**, *43*, 22391–22400. [\[CrossRef\]](#)
113. Wronski, Z.; Carpenter, G.; Czujko, T.; Varin, R. A new nanonickel catalyst for hydrogen storage in solid-state magnesium hydrides. *Int. J. Hydrog. Energy* **2011**, *36*, 1159–1166. [\[CrossRef\]](#)
114. Liu, Y.; Zou, J.; Zeng, X.; Ding, W. A co-precipitated Mg–Ti nano-composite with high capacity and rapid hydrogen absorption kinetics at room temperature. *RSC Adv.* **2014**, *4*, 42764–42771. [\[CrossRef\]](#)
115. Li, Q.; Li, Y.; Liu, B.; Lu, X.; Zhang, T.; Gu, Q. The cycling stability of the in situ formed Mg-based nanocomposite catalyzed by YH₂. *J. Mater. Chem. A* **2017**, *5*, 17532–17543. [\[CrossRef\]](#)
116. AlMatrouk, H.S.; Chihai, V. Theoretical study on the effects of the magnesium hydride doping with cobalt and nickel on the hydrogen release. *Int. J. Hydrog. Energy* **2015**, *40*, 5319–5325. [\[CrossRef\]](#)
117. Lu, C.; Zou, J.; Zeng, X.; Ding, W. Hydrogen storage properties of core-shell structured Mg@TM (TM = Co, V) composites. *Int. J. Hydrog. Energy* **2017**, *42*, 15246–15255. [\[CrossRef\]](#)

118. Zou, J.; Guo, H.; Zeng, X.; Zhou, S.; Chen, X.; Ding, W. Hydrogen storage properties of Mg–TM–La (TM = Ti, Fe, Ni) ternary composite powders prepared through arc plasma method. *Int. J. Hydrog. Energy* **2013**, *38*, 8852–8862. [\[CrossRef\]](#)
119. Gattia, D.M.; Jangir, M.; Jain, I. Study on nanostructured MgH₂ with Fe and its oxides for hydrogen storage applications. *J. Alloy. Compd.* **2019**, *801*, 188–191. [\[CrossRef\]](#)
120. El-Eskandarany, M.S.; Al-Ajmi, F.; Banyan, M.; Al-Duweesh, A. Synergetic effect of reactive ball milling and cold pressing on enhancing the hydrogen storage behavior of nanocomposite MgH₂/10 wt% TiMn₂ binary system. *Int. J. Hydrog. Energy* **2019**, *44*, 26428–26443. [\[CrossRef\]](#)
121. Xie, L.; Li, J.; Zhang, T.; Song, L. Air-stable MgH₂ – CeO₂ composite with facilitated de/hydrogenation kinetics synthesized by high energy ball milling. *Mater. Charact.* **2017**, *133*, 94–101. [\[CrossRef\]](#)
122. Chakrabarti, S.; Biswas, K. Effect on de-hydrogenation efficiency on doping of rare earth elements (Pr, Nd, Gd, Dy) in MgH₂—A density functional theory study. *Int. J. Hydrog. Energy* **2017**, *42*, 1012–1017. [\[CrossRef\]](#)
123. Zou, J.; Zeng, X.; Ying, Y.; Chen, X.; Guo, H.; Zhou, S.; Ding, W. Study on the hydrogen storage properties of core–shell structured Mg–RE (RE = Nd, Gd, Er) nano-composites synthesized through arc plasma method. *Int. J. Hydrog. Energy* **2013**, *38*, 2337–2346. [\[CrossRef\]](#)
124. Chakrabarti, S.; Biswas, K. Effect on specific capacity and de-hydrogenation efficiency in doped-MgH₂. *Int. J. Hydrog. Energy* **2017**, *42*, 327–339. [\[CrossRef\]](#)
125. Slater, J.C. Atomic Radii in Crystals. *J. Chem. Phys.* **1964**, *41*, 3199–3204. [\[CrossRef\]](#)
126. Meija, J.; Coplen, T.B.; Berglund, M.; Brand, W.A.; de Bièvre, P.; Gröning, M.; Holden, N.E.; Irrgeher, J.; Loss, R.D.; Walczyk, T.; et al. Atomic weights of the elements 2013 (IUPAC Technical Report). *Pure Appl. Chem.* **2016**, *88*, 265–291. [\[CrossRef\]](#)
127. Urretavizcaya, G.; Chávez, A.C.S.; Castro, F.J. Hydrogen absorption and desorption in the Mg–Ag system. *J. Alloy. Compd.* **2014**, *611*, 202–209. [\[CrossRef\]](#)
128. Emami, H.; Edalati, K.; Staykov, A.; Hongo, T.; Iwaoka, H.; Horita, Z.; Akiba, E. Solid-state reactions and hydrogen storage in magnesium mixed with various elements by high-pressure torsion: Experiments and first-principles calculations. *RSC Adv.* **2016**, *6*, 11665–11674. [\[CrossRef\]](#)
129. Crivello, J.-C.; Denys, R.V.; Dornheim, M.; Felderhoff, M.; Grant, D.M.; Huot, J.; Jensen, T.R.; De Jongh, P.; Latroche, M.; Walker, G.S.; et al. Mg-based compounds for hydrogen and energy storage. *Appl. Phys. A* **2016**, *122*, 1–17. [\[CrossRef\]](#)
130. Skripnyuk, V.; Rabkin, E. Mg₃Cd: A model alloy for studying the destabilization of magnesium hydride. *Int. J. Hydrog. Energy* **2012**, *37*, 10724–10732. [\[CrossRef\]](#)
131. Moser, Z.; Gasior, W.; Wypartowicz, J.; Zabdyr, L. The Cd–Mg (Cadmium–Magnesium) system. *Bull. Alloy. Phase Diagr.* **1984**, *5*, 23–30. [\[CrossRef\]](#)
132. Hayashi, Y. Ordering of Ni₃Mn and diffusivity of hydrogen in the alloy. *Phys. Status solidi (a)* **1988**, *107*, 619–624. [\[CrossRef\]](#)
133. Vajo, J.J.; Salguero, T.T.; Gross, A.F.; Skeith, S.L.; Olson, G.L. Thermodynamic destabilization and reaction kinetics in light metal hydride systems. *J. Alloy. Compd.* **2007**, *446*, 409–414. [\[CrossRef\]](#)
134. Rönnebro, E.; Kyoi, D.; Kitano, A.; Kitano, Y.; Sakai, T. Hydrogen sites analysed by X-ray synchrotron diffraction in Mg₇TiH₁₃–16 made at gigapascal high-pressures. *J. Alloy. Compd.* **2005**, *404*–*406*, 68–72. [\[CrossRef\]](#)
135. Moser, D.; Bull, D.J.; Sato, T.; Noréus, D.; Kyoi, D.; Sakai, T.; Kitamura, N.; Yusa, H.; Taniguchi, T.; Kalisvaart, W.P.; et al. Structure and stability of high pressure synthesized Mg–TM hydrides (TM = Ti, Zr, Hf, V, Nb and Ta) as possible new hydrogen rich hydrides for hydrogen storage. *J. Mater. Chem.* **2009**, *19*, 8150–8161. [\[CrossRef\]](#)
136. Kyoi, D.; Sato, T.; Rönnebro, E.; Tsuji, Y.; Kitamura, N.; Ueda, A.; Ito, M.; Katsuyama, S.; Hara, S.; Noréus, D.; et al. A novel magnesium–vanadium hydride synthesized by a gigapascal-high-pressure technique. *J. Alloy. Compd.* **2004**, *375*, 253–258. [\[CrossRef\]](#)
137. Kyoi, D.; Rönnebro, E.; Kitamura, N.; Ueda, A.; Ito, M.; Katsuyama, S.; Sakai, T. The first magnesium–chromium hydride synthesized by the gigapascal high-pressure technique. *J. Alloy. Compd.* **2003**, *361*, 252–256. [\[CrossRef\]](#)
138. Goto, Y.; Kakuta, H.; Kamegawa, A.; Takamura, H.; Okada, M. Effect of synthesis pressure on hydride phases in Mg–M. systems (M = Mn, Y). *Sci. Technol. Adv. Mater.* **2003**, *4*, 333–338. [\[CrossRef\]](#)
139. Correspondence. *J. Alloy. Compd.* **1998**, *279*, L8–L10. [\[CrossRef\]](#)
140. Goto, Y.; Hayashi, T.; Kataoka, R.; Kakuta, H.; Kamegawa, A.; Takamura, H.; Okada, M. High-Pressure Synthesis of Novel Hydrides in Mg–TM Systems (TM = Zr, Nb and Mo). *Mater. Trans.* **2005**, *46*, 1798–1801. [\[CrossRef\]](#)
141. Okada, M.; Goto, Y.; Kataoka, R.; Yambe, Y.; Kamegawa, A.; Takamura, H. Novel hydrides in Mg–TM systems synthesized by high pressure (TM=Zr, Nb, Hf and Ta). *J. Alloy. Compd.* **2007**, *446*–*447*, 6–10. [\[CrossRef\]](#)
142. Takasaki, T.; Kyoi, D.; Kitamura, N.; Tanase, S.; Sakai, T. Reversible Hydrogen Storage Property and Structural Analysis for Face-Centered Cubic Hydride Mg_{0.82}Zr_{0.18}H₂ Prepared by Gigapascal Hydrogen Pressure Method. *J. Phys. Chem. B* **2007**, *111*, 14102–14106. [\[CrossRef\]](#) [\[PubMed\]](#)
143. Kyoi, D.; Sakai, T.; Kitamura, N.; Ueda, A.; Tanase, S. Synthesis of FCC Mg–Zr and Mg–Hf hydrides using GPa hydrogen pressure method and their hydrogen-desorption properties. *J. Alloy. Compd.* **2008**, *463*, 311–316. [\[CrossRef\]](#)
144. Kyoi, D.; Kitamura, N.; Tanaka, H.; Ueda, A.; Tanase, S.; Sakai, T. Hydrogen desorption properties of FCC super-lattice hydride Mg₇NbH_x prepared by ultra-high pressure techniques. *J. Alloy. Compd.* **2007**, *428*, 268–273. [\[CrossRef\]](#)
145. Sato, T.; Kyoi, D.; Rönnebro, E.; Kitamura, N.; Sakai, T.; Noréus, D. Structural investigations of two new ternary magnesium–niobium hydrides, Mg_{6.5}NbH_{~14} and MgNb₂H_{~4}. *J. Alloy. Compd.* **2006**, *417*, 230–234. [\[CrossRef\]](#)

146. Chen, Y.; Dai, J.; Wang, L.; Song, Y. Stabilization of Ca₇Ge-type magnesium compounds by alloying of non-metal elements: A new family material for reversible hydrogen storage applications. *Int. J. Hydrog. Energy* **2019**, *44*, 23216–23224. [CrossRef]
147. Shelyapina, M.; Fruchart, D.; Wolfers, P. Electronic structure and stability of new FCC magnesium hydrides Mg₇MH₁₆ and Mg₆MH₁₆ (M = Ti, V, Nb): An ab initio study. *Int. J. Hydrog. Energy* **2010**, *35*, 2025–2032. [CrossRef]
148. Xiao, X.-B.; Zhang, W.-B.; Yu, W.-Y.; Wang, N.; Tang, B.-Y. Energetics and electronic properties of Mg₇TMH₁₆ (TM=Sc, Ti, V, Y, Zr, Nb): An ab initio study. *Phys. B Condens. Matter* **2009**, *404*, 2234–2240. [CrossRef]
149. Erkisi, A.; Gökoglu, G. First principles investigation of Mg₇XH₁₆ (X = Ti, Zn, Pd, and Cd) ternary hydrides for hydrogen storage applications. *Mater. Res. Express* **2018**, *5*, 065517. [CrossRef]
150. Nayeb-Hashemi, A.A.; Clark, J.B. The Co-Mg (Cobalt-Magnesium) system. *Bull. Alloy. Phase Diagr.* **1987**, *8*, 352–355. [CrossRef]
151. Verón, M.; Condó, A.; Gennari, F. Effective synthesis of Mg₂CoH₅ by reactive mechanical milling and its hydrogen sorption behavior after cycling. *Int. J. Hydrog. Energy* **2013**, *38*, 973–981. [CrossRef]
152. Ivanov, E.Y.; Konstantchuk, I.G.; Stepanov, A.A.; Jie, Y.; Pezat, M.; Darriet, B. The ternary system magnesium-cobalt-hydrogen. *Inorg. Chem.* **1989**, *28*, 613–615. [CrossRef]
153. Okamoto, H. Mg-Sc (Magnesium-Scandium). *J. Phase Equilibria Diffus.* **2009**, *30*, 660–661. [CrossRef]
154. Murray, J.L. The Mg-Ti (Magnesium-Titanium) system. *Bull. Alloy. Phase Diagr.* **1986**, *7*, 245–248. [CrossRef]
155. Predel, B. Mg-V (Magnesium-Vanadium). In *Li-Mg-Nd-Zr*; Madelung, O., Ed.; Springer: Berlin/Heidelberg, Germany, 1997; Volume 5H.
156. Bélisle, E. FTlite-FACT Light Alloy Databases. 2021. Available online: https://www.crct.polymtl.ca/fact/phase_diagram.php?file=Cr-Mg.jpg&dir=FTlite.
157. Nayeb-Hashemi, A.A.; Clark, J.B. The Mg-Mn (Magnesium-Manganese) system. *Bull. Alloy. Phase Diagr.* **1985**, *6*, 160–164. [CrossRef]
158. Lu, Y.; Kim, H.; Sakaki, K.; Hayashi, S.; Jimura, K.; Asano, K. Destabilizing the Dehydrogenation Thermodynamics of Magnesium Hydride by Utilizing the Immiscibility of Mn with Mg. *Inorg. Chem.* **2019**, *58*, 14600–14607. [CrossRef]
159. Nayeb-Hashemi, A.A.; Clark, J.B.; Swartzendruber, L.J. The Fe-Mg (Iron-Magnesium) system. *Bull. Alloy. Phase Diagr.* **1985**, *6*, 235–238. [CrossRef]
160. Nayeb-Hashemi, A.A.; Clark, J.B. The Mg-Ni (Magnesium-Nickel) system. *Bull. Alloy. Phase Diagr.* **1985**, *6*, 238–244. [CrossRef]
161. Dai, J.; Jiang, B.; Zhang, J.; Yang, Q.; Jiang, Z.; Dong, H.; Pan, F. Diffusion Kinetics in Mg-Cu Binary System. *J. Phase Equilibria Diffus.* **2015**, *36*, 613–619. [CrossRef]
162. Okamoto, H. Comment on Mg-Zn (magnesium-zinc). *J. Phase Equilibria Diffus.* **1994**, *15*, 129–130. [CrossRef]
163. Okamoto, H. Mg-Y (Magnesium-Yttrium). *J. Phase Equilibria Diffus.* **2010**, *31*, 199. [CrossRef]
164. Okamoto, H. Mg-Zr (Magnesium-Zirconium). *J. Phase Equilibria Diffus.* **2007**, *28*, 305–306. [CrossRef]
165. Edalati, K.; Emami, H.; Ikeda, Y.; Iwaoka, H.; Tanaka, I.; Akiba, E.; Horita, Z. New nanostructured phases with reversible hydrogen storage capability in immiscible magnesium-zirconium system produced by high-pressure torsion. *Acta Mater.* **2016**, *108*, 293–303. [CrossRef]
166. Predel, B. Mg-Nb (Magnesium-Niobium). In *Li-Mg-Nd-Zr*; Madelung, O., Ed.; Springer: Berlin/Heidelberg, Germany, 1997; Volume 5H.
167. Huang, K.; Heinrich, H.; Keiser, D.; Sohn, Y.H. Fuel-Matrix Chemical Interaction between U-7wt.%Mo Alloy and Mg. *Defect Diffus. Forum* **2013**, *333*, 199–206. [CrossRef]
168. Bélisle, E. SGNobl Noble Metal Alloy Database. 2021. Available online: https://www.crct.polymtl.ca/fact/phase_diagram.php?file=Mg-Ru.jpg&dir=SGNobl.
169. Bronger, W.; Jansen, K.; Auffermann, G. Mg₃RuH₆, a complex hydride containing two types of hydrogen atoms differing in their bonding. *J. Alloy. Compd.* **1993**, *199*, 47–51. [CrossRef]
170. Nyeb-Hashemi, A.A.; Clark, J.B. The Mg-Rh (Magnesium-Rhodium) system. *J. Phase Equilibria Diffus.* **1987**, *8*, 117–118. [CrossRef]
171. Bonhomme, F.; Selvam, P.; Yoshida, M.; Yvon, K.; Fischer, P. Hydrogen-stabilized Mg₂RhH_{1.1} with filled Ti₂Ni-type structure. *J. Alloy. Compd.* **1992**, *178*, 167–172. [CrossRef]
172. Becker, J.N.; Bauer, J.; Giehr, A.; Chu, P.I.; Kunkel, N.; Springborg, M.; Kohlmann, H. Electronic Structure of Ternary Rhodium Hydrides with Lithium and Magnesium. *Inorg. Chem.* **2014**, *53*, 1135–1143. [CrossRef]
173. Okamoto, H. Mg-Pd (Magnesium-Palladium). *J. Phase Equilibria Diffus.* **2010**, *31*, 407–408. [CrossRef]
174. Nayeb-Hashemi, A.A.; Clark, J.B. The Ag-Mg (Silver-Magnesium) system. *Bull. Alloy. Phase Diagr.* **1984**, *5*, 348–358. [CrossRef]
175. Si, T.; Zhang, J.; Liu, D.; Zhang, Q. A new reversible Mg₃Ag-H₂ system for hydrogen storage. *J. Alloy. Compd.* **2013**, *581*, 246–249. [CrossRef]
176. Si, T.; Cao, Y.; Zhang, Q.; Sun, D.; Ouyang, L.; Zhu, M. Enhanced hydrogen storage properties of a Mg-Ag alloy with solid dissolution of indium: A comparative study. *J. Mater. Chem. A* **2015**, *3*, 8581–8589. [CrossRef]
177. Shelyapina, M.G.; Siretskiy, M.Y. Influence of 3d metal atoms on the geometry, electronic structure, and stability of a Mg₁₃H₂₆ cluster. *Phys. Solid State* **2010**, *52*, 1992–1998. [CrossRef]
178. Dai, J.; Song, Y.; Yang, R. Intrinsic mechanisms on enhancement of hydrogen desorption from MgH₂ by (001) surface doping. *Int. J. Hydrog. Energy* **2011**, *36*, 12939–12949. [CrossRef]
179. Novaković, N.; Novaković, J.G.; Matović, L.; Manasijević, M.; Radisavljević, I.; Mamula, B.P.; Ivanović, N. Ab initio calculations of MgH₂, MgH₂:Ti and MgH₂:Co compounds. *Int. J. Hydrog. Energy* **2010**, *35*, 598–608. [CrossRef]

180. Smithson, H.; Marianetti, C.A.; Morgan, D.; Van der Ven, A.; Predith, A.; Ceder, G. First-principles study of the stability and electronic structure of metal hydrides. *Phys. Rev. B* **2002**, *66*, 144107. [\[CrossRef\]](#)
181. Myers, W.R.; Wang, L.-W.; Richardson, T.J.; Rubin, M.D. Calculation of thermodynamic, electronic, and optical properties of monoclinic Mg_2NiH_4 . *J. Appl. Phys.* **2002**, *91*, 4879–4885. [\[CrossRef\]](#)
182. Chen, D.; Wang, Y.; Chen, L.; Liu, S.; Ma, C.; Wang, L. Alloying effects of transition metals on chemical bonding in magnesium hydride MgH_2 . *Acta Mater.* **2004**, *52*, 521–528. [\[CrossRef\]](#)
183. Zhang, J.; Qu, H.; Yan, S.; Wu, G.; Yu, X.; Peng, P. Enhanced hydrogen diffusion in magnesium based hydride induced by strain and doping from first principle study. *J. Alloy. Compd.* **2017**, *694*, 687–693. [\[CrossRef\]](#)
184. Zhang, J.; He, L.; Yao, Y.; Zhou, X.; Yu, L.; Lu, X.; Zhou, D. Catalytic effect and mechanism of NiCu solid solutions on hydrogen storage properties of MgH_2 . *Renew. Energy* **2020**, *154*, 1229–1239. [\[CrossRef\]](#)
185. Tao, S.X.; Notten, P.H.; van Santen, R.A.; Jansen, A.P. DFT studies of hydrogen storage properties of $\text{Mg}_{0.75}\text{Ti}_{0.25}$. *J. Alloy. Compd.* **2011**, *509*, 210–216. [\[CrossRef\]](#)
186. Zhang, L.; Sun, Z.; Yao, Z.; Yang, L.; Yan, N.; Lu, X.; Xiao, B.; Zhu, X.-Q.; Chen, L. Excellent catalysis of Mn_3O_4 nanoparticles on the hydrogen storage properties of MgH_2 : An experimental and theoretical study. *Nanoscale Adv.* **2020**, *2*, 1666–1675. [\[CrossRef\]](#)
187. Chen, H.; Ma, N.; Li, J.; Wang, Y.; She, C.; Zhang, Y.; Li, X.; Liu, J.; Feng, X.; Zhou, S. Effect of atomic iron on hydriding reaction of magnesium: Atomic-substitution and atomic-adsorption cases from a density functional theory study. *Appl. Surf. Sci.* **2020**, *504*, 144489. [\[CrossRef\]](#)
188. Zhang, L.; Ji, L.; Yao, Z.; Yan, N.; Sun, Z.; Yang, X.; Zhu, X.; Hu, S.; Chen, L. Facile synthesized Fe nanosheets as superior active catalyst for hydrogen storage in MgH_2 . *Int. J. Hydrog. Energy* **2019**, *44*, 21955–21964. [\[CrossRef\]](#)
189. Zhang, L.; Cai, Z.; Zhu, X.; Yao, Z.; Sun, Z.; Ji, L.; Yan, N.; Xiao, B.; Chen, L. Two-dimensional ZrCo nanosheets as highly effective catalyst for hydrogen storage in MgH_2 . *J. Alloy. Compd.* **2019**, *805*, 295–302. [\[CrossRef\]](#)
190. Wang, K.; Zhang, X.; Ren, Z.; Zhang, X.; Hu, J.; Gao, M.; Pan, H.; Liu, Y. Nitrogen-stimulated superior catalytic activity of niobium oxide for fast full hydrogenation of magnesium at ambient temperature. *Energy Storage Mater.* **2019**, *23*, 79–87. [\[CrossRef\]](#)
191. Du, J.; Lan, Z.; Zhang, H.; Lü, S.; Liu, H.; Guo, J. Catalytic enhanced hydrogen storage properties of Mg-based alloy by the addition of reduced graphene oxide supported V_2O_3 nanocomposite. *J. Alloy. Compd.* **2019**, *802*, 660–667. [\[CrossRef\]](#)
192. Zhang, X.; Leng, Z.; Gao, M.; Hu, J.; Du, F.; Yao, J.; Pan, H.; Liu, Y. Enhanced hydrogen storage properties of MgH_2 catalyzed with carbon-supported nanocrystalline TiO_2 . *J. Power Sources* **2018**, *398*, 183–192. [\[CrossRef\]](#)
193. Shinde, S.S.; Kim, D.-H.; Yu, J.-Y.; Lee, J.-H. Self-assembled air-stable magnesium hydride embedded in 3-D activated carbon for reversible hydrogen storage. *Nanoscale* **2017**, *9*, 7094–7103. [\[CrossRef\]](#)
194. Kumar, S.; Kojima, Y.; Dey, G.K. Tailoring the hydrogen absorption desorption's dynamics of Mg MgH_2 system by titanium suboxide doping. *Int. J. Hydrog. Energy* **2017**, *42*, 21841–21848. [\[CrossRef\]](#)
195. Song, Y.; Guo, Z.; Yang, R. Influence of titanium on the hydrogen storage characteristics of magnesium hydride: A first principles investigation. *Mater. Sci. Eng. A* **2004**, *365*, 73–79. [\[CrossRef\]](#)
196. Varunaa, R.; Kiruthika, S.; Ravindran, P. Ti^{4+} substituted magnesium hydride as promising material for hydrogen storage and photovoltaic applications. *AIP Conf. Proc.* **2019**, *2115*, 030545. [\[CrossRef\]](#)
197. Varunaa, R.; Fjellvåg, H.; Ravindran, P. Zinc substituted MgH_2 —A potential material for hydrogen storage applications. *Int. J. Hydrog. Energy* **2019**, *44*, 13632–13646. [\[CrossRef\]](#)
198. Shelyapina, M.G.; Fruchart, D. Role of Transition Elements in Stability of Magnesium Hydride: A Review of Theoretical Studies. *Solid State Phenom.* **2011**, *170*, 227–231. [\[CrossRef\]](#)
199. Novaković, J.G.; Novaković, N.; Kurko, S.; Govedarović, S.M.; Pantić, T.; Mamula, B.P.; Batalović, K.; Radaković, J.; Rmuš, J.; Shelyapina, M.; et al. Influence of Defects on the Stability and Hydrogen-Sorption Behavior of Mg-Based Hydrides. *ChemPhysChem* **2019**, *20*, 1216–1247. [\[CrossRef\]](#) [\[PubMed\]](#)
200. Liu, T.; Ma, X.; Chen, C.; Xu, L.; Li, X. Catalytic Effect of Nb Nanoparticles for Improving the Hydrogen Storage Properties of Mg-Based Nanocomposite. *J. Phys. Chem. C* **2015**, *119*, 14029–14037. [\[CrossRef\]](#)
201. Wu, X.; Zhang, R.; Yang, J. A first-principles study of the thermodynamic and electronic properties of Mg and MgH_2 nanowires. *Phys. Chem. Chem. Phys.* **2016**, *18*, 19412–19419. [\[CrossRef\]](#) [\[PubMed\]](#)
202. Allred, A. Electronegativity values from thermochemical data. *J. Inorg. Nucl. Chem.* **1961**, *17*, 215–221. [\[CrossRef\]](#)
203. Huheey, J.E.; Keiter, E.A.; Keiter, R.L. *Inorganic Chemistry: Principles of Structure and Reactivity*, 4th ed.; HarperCollins: New York, NY, USA, 1993; p. 30.
204. Wang, Z.; Guo, X.; Wu, M.; Sun, Q.; Jia, Y. First-principles study of hydrogen dissociation and diffusion on transition metal-doped $\text{Mg}(0001)$ surfaces. *Appl. Surf. Sci.* **2014**, *305*, 40–45. [\[CrossRef\]](#)
205. Zhang, J.; Zhu, Y.; Yao, L.; Xu, C.; Liu, Y.; Li, L. State of the art multi-strategy improvement of Mg-based hydrides for hydrogen storage. *J. Alloy. Compd.* **2018**, *782*, 796–823. [\[CrossRef\]](#)
206. Liu, Y.; Zhu, J.; Liu, Z.; Zhu, Y.; Zhang, J.; Li, L. Magnesium Nanoparticles with Pd Decoration for Hydrogen Storage. *Front. Chem.* **2020**, *7*, 949. [\[CrossRef\]](#)
207. Lu, C.; Ma, Y.; Li, F.; Zhu, H.; Zeng, X.; Ding, W.; Deng, T.; Wu, J.; Zou, J. Visualization of fast “hydrogen pump” in core-shell nanostructured Mg@Pt through hydrogen-stabilized Mg_3Pt . *J. Mater. Chem. A* **2019**, *7*, 14629–14637. [\[CrossRef\]](#)
208. Ji, L.; Zhang, L.; Yang, X.; Zhu, X.; Chen, L. The remarkably improved hydrogen storage performance of MgH_2 by the synergetic effect of an FeNi/rGO nanocomposite. *Dalton Trans.* **2020**, *49*, 4146–4154. [\[CrossRef\]](#) [\[PubMed\]](#)

209. Xu, X.; Song, C. Improving hydrogen storage/release properties of magnesium with nano-sized metal catalysts as measured by tapered element oscillating microbalance. *Appl. Catal. A Gen.* **2006**, *300*, 130–138. [\[CrossRef\]](#)
210. Du, A.J.; Smith, S.C.; Yao, X.D.; Sun, C.H.; Li, L.; Lu, G.Q. The role of V_2O_5 on the dehydrogenation and hydrogenation in magnesium hydride: An ab initio study. *Appl. Phys. Lett.* **2008**, *92*, 163106. [\[CrossRef\]](#)
211. Pozzo, M.; Alfè, D. Hydrogen dissociation and diffusion on transition metal (=Ti, Zr, V, Fe, Ru, Co, Rh, Ni, Pd, Cu, Ag)-doped Mg(0001) surfaces. *Int. J. Hydrog. Energy* **2009**, *34*, 1922–1930. [\[CrossRef\]](#)
212. Vegge, T.; Hedegaard-Jensen, L.S.; Bonde, J.; Munter, T.R.; Nørskov, J.K. Trends in hydride formation energies for magnesium-3d transition metal alloys. *J. Alloy. Compd.* **2005**, *386*, 1–7. [\[CrossRef\]](#)
213. Ni, M.; Huang, L.; Guo, L.; Zeng, Z. Hydrogen storage in Li-doped charged single-walled carbon nanotubes. *Int. J. Hydrog. Energy* **2010**, *35*, 3546–3549. [\[CrossRef\]](#)
214. Huang, X.; Xiao, X.; Wang, X.; Wang, C.; Fan, X.; Tang, Z.; Wang, C.; Wang, Q.; Chen, L. Synergistic Catalytic Activity of Porous Rod-like TiO_3 (TM = Ni and Co) for Reversible Hydrogen Storage of Magnesium Hydride. *J. Phys. Chem. C* **2018**, *122*, 27973–27982. [\[CrossRef\]](#)
215. Yao, P.; Jiang, Y.; Liu, Y.; Wu, C.; Chou, K.-C.; Lyu, T.; Li, Q. Catalytic effect of Ni@rGO on the hydrogen storage properties of MgH_2 . *J. Magnes. Alloy* **2020**, *8*, 461–471. [\[CrossRef\]](#)
216. Wang, P.; Wang, Z.; Tian, Z.; Xia, C.; Yang, T.; Liang, C.; Li, Q. Enhanced hydrogen absorption and desorption properties of MgH_2 with NiS₂: The catalytic effect of in-situ formed MgS and Mg_2NiH_4 phases. *Renew. Energy* **2020**, *160*, 409–417. [\[CrossRef\]](#)
217. Liu, P.; Lian, J.; Chen, H.; Liu, X.; Chen, Y.; Zhang, T.; Yu, H.; Lu, G.; Zhou, S. In-situ synthesis of Mg_2Ni -CeO₁₁ catalyst for improvement of hydrogen storage in magnesium. *Chem. Eng. J.* **2019**, *385*, 123448. [\[CrossRef\]](#)
218. Dai, J.H.; Song, Y.; Yang, R. First Principles Study on Hydrogen Desorption from a Metal (=Al, Ti, Mn, Ni) Doped MgH_2 (110) Surface. *J. Phys. Chem. C* **2010**, *114*, 11328–11334. [\[CrossRef\]](#)
219. Ding, Z.; Fu, Y.; Wang, Y.; Bi, J.; Zhang, L.; Peng, D.; Li, Y.; Han, S. $MgCNi_3$ prepared by powder metallurgy for improved hydrogen storage properties of MgH_2 . *Int. J. Hydrog. Energy* **2019**, *44*, 8347–8356. [\[CrossRef\]](#)
220. Chen, M.; Xiao, X.; Zhang, M.; Liu, M.; Huang, X.; Zheng, J.; Zhang, Y.; Jiang, L.; Chen, L. Excellent synergistic catalytic mechanism of in-situ formed nanosized Mg_2Ni and multiple valence titanium for improved hydrogen desorption properties of magnesium hydride. *Int. J. Hydrog. Energy* **2019**, *44*, 1750–1759. [\[CrossRef\]](#)
221. Wu, C.; Wang, Y.; Liu, Y.; Ding, W.; Sun, C. Enhancement of hydrogen storage properties by in situ formed LaH_3 and Mg_2NiH_4 during milling MgH_2 with porous $LaNiO_3$. *Catal. Today* **2018**, *318*, 113–118. [\[CrossRef\]](#)
222. Xie, X.; Chen, M.; Liu, P.; Shang, J.; Liu, T. High hydrogen desorption properties of Mg-based nanocomposite at moderate temperatures: The effects of multiple catalysts in situ formed by adding nickel sulfides/graphene. *J. Power Sources* **2017**, *371*, 112–118. [\[CrossRef\]](#)
223. Huang, X.; Xiao, X.; Zhang, W.; Fan, X.; Zhang, L.; Cheng, C.; Li, S.; Ge, H.; Wang, Q.; Chen, L. Transition metal (Co, Ni) nanoparticles wrapped with carbon and their superior catalytic activities for the reversible hydrogen storage of magnesium hydride. *Phys. Chem. Chem. Phys.* **2017**, *19*, 4019–4029. [\[CrossRef\]](#) [\[PubMed\]](#)
224. Lu, C.; Zou, J.; Shi, X.; Zeng, X.; Ding, W. Synthesis and hydrogen storage properties of core-shell structured binary Mg@Ti and ternary Mg@Ti@Ni composites. *Int. J. Hydrog. Energy* **2017**, *42*, 2239–2247. [\[CrossRef\]](#)
225. Xie, X.; Ma, X.; Liu, P.; Shang, J.; Li, X.; Liu, T. Formation of Multiple-Phase Catalysts for the Hydrogen Storage of Mg Nanoparticles by Adding Flowerlike NiS. *ACS Appl. Mater. Interfaces* **2017**, *9*, 5937–5946. [\[CrossRef\]](#) [\[PubMed\]](#)
226. Chen, M.; Pu, Y.; Li, Z.; Huang, G.; Liu, X.; Lu, Y.; Tang, W.; Xu, L.; Liu, S.; Yu, R.; et al. Synergy between metallic components of MoNi alloy for catalyzing highly efficient hydrogen storage of MgH_2 . *Nano Res.* **2020**, *13*, 2063–2071. [\[CrossRef\]](#)
227. Zhang, J.; Zhu, Y.; Zang, X.; Huan, Q.; Su, W.; Zhu, D.; Li, L. Nickel-decorated graphene nanoplates for enhanced H_2 sorption properties of magnesium hydride at moderate temperatures. *J. Mater. Chem. A* **2016**, *4*, 2560–2570. [\[CrossRef\]](#)
228. Bouhadda, Y.; Bououdina, M.; Fenineche, N.; Boudouma, Y. Electronic and elastic properties of Mg_7TiH_{16} hydrogen storage material. *Comput. Mater. Sci.* **2013**, *78*, 110–115. [\[CrossRef\]](#)
229. Lin, H.-J.; Tang, J.-J.; Yu, Q.; Wang, H.; Ouyang, L.-Z.; Zhao, Y.-J.; Liu, J.-W.; Wang, W.-H.; Zhu, M. Symbiotic $CeH_{2.73}/CeO_2$ catalyst: A novel hydrogen pump. *Nano Energy* **2014**, *9*, 80–87. [\[CrossRef\]](#)
230. Daryani, M.; Simchi, A.; Sadati, M.; Hosseini, H.M.; Targholizadeh, H.; Khakbiz, M. Effects of Ti-based catalysts on hydrogen desorption kinetics of nanostructured magnesium hydride. *Int. J. Hydrog. Energy* **2014**, *39*, 21007–21014. [\[CrossRef\]](#)
231. Khrussanova, M.; Grigorova, E.; Mitov, I.; Radev, D.; Peshev, P. Hydrogen sorption properties of an Mg–Ti–V–Fe nanocomposite obtained by mechanical alloying. *J. Alloy. Compd.* **2001**, *327*, 230–234. [\[CrossRef\]](#)
232. Shen, Z.; Wang, Z.; Zhang, M.; Gao, M.; Hu, J.; Du, F.; Liu, Y.; Pan, H. A novel solid-solution MXene ($Ti_{0.5}V_{0.5}$)₃C₂ with high catalytic activity for hydrogen storage in MgH_2 . *Materialia* **2018**, *1*, 114–120. [\[CrossRef\]](#)
233. Song, M.Y.; Kwak, Y.J.; Lee, S.H.; Song, J.; Mumm, D.R. Enhancement of hydrogen-storage performance of MgH_2 by Mg_2Ni formation and hydride-forming Ti addition. *Int. J. Hydrog. Energy* **2012**, *37*, 18133–18139. [\[CrossRef\]](#)
234. Dehouche, Z.; Goyette, J.; Bose, T.; Schulz, R. Moisture effect on hydrogen storage properties of nanostructured MgH_2 –V–Ti composite. *Int. J. Hydrog. Energy* **2003**, *28*, 983–988. [\[CrossRef\]](#)
235. Liang, G.; Huot, J.; Boily, S.; Van Neste, A.; Schulz, R. Hydrogen storage properties of the mechanically milled MgH_2 –V nanocomposite. *J. Alloy. Compd.* **1999**, *291*, 295–299. [\[CrossRef\]](#)

236. Yavari, A.; de Castro, J.; Vaughan, G.; Heunen, G. Structural evolution and metastable phase detection in MgH_2 -5%NbH nanocomposite during in-situ H-desorption in a synchrotron beam. *J. Alloy. Compd.* **2003**, *353*, 246–251. [\[CrossRef\]](#)
237. Floriano, R.; Deledda, S.; Hauback, B.; Leiva, D.; Botta, W. Iron and niobium based additives in magnesium hydride: Microstructure and hydrogen storage properties. *Int. J. Hydrog. Energy* **2016**, *42*, 6810–6819. [\[CrossRef\]](#)
238. Patelli, N.; Migliori, A.; Morandi, V.; Pasquini, L. Interfaces within biphasic nanoparticles give a boost to magnesium-based hydrogen storage. *Nano Energy* **2020**, *72*, 104654. [\[CrossRef\]](#)
239. Ma, X.; Xie, X.; Liu, P.; Xu, L.; Liu, T. Synergic catalytic effect of Ti hydride and Nb nanoparticles for improving hydrogenation and dehydrogenation kinetics of Mg-based nanocomposite. *Prog. Nat. Sci.* **2017**, *27*, 99–104. [\[CrossRef\]](#)
240. Cuevas, F.; Korablov, D.; Latroche, M. Synthesis, structural and hydrogenation properties of Mg-rich MgH_2 -TiH₂ nanocomposites prepared by reactive ball milling under hydrogen gas. *Phys. Chem. Chem. Phys.* **2012**, *14*, 1200–1211. [\[CrossRef\]](#)
241. Weaver, J.H.; Peterman, D.J.; Peterson, D.T.; Franciosi, A. Electronic structure of metal hydrides. IV. TiH_x, ZrH_x, HfH_x, and the fcc-fct lattice distortion. *Phys. Rev. B* **1981**, *23*, 1692–1698. [\[CrossRef\]](#)
242. Weaver, J.; Peterson, D. Electronic structure studies of metal hydrides. *J. Less Common Met.* **1980**, *74*, 207–216. [\[CrossRef\]](#)
243. Pasquini, L.; Sacchi, M.; Brighi, M.; Boelsma, C.; Bals, S.; Perkisas, T.; Dam, B. Hydride destabilization in core-shell nanoparticles. *Int. J. Hydrog. Energy* **2014**, *39*, 2115–2123. [\[CrossRef\]](#)
244. Liu, W.; Setijadi, E.J.; Aguey-Zinsou, K.-F. Tuning the Thermodynamic Properties of MgH_2 at the Nanoscale via a Catalyst or Destabilizing Element Coating Strategy. *J. Phys. Chem. C* **2014**, *118*, 27781–27792. [\[CrossRef\]](#)
245. Baldi, A.; Gonzalez-Silveira, M.; Palmisano, V.; Dam, B.; Griessen, R. Destabilization of the Mg-H System through Elastic Constraints. *Phys. Rev. Lett.* **2009**, *102*, 226102. [\[CrossRef\]](#) [\[PubMed\]](#)
246. Wagner, S.; Pundt, A. Quasi-thermodynamic model on hydride formation in palladium-hydrogen thin films: Impact of elastic and microstructural constraints. *Int. J. Hydrog. Energy* **2016**, *41*, 2727–2738. [\[CrossRef\]](#)
247. Pasquini, L.; Boscherini, F.; Callini, E.; Maurizio, C.; Pasquali, L.; Montecchi, M.; Bonetti, E. Local structure at interfaces between hydride-forming metals: A case study of Mg-Pd nanoparticles by x-ray spectroscopy. *Phys. Rev. B* **2011**, *83*, 184111. [\[CrossRef\]](#)
248. Chung, C.-J.; Lee, S.-C.; Groves, J.R.; Brower, E.N.; Sinclair, R.; Clemens, B.M. Interfacial Alloy Hydride Destabilization in Mg/Pd Thin Films. *Phys. Rev. Lett.* **2012**, *108*, 106102. [\[CrossRef\]](#) [\[PubMed\]](#)
249. Hao, S.; Sholl, D.S. Effect of TiH₂-Induced Strain on Thermodynamics of Hydrogen Release from MgH_2 . *J. Phys. Chem. C* **2012**, *116*, 2045–2050. [\[CrossRef\]](#)
250. Alefeld, G. Phase transitions of hydrogen in metals due to elastic interaction. *Ber. Der Bunsenges. Für Phys. Chem.* **1972**, *76*, 746–755. [\[CrossRef\]](#)
251. Roy, A.; Janotti, A.; Van de Walle, C.G. Effect of transition-metal additives on hydrogen desorption kinetics of MgH_2 . *Appl. Phys. Lett.* **2013**, *102*, 033902. [\[CrossRef\]](#)
252. German, E.; Gebauer, R. Improvement of Hydrogen Vacancy Diffusion Kinetics in MgH_2 by Niobium- and Zirconium-Doping for Hydrogen Storage Applications. *J. Phys. Chem. C* **2016**, *120*, 4806–4812. [\[CrossRef\]](#)
253. Giusepponi, S.; Celino, M. DFT model of hydrogen desorption from MgH_2 : The role of iron catalyst. *Int. J. Hydrog. Energy* **2013**, *38*, 15254–15263. [\[CrossRef\]](#)
254. Klyukin, K.; Shelyapina, M.G.; Fruchart, D. Hydrogen induced phase transition in magnesium: An Ab initio study. *J. Alloy. Compd.* **2013**, *580*, S10–S12. [\[CrossRef\]](#)
255. Tao, S.X.; Notten, P.H.L.; van Santen, R.A.; Jansen, A.P.J. Density functional theory studies of the hydrogenation properties of Mg and Ti. *Phys. Rev. B* **2009**, *79*, 144121. [\[CrossRef\]](#)
256. Uchida, H.T.; Kirchheim, R.; Pundt, A. Influence of hydrogen loading conditions on the blocking effect of nanocrystalline Mg films. *Scr. Mater.* **2011**, *64*, 935–937. [\[CrossRef\]](#)
257. Song, M.; Bobet, J.-L.; Darriet, B. Improvement in hydrogen sorption properties of Mg by reactive mechanical grinding with Cr_2O_3 , Al_2O_3 and CeO_2 . *J. Alloy. Compd.* **2002**, *340*, 256–262. [\[CrossRef\]](#)
258. Pukazhselvan, D.; Nasani, N.; Correia, P.; Carbó-Argibay, E.; Otero-Irurueta, G.; Stroppa, D.G.; Fagg, D.P. Evolution of reduced Ti containing phase(s) in $\text{MgH}_2/\text{TiO}_2$ system and its effect on the hydrogen storage behavior of MgH_2 . *J. Power Sources* **2017**, *362*, 174–183. [\[CrossRef\]](#)
259. Sazelee, N.; Idris, N.; Din, M.; Mustafa, N.; Ali, N.; Yahya, M.; Yap, F.H.; Sulaiman, N.; Ismail, M. Synthesis of $\text{BaFe}_{12}\text{O}_{19}$ by solid state method and its effect on hydrogen storage properties of MgH_2 . *Int. J. Hydrog. Energy* **2018**, *43*, 20853–20860. [\[CrossRef\]](#)
260. Ali, N.A.; Idris, N.H.; Din, M.F.; Mustafa, N.S.; Sazelee, N.A.; Yap, F.A.H.; Sulaiman, N.N.; Yahya, M.S.; Ismail, M. Nanolayer-like-shaped MgFe_2O_4 synthesised via a simple hydrothermal method and its catalytic effect on the hydrogen storage properties of MgH_2 . *RSC Adv.* **2018**, *8*, 15667–15674. [\[CrossRef\]](#)
261. Zhang, T.; Isobe, S.; Jain, A.; Wang, Y.; Yamaguchi, S.; Miyaoka, H.; Ichikawa, T.; Kojima, Y.; Hashimoto, N. Enhancement of hydrogen desorption kinetics in magnesium hydride by doping with lithium metatitanate. *J. Alloy. Compd.* **2017**, *711*, 400–405. [\[CrossRef\]](#)
262. Friedrichs, O.; Aguey-Zinsou, F.; Fernández, J.A.; Sánchez-López, J.; Justo, A.; Klassen, T.; Bormann, R.; Fernández, A. MgH_2 with Nb_2O_5 as additive, for hydrogen storage: Chemical, structural and kinetic behavior with heating. *Acta Mater.* **2006**, *54*, 105–110. [\[CrossRef\]](#)
263. Friedrichs, O.; Klassen, T.; Sánchez-López, J.; Bormann, R.; Fernández, A. Hydrogen sorption improvement of nanocrystalline MgH_2 by Nb_2O_5 nanoparticles. *Scr. Mater.* **2006**, *54*, 1293–1297. [\[CrossRef\]](#)

264. Porcu, M.; Petford-Long, A.; Sykes, J. TEM studies of Nb₂O₅ catalyst in ball-milled MgH₂ for hydrogen storage. *J. Alloy. Compd.* **2008**, *453*, 341–346. [\[CrossRef\]](#)
265. Pukazhselvan, D.; Nasani, N.; Sandhya, K.; Singh, B.; Bdikin, I.; Koga, N.; Fagg, D.P. Role of chemical interaction between MgH₂ and TiO₂ additive on the hydrogen storage behavior of MgH₂. *Appl. Surf. Sci.* **2017**, *420*, 740–745. [\[CrossRef\]](#)
266. Pukazhselvan, D.; Bdikin, I.; Perez, J.; Carbó-Argibay, E.; Antunes, I.; Stroppa, D.G.; Fagg, D.P. Formation of Mg–Nb–O rock salt structures in a series of mechanochemically activated MgH₂ + nNb₂O₅ (n = 0.083–1.50) mixtures. *Int. J. Hydrog. Energy* **2016**, *41*, 2677–2688. [\[CrossRef\]](#)
267. Friedrichs, O.; Sánchez-López, J.C.; López-Cartes, C.; Klassen, T.; Bormann, R.; Fernández, A. Nb₂O₅ “Pathway Effect” on Hydrogen Sorption in Mg. *J. Phys. Chem. B* **2006**, *110*, 7845–7850. [\[CrossRef\]](#) [\[PubMed\]](#)
268. Pukazhselvan, D.; Nasani, N.; Yang, T.; Ramasamy, D.; Shaula, A.; Fagg, D.P. Chemically transformed additive phases in Mg₂TiO₄ and MgTiO₃ loaded hydrogen storage system MgH₂. *Appl. Surf. Sci.* **2019**, *472*, 99–104. [\[CrossRef\]](#)
269. Liu, P.; Chen, H.; Yu, H.; Liu, X.; Jiang, R.; Li, X.; Zhou, S. Oxygen vacancy in magnesium/cerium composite from ball milling for hydrogen storage improvement. *Int. J. Hydrog. Energy* **2019**, *44*, 13606–13612. [\[CrossRef\]](#)
270. Cui, J.; Wang, H.; Liu, J.; Ouyang, L.; Zhang, Q.; Sun, D.; Yao, X.; Zhu, M. Remarkable enhancement in dehydrogenation of MgH₂ by a nano-coating of multi-valence Ti-based catalysts. *J. Mater. Chem. A* **2013**, *1*, 5603–5611. [\[CrossRef\]](#)
271. Mao, J.; Zou, J.; Lu, C.; Zeng, X.; Ding, W. Hydrogen storage and hydrolysis properties of core-shell structured Mg-MFx (M=V, Ni, La and Ce) nano-composites prepared by arc plasma method. *J. Power Sources* **2017**, *366*, 131–142. [\[CrossRef\]](#)
272. Zheng, S.; Fang, F.; Zhang, J.; Sun, L.; He, B.; Wei, S.; Chen, G.; Sun, D. Study of the Correlation between the Stability of Mg-Based Hydride and the Ti-Containing Agent. *J. Phys. Chem. C* **2007**, *111*, 14021–14025. [\[CrossRef\]](#)
273. Fernandez, J.R.A.; Aguey-Zinsou, K.-F. Superior MgH₂ Kinetics with MgO Addition: A Tribological Effect. *Catalysts* **2012**, *2*, 330–343. [\[CrossRef\]](#)
274. Chen, M.; Xiao, X.; Zhang, M.; Zheng, J.; Liu, M.; Wang, X.; Jiang, L.; Chen, L. Highly dispersed metal nanoparticles on TiO₂ acted as nano redox reactor and its synergistic catalysis on the hydrogen storage properties of magnesium hydride. *Int. J. Hydrog. Energy* **2019**, *44*, 15100–15109. [\[CrossRef\]](#)
275. Ma, Z.; Zhang, Q.; Zhu, W.; Khan, D.; Hu, C.; Huang, T.; Ding, W.; Zou, J. Nano Fe and Mg₂Ni derived from TMA-TM (TM = Fe, Ni) MOFs as synergetic catalysts for hydrogen storage in MgH₂. *Sustain. Energy Fuels* **2020**, *4*, 2192–2200. [\[CrossRef\]](#)
276. Sun, C.; Jia, Y.; Yang, X.-H.; Yang, H.-G.; Yao, X.; Lu, G.Q.; Selloni, A.; Smith, S.C. Hydrogen Incorporation and Storage in Well-Defined Nanocrystals of Anatase Titanium Dioxide. *J. Phys. Chem. C* **2011**, *115*, 25590–25594. [\[CrossRef\]](#)
277. Ma, Z.; Liu, J.; Zhu, Y.; Zhao, Y.; Lin, H.; Zhang, Y.; Li, H.; Zhang, J.; Liu, Y.; Gao, W.; et al. Crystal-facet-dependent catalysis of anatase TiO₂ on hydrogen storage of MgH₂. *J. Alloy. Compd.* **2020**, *822*, 153553. [\[CrossRef\]](#)
278. Zhang, M.; Xiao, X.; Wang, X.; Chen, M.; Lu, Y.; Liu, M.; Chen, L. Excellent catalysis of TiO₂ nanosheets with high-surface-energy {001} facets on the hydrogen storage properties of MgH₂. *Nanoscale* **2019**, *11*, 7465–7473. [\[CrossRef\]](#)
279. Liu, T.; Chen, C.; Wang, H.; Wu, Y. Enhanced Hydrogen Storage Properties of Mg–Ti–V Nanocomposite at Moderate Temperatures. *J. Phys. Chem. C* **2014**, *118*, 22419–22425. [\[CrossRef\]](#)
280. Blanco-Rey, M.; Juaristi, J.I.; Alducin, M.; López, M.J.; Alonso, J.A. Is Spillover Relevant for Hydrogen Adsorption and Storage in Porous Carbons Doped with Palladium Nanoparticles. *J. Phys. Chem. C* **2016**, *120*, 17357–17364. [\[CrossRef\]](#)
281. Rangel, E.; Sansores, E.; Vallejo, E.; Hernández-Hernández, A.; López-Pérez, P.A. Study of the interplay between N-graphene defects and small Pd clusters for enhanced hydrogen storage via a spill-over mechanism. *Phys. Chem. Chem. Phys.* **2016**, *18*, 33158–33170. [\[CrossRef\]](#)
282. Karim, W.; Spreafico, C.; Kleibert, A.; Gobrecht, J.; VandeVondele, J.; Ekinici, Y.; van Bokhoven, J.A. Catalyst support effects on hydrogen spillover. *Nature* **2017**, *541*, 68–71. [\[CrossRef\]](#)
283. Zhou, C.; Szpunar, J.A.; Cui, X. Synthesis of Ni/Graphene Nanocomposite for Hydrogen Storage. *ACS Appl. Mater. Interfaces* **2016**, *8*, 15232–15241. [\[CrossRef\]](#) [\[PubMed\]](#)
284. Peng, Z.; Li, Z.; Liu, Y.-Q.; Yan, S.; Tong, J.; Wang, D.; Ye, Y.; Li, S. Supported Pd nanoclusters with enhanced hydrogen spillover for NO_x removal via H₂-SCR: The elimination of “volcano-type” behaviour. *Chem. Commun.* **2017**, *53*, 5958–5961. [\[CrossRef\]](#)
285. Zhou, H.; Zhang, J.; Ji, D.; Yuan, A.; Shen, X. Effect of catalyst loading on hydrogen storage capacity of ZIF-8/graphene oxide doped with Pt or Pd via spillover. *Microporous Mesoporous Mater.* **2016**, *229*, 68–75. [\[CrossRef\]](#)
286. Zhou, C.; Szpunar, J.A. Hydrogen Storage Performance in Pd/Graphene Nanocomposites. *ACS Appl. Mater. Interfaces* **2016**, *8*, 25933–25940. [\[CrossRef\]](#) [\[PubMed\]](#)
287. Valencia, F.J.; González, R.I.; Tramontina, D.; Rogan, J.; Valdivia, J.A.; Kiwi, M.; Bringa, E.M. Hydrogen Storage in Palladium Hollow Nanoparticles. *J. Phys. Chem. C* **2016**, *120*, 23836–23841. [\[CrossRef\]](#)
288. Liu, M.; Zhao, S.; Xiao, X.; Chen, M.; Sun, C.; Yao, Z.; Hu, Z.; Chen, L. Novel 1D carbon nanotubes uniformly wrapped nanoscale MgH₂ for efficient hydrogen storage cycling performances with extreme high gravimetric and volumetric capacities. *Nano Energy* **2019**, *61*, 540–549. [\[CrossRef\]](#)
289. Bérubé, V.; Radtke, G.; Dresselhaus, M.; Chen, G. Size effects on the hydrogen storage properties of nanostructured metal hydrides: A review. *Int. J. Energy Res.* **2007**, *31*, 637–663. [\[CrossRef\]](#)
290. Aguey-Zinsou, K.-F.; Ares-Fernández, J.-R. Hydrogen in magnesium: New perspectives toward functional stores. *Energy Environ. Sci.* **2010**, *3*, 526–543. [\[CrossRef\]](#)

291. de Jongh, P.E.; Adelhelm, P. Nanosizing and Nanoconfinement: New Strategies Towards Meeting Hydrogen Storage Goals. *ChemSuschem* **2010**, *3*, 1332–1348. [[CrossRef](#)]
292. Kalidindi, S.B.; Jagirdar, B.R. Highly Monodisperse Colloidal Magnesium Nanoparticles by Room Temperature Digestive Ripening. *Inorg. Chem.* **2009**, *48*, 4524–4529. [[CrossRef](#)] [[PubMed](#)]
293. Schneemann, A.; White, J.L.; Kang, S.; Jeong, S.; Wan, L.F.; Cho, E.S.; Heo, T.W.; Prendergast, D.; Urban, J.J.; Wood, B.C.; et al. Nanostructured Metal Hydrides for Hydrogen Storage. *Chem. Rev.* **2018**, *118*, 10775–10839. [[CrossRef](#)] [[PubMed](#)]
294. Zhang, J.; Yan, S.; Qu, H. Recent progress in magnesium hydride modified through catalysis and nanoconfinement. *Int. J. Hydrog. Energy* **2018**, *43*, 1545–1565. [[CrossRef](#)]
295. Li, J.; Li, B.; Shao, H.; Li, W.; Lin, H. Catalysis and Downsizing in Mg-Based Hydrogen Storage Materials. *Catalysts* **2018**, *8*, 89. [[CrossRef](#)]
296. Cui, J.; Ouyang, L.; Wang, H.; Yao, X.; Zhu, M. On the hydrogen desorption entropy change of modified MgH_2 . *J. Alloy. Compd.* **2018**, *737*, 427–432. [[CrossRef](#)]
297. Konarova, M.; Tanksale, A.; Beltramini, J.N.; Lu, G. Effects of nano-confinement on the hydrogen desorption properties of MgH_2 . *Nano Energy* **2013**, *2*, 98–104. [[CrossRef](#)]
298. Zhao-Karger, Z.; Hu, J.; Roth, A.; Wang, D.; Kübel, C.; Lohstroh, W.; Fichtner, M. Altered thermodynamic and kinetic properties of MgH_2 infiltrated in microporous scaffold. *Chem. Commun.* **2010**, *46*, 8353–8355. [[CrossRef](#)] [[PubMed](#)]
299. Zhou, S.; Zhang, X.; Li, T.; Wang, N.; Chen, H.; Zhang, T.; Yu, H.; Niu, H.; Liu, D. Nano-confined magnesium for hydrogen storage from reactive milling with anthracite carbon as milling aid. *Int. J. Hydrog. Energy* **2014**, *39*, 13628–13633. [[CrossRef](#)]
300. Sun, Y.; Ma, T.; Aguey-Zinsou, K.-F. Magnesium Supported on Nickel Nanobelts for Hydrogen Storage: Coupling Nanosizing and Catalysis. *ACS Appl. Nano Mater.* **2018**, *1*, 1272–1279. [[CrossRef](#)]
301. Xia, G.; Tan, Y.; Chen, X.; Sun, D.; Guo, Z.; Liu, H.; Ouyang, L.; Zhu, M.; Yu, X. Monodisperse Magnesium Hydride Nanoparticles Uniformly Self-Assembled on Graphene. *Adv. Mater.* **2015**, *27*, 5981–5988. [[CrossRef](#)]
302. Wagemans, R.W.P.; van Lenthe, J.H.; de Jongh, P.E.; van Dillen, A.J.; de Jong, K.P. Hydrogen Storage in Magnesium Clusters: Quantum Chemical Study. *J. Am. Chem. Soc.* **2005**, *127*, 16675–16680. [[CrossRef](#)] [[PubMed](#)]
303. Kim, K.C.; Dai, B.; Johnson, J.K.; Sholl, D.S. Assessing nanoparticle size effects on metal hydride thermodynamics using the Wulff construction. *Nanotechnology* **2009**, *20*, 204001. [[CrossRef](#)]
304. Jain, I.; Lal, C.; Jain, A. Hydrogen storage in Mg: A most promising material. *Int. J. Hydrog. Energy* **2010**, *35*, 5133–5144. [[CrossRef](#)]
305. Liu, W.; Aguey-Zinsou, K.-F. Size effects and hydrogen storage properties of Mg nanoparticles synthesised by an electroless reduction method. *J. Mater. Chem. A* **2014**, *2*, 9718–9726. [[CrossRef](#)]
306. Aguey-Zinsou, K.-F.; Fernandez, J.A.; Klassen, T.; Bormann, R. Effect of Nb_2O_5 on MgH_2 properties during mechanical milling. *Int. J. Hydrog. Energy* **2007**, *32*, 2400–2407. [[CrossRef](#)]
307. Zhang, X.; Liu, Y.; Hu, J.; Gao, M.; Pan, H. Empowering hydrogen storage performance of MgH_2 by nanoengineering and nanocatalysis. *Mater. Today Nano* **2020**, *9*, 100064. [[CrossRef](#)]
308. Pang, Y.; Li, Q. A review on kinetic models and corresponding analysis methods for hydrogen storage materials. *Int. J. Hydrog. Energy* **2016**, *41*, 18072–18087. [[CrossRef](#)]

Disclaimer/Publisher's Note: The statements, opinions and data contained in all publications are solely those of the individual author(s) and contributor(s) and not of MDPI and/or the editor(s). MDPI and/or the editor(s) disclaim responsibility for any injury to people or property resulting from any ideas, methods, instructions or products referred to in the content.